

Electronic Thesis and Dissertation Repository

8-3-2021 11:15 AM

Brain Representations of Dexterous Hand Control: Investigating the Functional Organization of Individuated Finger Movements and Somatosensory Integration

Spencer Arbuckle, *The University of Western Ontario*

Supervisor: Diedrichsen, Jörn, *The University of Western Ontario*

Co-Supervisor: Pruszynski, Andrew, *The University of Western Ontario*

A thesis submitted in partial fulfillment of the requirements for the Doctor of Philosophy degree in Neuroscience

© Spencer Arbuckle 2021

Follow this and additional works at: <https://ir.lib.uwo.ca/etd>



Part of the [Computational Neuroscience Commons](#), and the [Systems Neuroscience Commons](#)

Recommended Citation

Arbuckle, Spencer, "Brain Representations of Dexterous Hand Control: Investigating the Functional Organization of Individuated Finger Movements and Somatosensory Integration" (2021). *Electronic Thesis and Dissertation Repository*. 7997.

<https://ir.lib.uwo.ca/etd/7997>

This Dissertation/Thesis is brought to you for free and open access by Scholarship@Western. It has been accepted for inclusion in Electronic Thesis and Dissertation Repository by an authorized administrator of Scholarship@Western. For more information, please contact wlsadmin@uwo.ca.

Abstract

Using our hands to manipulate objects in our daily life requires both dexterous movements and the integration of somatosensory information across fingers. Although the primary motor (M1) and somatosensory cortices (S1) are critical for these two complementary roles, it is unclear how neural populations in these regions functionally represent these processes. This thesis examined the functional organization of brain representations (the representational geometry) in M1 and S1 for dexterous hand control and somatosensory processing. To that end, representational geometries were estimated from fine-grained brain activity patterns measured with functional MRI (fMRI). Since fMRI measures a blood-based proxy of neural activity, any non-linearities in the coupling between neural activity and the fMRI signal could distort the representational geometries. Chapter 2 therefore evaluated the stability of representational geometries. Human participants made individuated finger presses at varying pressing speeds, such that overall activity was modulated across a broad range.

Representational geometries were relatively stable across pressing speeds in M1 and S1, validating the use of this analysis framework with fMRI data. Chapter 3 then explored how M1 is organized for dexterous hand control. In agreement with previous research, representations of each finger were quite distinct. However, representations of the same finger moving in different directions were very similar. Insight into this observation was gained by comparing the fMRI results to neural spiking data recorded in monkeys trained to perform an identical task. By leveraging the complementary perspectives offered by fMRI and spiking, a new organization of M1 for finger control was proposed. Chapter 4 then examined how somatosensory inputs from multiple fingers are integrated in S1. The full nature of this integration is unknown. Here, human participants experienced simulation of all possible single- and multi-finger combinations. Representational model analyses revealed that unique non-linear interactions between finger sensory inputs occur throughout S1, with stronger (and more spatially distant) interactions occurring in posterior S1. Altogether, these results provide new insight into how M1 and S1 are functionally organized to serve the motoric and sensory processes of the hand, and more broadly demonstrate how fMRI can be used to make inferences about the underlying functional organization of brain representations.

Summary for Lay Audience

Hand movements, like playing the piano or typing, are central in our everyday lives. These movements require fine control of individual fingers. Moreover, hand movements require that we also use sensory information from our fingers to better control object(s) in our hands. Although this sounds laborious, using our hands often feels effortless, suggesting that neurons in the brain are organized in such a way as to support these processes. In this thesis, I investigated how two brain regions, the primary motor cortex (M1) and primary somatosensory cortex (S1), are organized to control dexterous hand movements and integrate sensory information from the fingers. Understanding how M1 and S1 are organized for hand control is important because these regions are often damaged in brain diseases such as stroke. To study this, I used functional magnetic resonance imaging (fMRI) in healthy human participants. This technique non-invasively measures brain activity. However, fMRI does not measure neural activity directly. Therefore, there are several caveats that we must be aware of when using fMRI to draw conclusions about neural processes in the brain. Therefore, in my first project, I validated my analysis framework for fMRI data to ensure that some of the assumptions I make in my analyses are not violated. Having validated my analysis framework, I then investigated the relationships between patterns of brain activity (i.e., representations) in M1 that are evoked by movements of individual fingers in different directions. I found that the representations for different fingers were organized according to how we move our fingers in our daily lives. In other words, fingers that commonly move together are represented more similarly in M1. Furthermore, representations of the same finger moving in opposing directions were more similar than expected, given that such movements cannot co-occur in daily life. My findings suggest that groups of neurons that are involved in controlling opposing muscular patterns are closely linked in M1. In my last project, I used fMRI to study how sensory inputs from different fingers are integrated in S1. This integration process is important because it allows us to build information about an object in our hand (e.g., shape, size). To study how sensory inputs from the fingers are integrated, I stimulated all 31 possible single- and multi-finger combinations. I found that inputs from the fingers are integrated in unique ways depending on which fingers are stimulated, and that these inputs are entirely integrated in S1. Together, my work provides insight into how M1 and S1 are organized to enable dexterous hand control.

Keywords

Hand control, primary motor cortex, primary somatosensory cortex, movement, sensory integration, fMRI, MVPA, representational analysis

Co-Authorship Statement

I conducted the research presented in this thesis in collaboration with my supervisors, Dr. Jörn Diedrichsen and Dr. J. Andrew Pruszynski. I was supported by a doctoral scholarship from NSERC (PGSD3-519263-2018). The work presented in the chapters of this thesis have either been published (Chapters 2 and 3) or are about to be submitted (Chapter 4).

Chapter 2: **Arbuckle SA, Yokoi A, Pruszynski JA, Diedrichsen J** (2019) Stability of representational geometry across a wide range of fMRI activity levels. *NeuroImage* 186: 155–163.

I was the lead of this study and was actively involved in all aspects of the project (experiment design, data collection, data analysis, and writing). AY aided in data collection; JD and JP helped review and edit the paper.

Chapter 3: **Arbuckle SA, Weiler J, Kirk EA, Rice CL, Schieber M, Pruszynski JA, Ejaz N, Diedrichsen J** (2020) Structure of population activity in primary motor cortex for single finger flexion and extension. *Journal of Neuroscience* 40: 9210-9223.

I was the lead of this study and was actively involved in all aspects of the project (conceptualization, experiment design, data collection, data analysis, and writing). NE helped design the experiment; JW, EK, and CR helped collect the EMG data; MS provided the neural spiking data; JD and JP helped review and edit the paper.

Chapter 4: **Arbuckle SA, Pruszynski JA, Diedrichsen J**. Mapping the integration of sensory information across fingers in human sensorimotor cortex

I was the lead of this study and was actively involved in all aspects of the project (conceptualization, experiment design, data collection, data analysis, and writing). JD and JP helped review and edit the manuscript.

Acknowledgments

Science is a team effort. I would be remiss to not recognize the countless people that have played important roles in my studies and research, either as supervisors, mentors, friends, or any combination therein. Because an exhaustive list is just not possible, I here recognize the support and efforts of those that were most impactful:

- Jörn Diedrichsen, for (above all) being an excellent teacher, supervisor, and scientist
- Jedrzej (Andrew) Pruszynski, for his supervision, support, and clarity in writing
- Mentors and friends: Naveed Ejaz, Jeff Weiler, Björn Herrmann, and Molly Henry
- My advisory committee: Paul Gribble, Julio Martinez-Trujillo, and Jessica Grahn
- “Superlab” members: notably Eva Berlot, Nicola Popp, and Dimitri Palidis
- CFMM staff: Trevor Szekeres, Scott Charlton, and Joe Gati
- My numerous co-authors for their efforts and expertise
- My parents: Rosanne Ashley and Grant Arbuckle, and sister: Madeleine Arbuckle
- My partner: Megan Roussy, for her never-ending patience and support
- Our cat: Lionus, for his antics and desultory motor skills
- My climbing partners: Andrew Ross, Jake Artibello, and Matt McCormick, for keeping me off the ground

Table of Contents

Abstract.....	ii
Summary for Lay Audience.....	iii
Co-Authorship Statement.....	v
Acknowledgments.....	vi
Table of Contents.....	vii
List of Figures.....	x
List of Appendices.....	x
List of Tables.....	x
Chapter 1.....	1
1 General Introduction.....	1
1.1 Preamble.....	1
1.2 How is the primary motor cortex (M1) organized for dexterous hand control?.....	3
1.2.1 M1 as a somatotopic map.....	4
1.2.2 M1 as a muscle map.....	5
1.2.3 An ethological organization of M1.....	7
1.3 How does the primary somatosensory cortex (S1) process sensory input from the fingers?.....	9
1.3.1 Relay of somatosensory signals from the periphery to S1.....	11
1.3.2 Integrating sensory information across fingers in S1.....	12
1.4 Measuring brain representations with functional magnetic resonance imaging (fMRI).....	16
1.4.1 fMRI measures excitatory postsynaptic activity, not spiking.....	20
1.4.2 fMRI provides a coarse measurement of population activity.....	21
1.4.3 Interpretations of fMRI assume linear and stable neurovascular coupling.....	22
1.5 Thesis overview.....	24
1.6 References.....	25
Chapter 2.....	37
2 Stability of representational geometry across a wide range of fMRI activity levels ...	37
2.1 Abstract.....	37
2.2 Introduction.....	38
2.3 Methods.....	40
2.3.1 Participants.....	40
2.3.2 Apparatus and stimuli.....	42
2.3.3 Behavioural task.....	42
2.3.4 fMRI data acquisition.....	43
2.3.5 Preprocessing and first-level model.....	43
2.3.6 Region of interest (ROI) definitions.....	44

2.3.7	Multivariate fMRI analysis	45
2.3.8	Stability of the representational geometry across stimulation-frequencies	46
2.3.9	Reliability of representational geometries	47
2.3.10	Bayesian analysis to quantify the evidence for no RDM distortion	48
2.4	Results	49
2.5	Discussion	59
2.5.1	Conclusion	62
2.6	References	63
Chapter 3		66
3	Structure of population activity in primary motor cortex for single finger flexion and extension	66
3.1	Abstract	66
3.2	Introduction	67
3.3	Methods	69
3.3.1	Human participants	69
3.3.2	Experimental design of human finger individuation task	69
3.3.3	fMRI acquisition and analysis	72
3.3.4	EMG recording and analysis	78
3.3.5	Experimental design of monkey finger individuation task	79
3.3.6	Analysis of single cell spiking data	80
3.3.7	Kinematic finger model RDM	81
3.3.8	Experimental design and statistical analysis	82
3.4	Results	83
3.4.1	M1 fMRI activity patterns differ strongly for different fingers, not for direction	83
3.4.2	Similarities of cortical representations for presses in different directions cannot be explained by the patterns of muscle activity	88
3.4.3	M1 spiking output differs equally for fingers and direction	91
3.4.4	Spatial organization of finger- and direction-related fMRI patterns	96
3.5	Discussion	97
3.6	References	103
Chapter 4		107
4	Mapping the integration of sensory information across fingers in human sensorimotor cortex	107
4.1	Abstract	107
4.2	Introduction	107
4.3	Results	109

4.3.1	Finger stimulation evokes broadly distributed activity in sensorimotor cortex.....	109
4.3.2	Increasing overlap of single-finger patterns in sensorimotor cortex	112
4.3.3	Interactions between finger activity patterns explain spatial complexity of multi-finger patterns.....	114
4.3.4	Interactions do not only arise between adjacent fingers	118
4.3.5	Complexity of finger interactions increases along sensorimotor cortex.	118
4.3.6	Finger interactions do not reflect a general suppression of activity	119
4.4	Discussion.....	120
4.5	Methods.....	124
4.5.1	Participants.....	124
4.5.2	Stimulation apparatus.....	124
4.5.3	Finger stimulation task.....	126
4.5.4	fMRI acquisition and analysis	128
4.5.5	Estimating single-finger selectivity	130
4.5.6	Multivariate fMRI analysis	132
4.5.7	Representational model analysis.....	133
4.5.8	Statistical analyses	137
4.6	References.....	139
Chapter 5	145
5	General discussion	145
5.1	Can fMRI be used to make inferences about the neural population code?.....	146
5.1.1	fMRI does not measure spiking	146
5.1.2	fMRI is spatially biased	148
5.1.3	Stability of representational analyses of fMRI data.....	151
5.1.4	Temporal resolution of fMRI.....	152
5.2	Can single-finger movements tell us anything about how M1 is organized to control dexterous hand movements?.....	153
5.3	The feature fallacy: Does the brain encode movements or muscles?	155
5.4	How is M1 organized to control dexterous hand movements?.....	158
5.5	Why integrate somatosensory information across fingers?	161
5.6	Conclusion	166
5.7	References.....	166
Appendices	172
Curriculum Vitae – Spencer A. Arbuckle	175

List of Figures

Figure 1.1: Proposed organizations of primary motor cortex	6
Figure 1.2: Subdivisions of primary motor and somatosensory cortex	13
Figure 1.3: Analysis of fMRI data	18
Figure 2.1: Experimental paradigm	41
Figure 2.2: Scaling of fMRI activity patterns	51
Figure 2.3: Multidimensional scaling of group average representational geometries	53
Figure 2.4: Stability of representational geometry across stimulation frequencies	54
Figure 2.5: The effect of RDM distortions on representational model comparisons.....	58
Figure 3.1: Experiment paradigms.....	71
Figure 3.2: fMRI activity patterns for finger flexion and extension in human M1	85
Figure 3.3: Representational structure of fingers and direction in human M1	87
Figure 3.4: Quantifying similarity of muscle activity patterns during finger flexion and extension	90
Figure 3.5: Analysis of M1 spiking activity during monkey single finger flexion and extension	92
Figure 3.6: Comparing strength of finger and direction representations across datasets .	94
Figure 3.7: Summary model of M1 organization.....	99
Figure 4.1: Activation and representation of fingers in the sensorimotor cortex	111
Figure 4.2: Finger tuning in the sensorimotor cortex	113
Figure 4.3: Multi-finger activity patterns in the somatosensory cortex	117
Figure 4.4: Experiment paradigm	125
Figure 5.1: Slipping stimulator device.....	165

List of Appendices

Appendix A: fMRI behavioural ethics approval.....	172
Appendix B: Behavioural ethics approval (for EMG experiment).....	173
Appendix C: Article reuse permissions (Chapter 2)	174
Appendix D: Article reuse permissions (Chapter 3).....	174

List of Tables

Table 2.1: Finger pressing behaviour during MRI data acquisition.	50
--	----

Chapter 1

1 General Introduction

1.1 Preamble

The human hand is beautifully complex. We not only use our hands to perform daily tasks like manipulating tools and typing, but to also convey emotion through touch, as a communicative aid via hand gestures and sign language, and as creative instruments to create art and music. Given the central role that the hand plays in human behaviour, a natural question to ask is how does the brain control the hand?

Charles Bell argued that the beauty and utility of the hand was evidence of a divine creator (Bell 1834). If this were true, one might presume that the circuits and structures that control hand movements are neatly organized and arranged. This, however, is not the case. The sensorimotor systems that are involved in hand control are broadly distributed throughout the nervous system. Muscle contractions that produce hand movements are evoked by spinal motor neurons, which receive projections from both cortical and subcortical regions that are themselves embedded in broad, interconnected networks. The complexity of this organization arises because these sensorimotor systems have slowly emerged over time to produce ever more ethologically suitable behaviours (Cisek 2019). The developmental slog of evolution is indeed progressive, but it does not result in neatly organized systems because evolution can only operate with what is immediately available (Jacob 1977). I highlight all of this to make the point that several levels of the sensorimotor system (spinal, subcortical, and cortical) are involved in controlling the hand, and that there is no single compact circuit.

However, this thesis is not concerned with understanding the entirety of all circuits relevant for hand control. Rather, I focus on the neural populations that are critical for the two fundamental roles that the hand serves in our everyday life. First, the hand is a medium for motor activity, allowing us to interact with the surrounding world with great dexterity. Second, the hand is an active sensory organ, providing sensory information that important for future behaviour. The neural populations that primarily control dexterous

movements and process sensory inputs from the fingers reside in the primary motor (M1) and somatosensory (S1) cortices (Lemon 2008; Rathelot and Strick 2009). Therefore, in my thesis, I examine how the distributed population activity in M1 and S1 relate to the two roles that hand plays in our daily life.

To study this, I use multivariate representational analyses of functional magnetic resonance imaging (fMRI) data collected from human participants. In brief, the first project (Chapter 2) examines the stability of multivariate representational analysis of fMRI data. The degree to which brain representations measured with fMRI are stable has important implications for the kinds of inferences one can make with this analysis framework, and it has direct implications for the rest of the work presented in my thesis. In the second project (Chapter 3), I examine how neural populations in M1 are organized to control fine individuated finger flexion and extension movements. Finally, in the last project (Chapter 4), I examine how tactile inputs from multiple fingers are integrated in the sensorimotor cortex.

Given the focus of my thesis, I forgo an exhaustive literature review about the sensorimotor control of the hand in the following opening chapter. Instead, I will focus on providing a more detailed introduction to the key neuroscientific and technical concepts that underlie the work presented in my thesis. The introduction is organized into three sections. In the first section, I briefly review the anatomical architecture that links the motor cortex with the hand and consider how neural populations in the primary motor cortex are organized for dexterous hand control. In the second section, I discuss how neural populations in the somatosensory cortex processes and integrate sensory input from the fingers. In the third section, I discuss how we use multivariate analyses of fMRI data to make inferences about the organization of representations in the brain. I discuss the relationship between neural population activity and distributed fMRI activity patterns, and highlight a series of caveats that must be considered when making inferences about the underlying neural code. These considerations have important implications for the work presented in my thesis.

1.2 How is the primary motor cortex (M1) organized for dexterous hand control?

Consider dexterous hand movements like writing, playing the piano, or folding origami. These movements involve fine fractionated control of individual fingers. How does the brain execute such fine control over them? Although several cortical and subcortical regions appear to be recruited during control of hand movements, the primary motor cortex (M1) is paramount for the dexterous control of the hand. Three lines of evidence support this.

First, M1 provides substantial inputs to both cortical (i.e., corticospinal) and subcortical (i.e., rubrospinal and reticulospinal) descending pathways (Russell and DeMyer 1961; Dum and Strick 1991; Morecraft et al. 2013; Rathelot and Strick 2006), all of which ultimately influence motor neuron pools in the ventral horn of the spinal cord. Lesioning either of these pathways results in a loss of dexterous movements (Tower 1940; Lawrence and Kuypers 1968; Lawrence and Hopkins 1976; Sasaki et al. 2004; Kinoshita et al. 2012).

Second, there are a substantial number of monosynaptic corticospinal projections that originate from M1 and synapse directly with motor neurons in the spinal cord (Bernhard and Bohm 1954; Strick and Preston 1982; Lemon 2008; Rathelot and Strick 2009). Much of these monosynaptic projections terminate in motor neurons pools that innervate distal hand muscles, perhaps allowing for more precise control over hand muscles (Phillips and Porter 1964; Clough, Kernell, and Phillips 1968; Asanuma et al. 1978; Shinoda, Yokota, and Futami 1981). Indeed, primates with greater finger individuation abilities appear to have greater numbers of these monosynaptic projections that arise from M1 (Heffner and Masterton 1983; Bortoff and Strick 1993; Lemon 2008).

Third, M1 lesions in monkeys result in substantial loss of manual dexterity, such as the ability to perform a precision grip of objects between the thumb and index finger (Passingham, Perry, and Wilkinson 1983; Matsumura et al. 1991; Schieber and Poliakov 1998; Bashir et al. 2012). Due to the distributed nature of the systems involved in hand control, these monkeys do not entirely lose the ability to use the affected hand and often

regain some skillful abilities (Murata et al. 2008); however, this recovery always appears incomplete (Rouiller et al. 1998; Liu and Rouiller 1999; Darling et al. 2014). Recovery of precise hand movements is even more incomplete in human stroke patients. Patients who have damage to the hand area of M1 have clear deficits in dexterous hand movements (Lang and Schieber 2004) that persist even after one year post-stroke (Ejaz et al. 2018). Thus, not only are neural populations in M1 involved in dexterous hand control, they are critical for this behaviour.

The spiking outputs from M1 to motor neuron pools in the spinal cord ultimately contain the muscle commands necessary to produce dexterous hand movements (Kakei, Hoffman, and Strick 1999). It is unclear, however, how neurons in M1 are organized to exert tight control over the complex musculoskeletal system of the primate hand. Do they spatially cluster according to finger preference, or according to individual muscles? Or is the organization more spatially diffuse? Perhaps neural populations are functionally organized, such that movements that tend to co-occur are represented in overlapping neural substrates and lack clear modularity. Here, I briefly consider each of these hypotheses and discuss their shortcomings. I conclude by highlighting why, from an ethological perspective, the simplest organization is one that is dictated by the statistics of everyday movements.

1.2.1 M1 as a somatotopic map

Initially, M1 was hypothesized to contain a map of different body parts, each represented by non-overlapping groups of neurons (Jackson 1870; Fritsch and Hitzig 1870; Penfield and Boldrey 1937). Thus, fingers were predicted to be represented by distinct groups of non-overlapping neurons in M1, with each neuron in each finger cluster being tuned to only movements of that finger. Under this organization, when we move our index finger, neurons in the index finger region become active. To move our middle finger, neurons in the middle finger region become active. The evidence for this somatotopic organization came from brain stimulation studies in various animals and human patients that elicited movements of specific limbs when specific cortical sites were stimulated (see Phillips 1973 and Taylor and Gross 2003 for reviews). This somatotopic model was the dominant theory of M1 organization for some time, and its popularity is evident from the continued

use of the pictorial representation of the motor homunculus (Fig. 1.1A; Penfield and Rasmussen 1950). This organization is also not *wrong* – there is indeed evidence for a broad somatotopic ordering (i.e., a gradient) of finger representations in M1, with the thumb being represented in more ventral regions of M1 and the little finger being more represented in dorsal regions (Beisteiner et al. 2001; Hlustík et al. 2001; Indovina and Sanes 2001; Dechent and Frahm 2003). However, studies consistently report that finger somatotopy in M1 is not strictly defined. Instead, finger representations in M1 are highly overlapping and fractured (Nudo et al. 1992). Similar observations are reported in human fMRI studies, where regions of activity evoked by single finger movements are also highly overlapping and diffuse (Sanes et al. 1995; Beisteiner et al. 2001; Hlustík et al. 2001; Indovina and Sanes 2001; Ejaz, Hamada, and Diedrichsen 2015). Furthermore, individual neurons in the hand region of M1 are not tuned to single fingers (as predicted under a strict somatotopic organization) but rather have broad and heterogenous tuning to multiple fingers (Schieber and Hibbard 1993; Schieber 2002). Therefore, somatotopy alone cannot explain the organization of neural populations in M1. To be fair, such a strict interpretation was never emphasized by Penfield (Penfield and Boldrey 1937), but the continued use of the motor homunculus as a didactic tool in neuroscience textbooks has obscured this because the homunculus does not necessarily distinguish between a strict somatotopic organization and a somatotopic gradient in M1.

1.2.2 M1 as a muscle map

One possible explanation for the overlap of finger representations is that neural populations in M1 are not tuned to a specific limb per se, but are rather tuned to individual muscles (Foerster 1936; Chang, Ruch, and Ward 1947). Thus, the overlap of limb representations in M1 would reflect the degree to which similar sets of muscles are recruited to move each limb. Penfield argued against this organization, stating that “the cortical motor sequence of man shows little preservation of the segmental representations of muscles found in the spinal cord and brain stem” (Penfield 1947). However, others argued that at some level, limbs must be represented by their constituent muscles (Chang, Ruch, and Ward 1947). Strong evidence to support the single muscle organization emerged after advances in microstimulation techniques allowed for much more precise

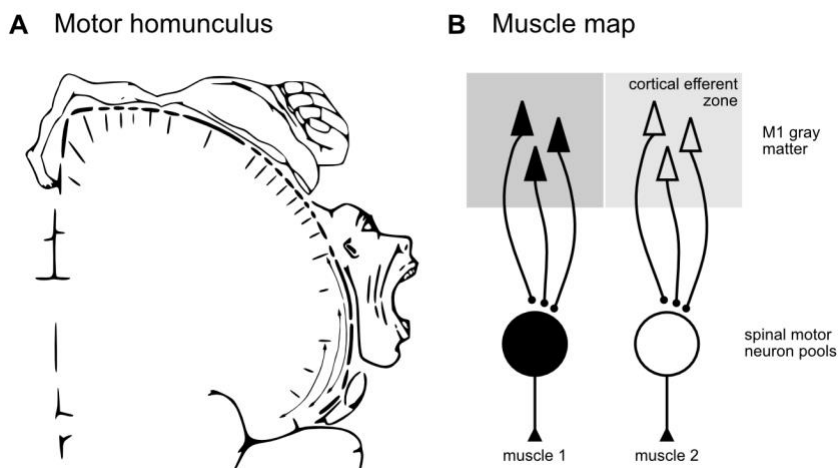


Figure 1.1: Proposed organizations of primary motor cortex

(a) The motor homunculus, arranged on a cross-section of the primary motor cortex (M1). Under this organization, each part of the body is represented at a focal point in M1. Figure reproduced under the CC BY-SA 4.0 license and was obtained from https://en.wikipedia.org/wiki/Cortical_homunculus#/media/File:Motor_homunculus.svg

(b) Schematic of the single muscle map proposed by Asanuma and Rosen (1972). Under this organization, each muscle would have a unique, clustered representation (“efferent zone”) in M1. The neurons in this cluster would represent only the corresponding muscle. These zones have strict borders and were hypothesized to rarely overlap, if at all.

stimulation in the cortex (Asanuma and Sakata 1967; Stoney, Thompson, and Asanuma 1968). Asanuma and Rosen (1972) demonstrated that low-threshold intracortical stimulation evoked activity of single muscles in primates. They hypothesized that neurons in M1 were spatially clustered into “cortical efferent zones” for each muscle, that the efferent zone of different muscles did not spatially overlap, and that the output of each zone innervated a single motor neuron pool in the spinal cord (Fig. 1.1B; Asanuma and Rosen 1972; Asanuma 1975; Asanuma et al. 1978).

Three clear lines of evidence argue against this organization. First, cortical neurons that project to single motor neuron pools are broadly distributed and highly overlapping in M1, not arranged in discrete, non-overlapping efferent zones (Landgren, Phillips, and Porter 1962; Jankowska, Padel, and Tanaka 1975; Andersen et al. 1975; Rathelot and Strick 2006, 2009). Second, the spiking activity of single neurons in M1 covary with the activity of several muscles of the upper forelimb, not single muscles (Fetz, Cheney, and German 1976; Fetz and Cheney 1980; Cheney and Fetz 1985; Buys et al. 1986; McKiernan et al. 1998). Third, the majority of corticospinal projections from M1 are not monosynaptic and instead exert influence on motor neurons via spinal interneurons. These premotor interneurons produce facilitation in multiple hand muscles, not just a single muscle (Takei and Seki 2010). These findings suggest that neurons in M1 are tuned not to single muscles, but rather groups of muscles. If neurons are tuned to groups of several muscles, what is the organizational principle that dictates muscle grouping? In the next section, I approach an answer to this question from an ethological perspective.

1.2.3 An ethological organization of M1

From an ethological perspective, it should not be very surprising that neural populations in M1 are not strictly organized according to specific fingers or single muscles. Everyday movements of the hand often involve multiple fingers moving in concert. For example, manipulating a small clasp on a piece of jewelry requires several different fingers moving together to operate the clasp while simultaneously stabilizing the piece of jewelry. If neurons in M1 are critical for producing such complex behaviour, why would they be arranged to represent each finger (muscle) separately given that they so rarely move (contract) in isolation? Therefore, an alternative organization for hand control in M1 is

that neurons are organized based on the statistics of everyday movements. Specifically, the fractured and overlapping nature of fingers representations comes about due to movement co-occurrence, with fingers that commonly move together being represented more similarly in M1. Importantly, this hypothesis does not suggest that M1 represents movements and not muscles (Phillips 1975; Kakei, Hoffman, and Strick 1999). Instead, this hypothesis suggests that any underlying feature (e.g., movement or muscle combinations) will be represented in a manner that is structured by the statistics of everyday actions¹. Thus, if neurons in M1 explicitly represent muscles, then the underlying organization of these muscle representations would be dictated according to recruitment patterns in everyday life.

The idea that M1 is organized according to ethologically relevant movements is not new. Ferrier (1875) electrically stimulated areas of the brain, noting that long-duration electrical stimulation in M1 produced complex, multi-joint movements. More recently, Graziano and colleagues (2002) revisited this idea and performed long-duration electrical stimulation in M1 and premotor cortex of monkeys. The authors noted that this stimulation produced complex, multi-joint movements, and that the movements appeared to have behavioural relevance. For example, some of the elicited movements involved bringing the hand to the mouth (presumably in reference to eating from the hand) or reaching with the arm. Therefore, instead of single body parts or individual muscles, Graziano and colleagues hypothesized that neural populations in M1 are organized according to ethologically-relevant movements (Graziano and Aflalo 2007). That this organizational principle extends to fine finger movements was demonstrated using transcranial magnetic stimulation (TMS) of M1. Gentner and Classen (2006) reported that the kinematics of multi-finger twitches evoked by TMS of M1 resembled the kinematic structure of everyday hand movements. To then demonstrate that is organization is shaped by the statistics of everyday movement, Gentner and colleagues (2010) studied multi-finger twitches evoked in musicians by M1 TMS. They reasoned

¹ This is an important point, and so I expand on this idea in the Discussion section (Chapter Five).

that professional musicians (like violinists) will have different movement statistics of the hand because they train highly specific patterns of hand movements, and this experience should alter the kinds of movements evoked by stimulating M1. To test this, they applied TMS to M1 and found that the multi-finger twitches evoked in professional musicians did indeed contain kinematic features that were not present in non-musician controls.

Although these studies demonstrated that stimulation evokes movements that resemble everyday actions, it is possible that such structure arises in populations downstream from M1. Therefore, to directly examine how M1 is organized, Ejaz and colleagues (2015) used multivariate analyses of fMRI activity patterns to examine the organization of single- and multi-finger representations in human M1. They demonstrated that the co-occurrence of finger movements during everyday activities fully predicted the measured organization of finger representations in M1. Furthermore, predictions from a muscle and a somatotopic model performed significantly worse at explaining the organization of measured finger representations.

Demonstrating that movement co-occurrence fully explains the similarities between finger representations is the first step to testing the hypothesis that M1 is organized according to the statistics of everyday movements. However, everyday hand movements (such as typing) involve several fingers moving in different directions. Under this hypothesis, one would predict that since movements of the same finger in different directions cannot temporally co-occur, these movements must be represented by distinct, non-overlapping neural substrates in M1. In **Chapter 3**, I put this prediction to a critical test by investigating to what degree the statistics of everyday hand movements can predict the relationship between M1 representations for movements of the same finger in different directions.

1.3 How does the primary somatosensory cortex (S1) process sensory input from the fingers?

When we write with a pen or interact with a cell phone, we rely on sensory information from our fingers so that we can better control the pen/phone. In order to better control a phone in our hand, somatosensory signals from each finger need to be integrated, yielding information about the phone's shape and how best to hold it. Whereas M1 is

necessary for the execution of hand movements, the primary somatosensory cortex (S1) is important for the integration of sensory information from the fingers².

Sensory information from fingers is important for hand control. Sensory signals from the fingers are relayed to S1 where they are integrated and are used for future manipulative actions. Lesions to S1 result in severe impairments of hand movements, even though M1 and the descending motor pathways are not physically impacted (Carlson 1981; Hikosaka et al. 1985; Brochier et al. 1999; Friel et al. 2005). These impairments commonly manifest as clumsy movements and deficient hand postures (for the task at hand). Why do S1 lesions produce such effects? The reason is that S1 has substantial inputs to several cortical regions involved in motor control of the hand, namely M1 and the posterior parietal cortex (Yau et al. 2016). The posterior parietal cortex is recruited during object manipulation and tool-use behaviours (Johnson-Frey 2004; Culham and Valyear 2006), and has recently been shown to have corticospinal projections that influence movements of the hand (Rathelot, Dum, and Strick 2017). S1 lesions impair the sensory information available to these regions, and the behavioural deficits that arise after S1 lesions therefore reflect the critical role that this sensory information plays in dexterous hand control.

In the context of dexterous hand control, it would be useful to be able to detect any unique combination of stimulation across the fingers. This detection would allow for a flexible mapping between patterns of somatosensory inputs from the fingers and motor responses. This leads to a fundamental question: how are somatosensory signals from the fingers integrated? Understanding how sensory inputs are integrated across the fingers is important because this integrated information is used to shape behaviour. Moreover, it can provide insight into the kinds of computations that are necessary in order to provide behaviourally-relevant sensory feedback from neural prostheses (Suminski et al. 2010; Abbasi et al. 2020; Flesher et al. 2021). In the following sections, I therefore examine how sensory inputs are integrated across fingers in human S1. I start by briefly reviewing

² Note that these processes are not exclusively performed by either region, but rather, neural populations in each region are more implicated in each process.

how somatosensory signals from the periphery are relayed to S1, and then consider the subregions of S1 and their respective roles in processing somatosensory signals.

1.3.1 Relay of somatosensory signals from the periphery to S1

I start with considering how the somatosensory signals are relayed from the periphery to S1. There are two broad classes of somatosensory information that are important for object manipulation. Cutaneous signals reflect contact events of an object with the skin of the hand, and proprioceptive signals reflect information about movement and hand posture (Hsiao and Yau 2008; Yau et al. 2016). Proprioceptive signals arise from golgi tendon organs, joint receptors, and muscle spindles, and cutaneous signals arise from mechanoreceptors in the glabrous skin of the hand³. There are four categories of mechanoreceptors, each responding to different features of contact events (Johansson and Vallbo 1983). Meissner endings (fast-adapting type I) transduce low-frequency vibrations and movement across the skin, and are sensitive to local spatial discontinuities like edges. Merkel endings (slow-adapting type I) transduce low-frequency vibrations and static indentations, and are sensitive to local spatial features. Pacinian endings (fast-adapting type II) transduce high-frequency vibrations, reflecting texture. Ruffini endings (slow-adapting type II) transduce skin stretch (Johansson and Flanagan 2009). All mechanoreceptors are stimulated when we dexterously manipulate objects with our hands.

These somatosensory signals from the upper-limb are relayed from the periphery via the cuneate nucleus to the ventral posterior lateral (VPL) nucleus of the thalamus. Although the cuneate and VPL appear to play an important role in gain control of sensory inputs (Azim and Seki 2019) and cross-modal integration (in cats: Jörntell et al. 2014), signals specific to each finger remain largely segregated (Florence, Wall, and Kaas 1988, 1989).

³ Mechanoreceptors can also convey proprioceptive information. For example, the skin of the hand will stretch along certain directions when moving the hand from one posture to another, and this stretch stimulates Ruffini endings.

From the VPL, the signals are relayed to S1. It is here in S1 that the sensory signals from different fingers substantially interact (Hsieh et al. 1995).

The primary somatosensory cortex of humans can be divided into four cytoarchitecturally distinct Brodmann areas (BA): 3a, 3b, 1, and 2 (Brodmann 1909; Powell and Mountcastle 1959). Most thalamic inputs are to BA 3a and 3b (Fig 1.2), with progressively fewer inputs to BA 1 and BA 2 (Jones and Powell 1970; Jones 1975; Shanks and Powell 1981). Instead, BA 1 and BA 2 receive substantial inputs from BA 3b (Burton and Fabri 1995). Furthermore, the average receptive fields of neurons in each region become increasingly broad, with neurons in BA 3b predominantly responding to stimulations at specific fingers, whereas receptive fields in BA 2 span multiple fingers (Hyvärinen and Poranen 1978; Sur, Merzenich, and Kaas 1980; Iwamura et al. 1993). That neural receptive fields broaden from BA 3 to BA 2 has often been interpreted as evidence that inputs from the different fingers are progressively integrated along S1 (Iwamura 1998).

1.3.2 Integrating sensory information across fingers in S1

As previously mentioned, it would be advantageous to be able to detect any arbitrary pattern of stimulation across the fingers for dexterous hand control. Such a detection ability would require that stimulation of each multi-finger pattern is uniquely represented in S1. In this section, I review what is currently known about the integration of sensory inputs across fingers in S1. To this end, I also briefly discuss how sensory inputs from multiple whiskers in rodents are integrated in the barrel cortex.

Previous experiments that have studied tactile signal integration from the fingers typically use simultaneous two-finger stimulation paradigms. The neural responses to two-finger stimulation are then compared against responses evoked during single-finger stimulation. At the single-neuron level, spike rates evoked during two finger stimulation are generally lower than expected if the individual finger responses were summed, although there are a few instances of increased firing rates (Reed et al. 2010). These suppressive effects are reported in BA 3b (Friedman, Chen, and Roe 2008; Lipton et al.

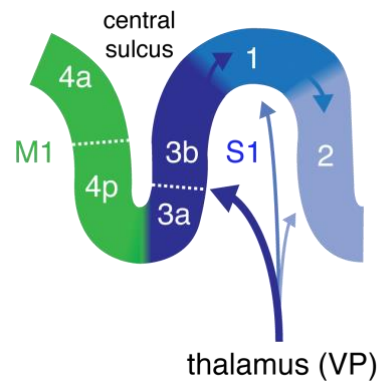


Figure 1.2: Subdivisions of primary motor and somatosensory cortex

The primary somatosensory cortex (S1) can be subdivided into 4 cytoarchitectonically distinct subdivisions: BA 3a, 3b, 1, and 2 (Brodmann 1909; Powell and Mountcastle 1959). BA 3a and 3b receive the brunt of thalamic inputs, and BA 1 and 2 receive progressively fewer. BA 3 projects to BA 1 (and 2), and BA 1 projects heavily to BA 2. This projection architecture has been interpreted to suggest that somatosensory inputs are progressively processed along S1. The primary motor cortex is also displayed here, and can be subdivided into 2 cytoarchitectonically distinct subdivisions: BA 4a and 4p (Geyer et al. 1996). Thalamic inputs to M1 are not shown in this figure.

2010; Thakur, Fitzgerald, and Hsiao 2012) and BA 1 (Friedman, Chen, and Roe 2008). Similar observations have been made in human participants using non-invasive measurements that average the activity across neural populations in these regions (Gandevia, Burke, and McKeon 1983; Hsieh et al. 1995; Biermann et al. 1998; Ishibashi et al. 2000; Hoechstetter et al. 2001; Ruben et al. 2006; Brouwer et al. 2015). The general suppressive effect appears to increase from BA 3b to BA 2, and this is interpreted as evidence that sensory inputs from the fingers interact to a greater degree in the posterior S1 (Ruben et al. 2006).

Furthermore, in BA 3b, greater sub-linear suppression occurs between inputs from spatially close regions on the hand, with few interactions occurring between inputs from distant points (Reed et al. 2008, 2010), suggesting that initial interactions in S1 occur between spatially close regions on the hand. Further support for this idea comes from the observation that neurons in BA 3b respond to spatially local tactile features like edge orientation, which can be extracted from inputs from a single finger (Bensmaia et al. 2008). It is hypothesized that interactions between more spatially distant points on the hand arise in BA 1 and BA 2, because the kinds of tactile features that neurons in S1 respond to become more complex (Iwamura and Tanaka 1978; Bodegård et al. 2001; Yau et al. 2016). For example, neurons in BA 2 are selective for specific curvatures, which is a tactile feature that extends across multiple fingers (Yau, Connor, and Hsiao 2013). Taken together, this body of work indicates that sensory inputs from the fingers interact in S1, and appear to be progressively integrated.

However, the full nature of interactions between sensory inputs from multiple fingers are unknown. This is because previous studies have been limited to two-finger stimulation paradigms. During dexterous object manipulation in daily life, one needs to integrate sensory inputs from all five fingers (or any combination therein). In addition, it is not clear whether this suppressive interaction effect observed during two-finger stimulation reflects non-linear integration of the sensory inputs from the fingers, or a general non-linear scaling of overall activity.

To therefore provide further insight into how sensory inputs across fingers might be combined, I briefly consider how inputs from multiple whiskers are integrated in the rodent barrel cortex. Clearly whiskers and fingers differ, but the rodent whisker system is one of the most well-studied sensory systems in neuroscience and has several parallels with sensory processing of multiple fingers (i.e., integrating sensory inputs across several flexible sensors; feature extraction). Sensory inputs from the whiskers to rodent S1 are arranged in distinct topographic modules called “barrels”, where each barrel receives thalamic inputs predominately from an individual whisker referred to as the “principal” whisker (Woolsey and Van der Loos 1970). Earlier work demonstrated that the activity of single barrel cortex neurons was lower during simultaneous stimulation of the principal and non-principal whiskers, presumably to enhance the spatial contrast between the principal whiskers and those adjacent to it (Simons 1985; Brumberg, Pinto, and Simons 1996). A similar observation was made using array-recordings to study population-level activity, with multi-whisker stimulation producing a sub-linear effect across the recorded neural population (Mirabella, Battiston, and Diamond 2001), like the effects reported during two-finger stimulation. However, recent work using more extensive sets of multi-whisker combinations, stimulating up to five whiskers simultaneously, report that individual neurons in the barrel cortex are highly selective to specific multi-whisker combinations. This means that each whisker combination is uniquely represented in barrel cortex, with some neurons responding supra-linearly to specific combinations (Laboy-Juárez et al. 2019; Lyall et al. 2020). This sparse encoding is the result of unique non-linear interactions that occur between inputs from specific whiskers in the barrel cortex (not a general suppressive effect). These findings indicate that multi-whisker integration is more complex than expected if all multi-whisker combinations evoked similar sub-linear effects.

What do these results mean for multi-finger integration in S1? If combination-specific interactions are a general feature of somatosensory processing, then multi-finger integration should also result in unique representations of any arbitrary stimulus combination in S1. Therefore, in **Chapter 4**, I stimulate all 31 possible single- and multi-finger combinations to study the interactions that occur during multi-finger integration in human S1.

1.4 Measuring brain representations with functional magnetic resonance imaging (fMRI)

In this thesis, I examine how neural populations in the human brain facilitate hand control. I focus on humans because compared to other primates, the flexibility and skill humans show with their hands is unmatched. I use fMRI as a non-invasive method to measure brain activity in humans, and use multivariate analyses to make inferences about how neural populations in the brain represent⁴ different aspects of hand control.

In univariate analyses of fMRI data, patterns of fMRI activity are often smoothed and averaged across participants, yielding activation maps that show *where* there is activity in the brain for each of the different experimental conditions (Fig. 1.3A). Although useful, this analysis approach cannot provide insight into what this activity reflects. Insight into what is represented in the brain activity patterns requires multivariate fMRI analyses.

One popular multivariate approach is to decode experimental conditions from the fine-grained activity patterns within each participant. For example, it is possible to decode upcoming reaching actions from fMRI patterns in premotor and parietal brain regions (Gallivan et al. 2011). The ability to decode experimental conditions is taken as evidence that the region from which the patterns are measured represents something about the experimental conditions (Haxby et al. 2001; Haxby, Connolly, and Guntupalli 2014). In this framework, decoding is used as a tool to reveal *what* information is contained in the activity patterns, but not necessarily *how* it is represented – knowing that certain kinds of information are contained in the population activity is not the same thing as understanding how this information is structured in the underlying brain representations (Kriegeskorte and Douglas 2019). The underlying representational structure conveys not only *what* information is represented, but also *how* it is represented relative to other

⁴ Population activity patterns from the brain convey information about the world. However, the presence of information in activity patterns from a brain region does not mean that the region is functionally implicated in some process. A representational interpretation, however, implies that not only is there information about the world in the activity patterns, but that this information is used by downstream neurons/regions in a such a way that it is relevant for behaviour (deCharms and Zador 2000; Kriegeskorte and Diedrichsen 2019).

experimental conditions. Therefore, stronger insights into how the underlying neural populations are involved in computation (or behaviour) can be formulated by considering how the fMRI activity patterns relate to one another in a brain region.

To this end, I measure the degree to which pairs of activity patterns are dissimilar (Fig. 1.2B), which is a non-discretized measure of decodability (Kriegeskorte, Mur, and Bandettini 2008; Walther et al. 2016). The collection of these dissimilarities is referred to as a representational geometry and it characterizes both how strongly each condition is represented in the patterns (*what* is represented), and how the different conditions relate to one-another⁵ (*how* it is represented; Diedrichsen and Kriegeskorte 2017; Kriegeskorte and Diedrichsen 2019). A great strength of this approach is that the representational geometries measured in each participant can be compared to model-predicted representational geometries that hypothesize how features are represented in the brain (Fig. 1.3B).

However, there are (at least) three important caveats that we must consider when using multivariate analyses of fMRI data to make inferences about the underlying neural representations. First, fMRI does not measure spiking activity directly, but rather a proxy of neural activity that depends on the concentration of oxygenated hemoglobin in the blood. Second, the measurement unit in fMRI (a volumetric-pixel, or voxel) averages activity across tens- to hundreds-of-thousands of neurons, and thus each voxel is not sensitive to information encoded in the neural activity patterns within that voxel. This averaging also results in a much coarser spatial perspective of neural activity compared to electrophysiology. Third, the fMRI signal is related to neural events through complex neurovascular coupling. Any instability of neurovascular coupling could have severe implications for multivariate analyses of fMRI data. In the following sections, I expand

⁵ Note that the representational geometry abstracts from the spatial arrangement of the activity patterns on the cortical surface. Therefore, information about the spatial arrangement and the degree to which features representation are concentrated or distributed across the population are disregarded. Depending on the research goal, ignoring these aspects may be a disadvantage.

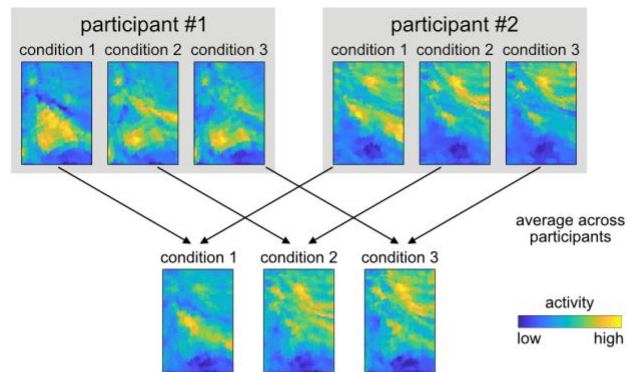
Figure 1.3: Analysis of fMRI data

(A) In univariate fMRI analyses, fMRI activity patterns are averaged across participants to yield a group-level activity map per condition, identifying what areas in the brain are active for each experimental condition. As can be appreciated in these example maps, fine spatial details from each participant are lost after averaging.

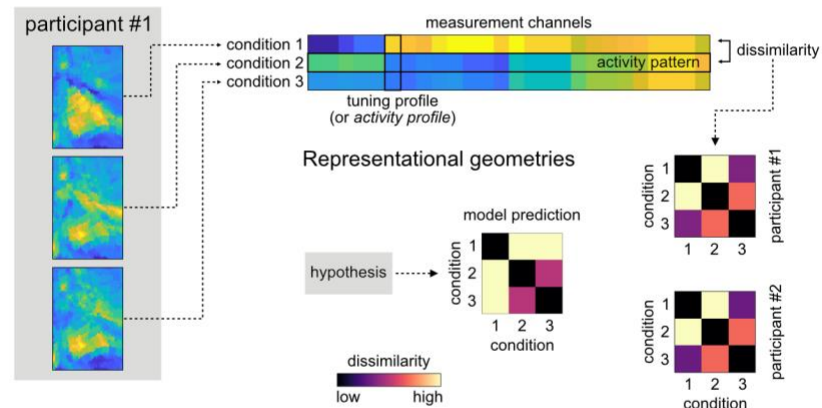
(B) In representational multivariate fMRI analysis, differences between activity patterns within each participant are summarized by calculating the paired dissimilarities between activity patterns. The collection of dissimilarities describes the representational geometry. Although the spatial patterns of each condition are quite distinct between participant 1 and 2, the relative dissimilarities between conditions are quite similar. This suggests that there is an underlying organization to these patterns across participants. To adjudicate between different organizing principles, model-predicted representational geometries are compared to the representational geometries of the participants.

(C) Schematic of the transformations that arise from stimulus presentation to measured BOLD fMRI activity patterns. The stimulus transduction can be any arbitrary linear or non-linear transformation. The neural activity representing the stimulus gives rise to hemodynamic responses, namely increases in blood-flow, blood-volume, and oxygen concentration. The changes in local magnetic susceptibility of the tissue is measured using MRI, yielding the BOLD signal measurement. The neural-to-BOLD fMRI transformation is comprised of the hemodynamic responses and the MRI measurement process. Figure is inspired from Boynton et al. (1996).

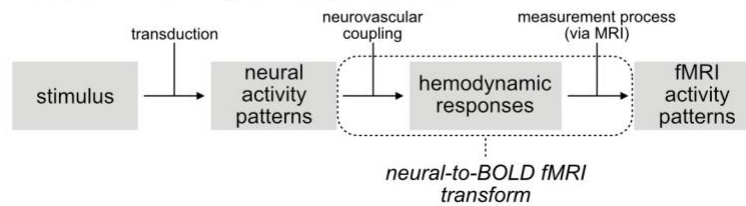
A Univariate analysis



B Representational analysis (multivariate)



C Neural-to-BOLD fMRI transformation



on these caveats and consider under what circumstances they alter the inferences one can make about the underlying neural population activities using multivariate fMRI analysis.

1.4.1 fMRI measures excitatory postsynaptic activity, not spiking

The first caveat we must consider is that fMRI does not directly measure the spiking activity of neurons. The studies presented in this thesis measure the Blood-Oxygen-Level-Dependent (BOLD) signal with fMRI (Ogawa, Lee, Kay, et al. 1990; Bandettini et al. 1992; Kwong et al. 1992; Ogawa et al. 1992). Although the BOLD signal is not a direct readout of neural spiking, it is tightly linked to neural activity. This is because neural communication in the brain involves active metabolic processes that require oxygen (Schwartz et al. 1979; Mata et al. 1980), and during increases in neural communication, the greater demand for oxygen is met by localized increases in oxygenated blood flow (Buxton, Wong, and Frank 1998). Thus, BOLD reflects neural processes that consume energy.

The greatest factor of energy consumption in the brain comes from active processes that reverse ion fluxes in postsynaptic receptors ($\geq 50\%$; Attwell and Laughlin 2001; Attwell and Iadecola 2002; Harris, Jolivet, and Attwell 2012). Both excitatory and inhibitory synaptic communication give rise to these postsynaptic events. However, because only 10-20% of cortical synapses are inhibitory (Hendry et al. 1987; Markram et al. 2004; Attwell and Iadecola 2002), the majority of metabolic activity related to synaptic transmission in the brain reflects excitatory communication. In addition, large inhibitory interneurons most often project to the initial segments of axons (DeFelipe et al. 1985) or to perisomatic regions of postsynaptic neurons (Miles et al. 1996), where the net effect of a single inhibitory input is stronger (meaning fewer inhibitory inputs are necessary). Taken together, this suggests that local energy demand in the primate brain arises predominantly from excitatory postsynaptic activity.

The increased demand for energy (oxygen and glucose) in the primate brain is met by increases in oxygenated blood flow – increases in oxygenated blood flow cause increases in the BOLD signal. The BOLD signal is sensitive to changes in the magnetic field that arise from the magnetic properties of hemoglobin, the oxygen-transport protein in red

blood cells (Pauling and Coryell 1936). In regions with more oxyhemoglobin, the BOLD signal is stronger because there is less magnetic field distortion (Ogawa, Lee, Nayak, et al. 1990; Ogawa, Lee, Kay, et al. 1990). In sum, this indicates that BOLD signal increases in a brain region reflect increased excitatory inputs and recurrent activity.

Several studies support this hypothesis. The BOLD signal is greater in cortical layers with the greatest number of excitatory synaptic inputs (Harel et al. 2006), and the BOLD signal is more strongly correlated with local field potentials than single- or multi-unit spiking outputs (Logothetis et al. 2001, 2003). In **Chapter 3**, we revisit this idea to provide a unique interpretation of our results.

1.4.2 fMRI provides a coarse measurement of population activity

The second caveat we must consider with fMRI is that there are two different signal resolutions, and these resolutions may limit the feature representations that we are sensitive to. The first resolution is the intrinsic spatial resolution of the hemodynamic response itself, which is dictated by the spatial specificity of neurovascular coupling. The good news is that this coupling appears to be fairly high resolution. With a clever design, O'Herron and colleagues (2016) demonstrated that the vasodilatory responses of individual blood vessels were tightly coupled to local synaptic activity. The authors reported that in the cat visual cortex, where neurons are spatially arranged into columns selective to stimulus orientation, the orientation tuning of individual blood vessels well-approximated the tuning of the neurons in a $\sim\frac{1}{2}$ mm diameter window around the vessel. Therefore, the hemodynamic response averages the underlying neural population responses at a spatial scale of $\sim\frac{1}{2}$ mm, which is too poor to resolve the synaptic activity of single neurons. However, when using fMRI to study brain representations, we are able to measure brain activity across a greater spatial extent than possible with neural recordings, and so there is a trade-off between spatial specificity and spatial coverage in either measurement modality.

The second limiter to spatial resolution is the resolution from the MR acquisition itself. A three-dimensional MR image is acquired over a short period of time by imaging several 2-dimensional slices (think sliced bread). Each spatial frequency of each slice requires

the readout of a gradient echo signal. The spatial resolution of each voxel in each slice is therefore limited by the time available to collect all these echoes during echo-planar BOLD imaging. Generally, faster collection leads to lower resolution voxels (but this depends on magnetic field strength and parallel imaging methods). In this thesis, I used high-field (7Tesla) MRI field strength imaging with isotropic voxel resolutions of $\sim 1.5\text{mm}$. Therefore, this means that the voxels have, to some degree, distorted the underlying neural representations. Within each voxel, the postsynaptic activity over tens- to hundreds-of-thousands of neurons have been averaged. Thus, although fMRI provides excellent spatial coverage compared to neural recordings, the spatial coverage comes at a cost.

Under what circumstances could the averaging of the fMRI measurement process distort the underlying neural representations? Let us consider an example where individual neurons are each tuned to movements of a single finger. If the neurons are broadly spatially clustered according to finger preference, then differences between fingers representations will be evident even after averaging the synaptic activities within each voxel. In contrast, if neurons tuned to different fingers are randomly intermixed, then any finger-specific signals will be strongly attenuated when averaging synaptic activity within each voxel. Therefore, fMRI is biased towards feature representations that exist at a broader spatial scale (Kriegeskorte and Diedrichsen 2016). To partly address this bias, I used higher resolution (i.e., smaller) voxels. However, the use of smaller voxels does not fully alleviate the fact that fMRI is biased towards representations that exist at a broad spatial scale. We revisit this idea again in **Chapter 3**, when we consider neural representations for fingers and movement directions.

1.4.3 Interpretations of fMRI assume linear and stable neurovascular coupling

The final caveat we must be aware of with fMRI concerns the linearity of the transformation between neural activity patterns and fMRI activity patterns (Fig. 1.3C). The analysis and interpretation of fMRI data depends on the assumption that the transformation between neural activity and fMRI activity is linear (Boynton et al. 1996). Specifically, we assume that an fMRI activity pattern (y) is the result of a constant linear

transformation function (A) of the underlying neural activity pattern (x): $y = A(x)$. This means that the same neural activity pattern will evoke the same fMRI activity pattern, and two different neural activity patterns will evoke two comparably different fMRI activity patterns. We additionally assume that A is independent of x such that the transformation between neural patterns and fMRI patterns is stable across a broad range of overall activity levels, and does not change for neural patterns in a region. It is only under these conditions that we can reliably interpret any changes in the fMRI activity patterns as being the result of changes in the underlying neural patterns.

Given the complexity of the neurovascular relationship, these assumptions may be violated to some extent. How would such violations influence fMRI analyses? For univariate fMRI analyses, any small violations of the stability of the transformation from neural to fMRI patterns would not pose too large a problem. This is because any small, idiosyncratic changes to A will be averaged out at the group-level analysis. In contrast, for multivariate fMRI analyses, violations of a stable linear transform between neural patterns and fMRI patterns would have substantially dire consequences. It would mean that the representations measured with fMRI would change based on the overall neural activity. For example, consider a ceiling effect of the BOLD signal (Siero et al., 2013). At low levels of overall neural activity, each distinct neural activity pattern would produce comparably distinct fMRI activity pattern. However, at increasing levels of neural activity, the BOLD patterns would saturate and suddenly become very similar to each other, much like over-exposed photographs. Effects like this would make representational geometries measured with fMRI difficult to compare across brain regions or patient populations where the overall signal magnitude varies. It would also lead to inappropriate inferences, such as when selecting between competing hypotheses about neural representations. Unfortunately, recent studies have reported evidence of changing nonlinearities in neurovascular coupling, meaning that fMRI inferences would depend on overall activity (Zhang, Zhu, and Chen 2008; Zhang et al. 2009; O'Herron et al. 2016). To therefore address this concern, in **Chapter 2** I experimentally tested the stability of representational geometries measured with fMRI. The work presented in Chapter 2 is critical because the remainder of the work in my thesis uses multivariate fMRI to make inferences about the underlying neural code in M1 and S1.

1.5 Thesis overview

The work presented in this thesis uses multivariate analyses of fMRI to examine how M1 is organized for individuated finger movements and how S1 integrates somatosensory information from multiple fingers. Therefore, the degree to which brain representations measured with fMRI are stable has important implications for my experiments. In **Chapter 2**, I examine the stability of brain representations measured with fMRI. In **Chapter 3**, I then examine how M1 is organized to control finger flexion and extension movements. Under the hypothesis that M1 is organized according to movement co-occurrence, one would predict that since flexion and extension of the same finger can never co-occur (from a kinematic perspective), finger flexion and extension should be associated with distinct brain representations. I tested this prediction using human fMRI and compared the results to neural spiking patterns recorded in two monkeys performing an identical task. In **Chapter 4**, I then examine how somatosensory inputs from the fingers are integrated in S1. Sensory inputs from all fingers must be integrated during everyday hand use. However, previous work studying sensory integration across fingers have been restricted to studying how inputs from two fingers interact. Therefore, the full nature of finger interactions is unknown. To address this gap, I stimulate all possible single- and multi-finger combinations in humans and characterize the patterns of integration that occur in S1. Finally, in **Chapter 5**, I return to the motivating questions in my thesis and offer commentary and future directions.

1.6 References

- Abbasi, A., Estebanez, L., Goueytes, D., Lassagne, H., Shulz, D. E., & Ego-Stengel, V. (2020). Cortical closed-loop brain-machine interface requires biomimetic sensory feedback. *bioRxiv*.
- Andersen, P., Hagan, P. J., Phillips, C. G., & Powell, T. P. (1975). Mapping by microstimulation of overlapping projections from area 4 to motor units of the baboon's hand. *Proceedings of the Royal Society of London. Series B, Containing Papers of a Biological Character*, 188(1090), 31–36.
- Asanuma, H. (1975). Recent developments in the study of the columnar arrangement of neurons within the motor cortex. *Physiological Reviews*, 55(2), 143–156.
- Asanuma, H., Hongo, T., Jankowska, E., Marcus, S., Shinoda, Y., & Zarzecki, P. (1978). Pattern of projections of individual pyramidal tract neurons to the spinal cord of the monkey. *Journal of Physiology, Paris*, 74(3), 235–236.
- Asanuma, H., & Rosén, I. (1972). Topographical organization of cortical efferent zones projecting to distal forelimb muscles in the monkey. *Experimental Brain Research. Experimentelle Hirnforschung. Experimentation Cerebrale*, 14(3), 243–256.
- Asanuma, H., & Sakata, H. (1967). Functional Organization of a Cortical Efferent System Examined with Focal Depth Stimulation in Cats. *Journal of Neurophysiology*, 30(1), 35–54.
- Attwell, D., & Laughlin, S. B. (2001). An energy budget for signaling in the grey matter of the brain. *Journal of Cerebral Blood Flow and Metabolism: Official Journal of the International Society of Cerebral Blood Flow and Metabolism*, 21(10), 1133–1145.
- Attwell, D., & Iadecola, C. (2002). The neural basis of functional brain imaging signals. *Trends in Neurosciences*, 25(12), 621–625.
- Azim, E., & Seki, K. (2019). Gain control in the sensorimotor system. *Current Opinion in Physiology*, 8, 177–187.
- Bandettini, P. A., Wong, E. C., Hinks, R. S., Tikofsky, R. S., & Hyde, J. S. (1992). Time course EPI of human brain function during task activation. *Magnetic Resonance in Medicine: Official Journal of the Society of Magnetic Resonance in Medicine / Society of Magnetic Resonance in Medicine*, 25(2), 390–397.
- Bashir, S., Kaeser, M., Wyss, A., Hamadjida, A., Liu, Y., Bloch, J., ... Rouiller, E. M. (2012). Short-term effects of unilateral lesion of the primary motor cortex (M1) on ipsilesional hand dexterity in adult macaque monkeys. *Brain Structure & Function*, 217(1), 63–79.
- Beisteiner, R., Windischberger, C., Lanzenberger, R., Edward, V., Cunnington, R., Erdler, M., ... Deecke, L. (2001). Finger somatotopy in human motor cortex. *NeuroImage*, 13(6 Pt 1), 1016–1026.

- Bell, C. (1834). *The hand; its mechanism and vital endowments, as evincing design*. London: W. Pickering.
- Bensmaia, S. J., Denchev, P. V., Dammann, J. F., 3rd, Craig, J. C., & Hsiao, S. S. (2008). The representation of stimulus orientation in the early stages of somatosensory processing. *The Journal of Neuroscience: The Official Journal of the Society for Neuroscience*, 28(3), 776–786.
- Bernhard, C. G., & Bohm, E. (1954). Monosynaptic corticospinal activation of fore limb motoneurons in monkeys (*Macaca mulatta*). *Acta Physiologica Scandinavica*, 31(2–3), 104–112.
- Biermann, K., Schmitz, F., Witte, O. W., Konczak, J., Freund, H.-J., & Schnitzler, A. (1998). Interaction of finger representation in the human first somatosensory cortex: a neuromagnetic study. *Neuroscience Letters*, Vol. 251, pp. 13–16.
- Bodegård, A., Geyer, S., Grefkes, C., Zilles, K., & Roland, P. E. (2001). Hierarchical processing of tactile shape in the human brain. *Neuron*, 31(2), 317–328.
- Bortoff, G. A., & Strick, P. L. (1993). Corticospinal terminations in two new-world primates: further evidence that corticomotoneuronal connections provide part of the neural substrate for manual dexterity. *The Journal of Neuroscience: The Official Journal of the Society for Neuroscience*, 13(12), 5105–5118.
- Boynton, G. M., Engel, S. A., Glover, G. H., & Heeger, D. J. (1996). Linear Systems Analysis of Functional Magnetic Resonance Imaging in Human V1. *The Journal of Neuroscience: The Official Journal of the Society for Neuroscience*, 16(13), 4207–4221.
- Brochier, T., Boudreau, M. J., Paré, M., & Smith, A. M. (1999). The effects of muscimol inactivation of small regions of motor and somatosensory cortex on independent finger movements and force control in the precision grip. *Experimental Brain Research. Experimentelle Hirnforschung. Experimentation Cerebrale*, 128(1–2), 31–40.
- Brodmann, K. (1909). *Vergleichende Lokalisationslehre der Grosshirnrinde in ihren Prinzipien dargestellt auf Grund des Zellenbaues*. Barth.
- Brouwer, G. J., Arnedo, V., Offen, S., Heeger, D. J., & Grant, A. C. (2015). Normalization in human somatosensory cortex. *Journal of Neurophysiology*, 114(5), 2588–2599.
- Brumberg, J. C., Pinto, D. J., & Simons, D. J. (1996). Spatial gradients and inhibitory summation in the rat whisker barrel system. *Journal of Neurophysiology*, 76(1), 130–140.
- Burton, H., & Fabri, M. (1995). Ipsilateral intracortical connections of physiologically defined cutaneous representations in areas 3b and 1 of macaque monkeys: projections in the vicinity of the central sulcus. *The Journal of Comparative Neurology*, 355(4), 508–538.
- Buxton, R. B., Wong, E. C., & Frank, L. R. (1998). Dynamics of blood flow and oxygenation changes during brain activation: the balloon model. *Magnetic*

- Resonance in Medicine: Official Journal of the Society of Magnetic Resonance in Medicine / Society of Magnetic Resonance in Medicine, 39(6), 855–864.
- Buys, E. J., Lemon, R. N., Mantel, G. W., & Muir, R. B. (1986). Selective facilitation of different hand muscles by single corticospinal neurones in the conscious monkey. *The Journal of Physiology*, 381, 529–549.
- Carlson, M. (1981). Characteristics of sensory deficits following lesions of Brodmann's areas 1 and 2 in the postcentral gyrus of *Macaca mulatta*. *Brain Research*, 204(2), 424–430.
- Chang, H.-T., Ruch, T. C., & Ward, A. A. (1947). Topographical Representation Of Muscles In Motor Cortex Of Monkeys. *Journal of Neurophysiology*, 10(1), 39–56.
- Cheney, P. D., & Fetz, E. E. (1985). Comparable patterns of muscle facilitation evoked by individual corticomotoneuronal (CM) cells and by single intracortical microstimuli in primates: evidence for functional groups of CM cells. *Journal of Neurophysiology*, Vol. 53, pp. 786–804.
- Cisek, P. (2019). Resynthesizing behavior through phylogenetic refinement. *Attention, Perception & Psychophysics*, 81(7), 2265–2287.
- Clough, J. F., Kernell, D., & Phillips, C. G. (1968). The distribution of monosynaptic excitation from the pyramidal tract and from primary spindle afferents to motoneurons of the baboon's hand and forearm. *The Journal of Physiology*, 198(1), 145–166.
- Culham, J. C., & Valyear, K. F. (2006). Human parietal cortex in action. *Current Opinion in Neurobiology*, 16(2), 205–212.
- Darling, W. G., Morecraft, R. J., Rotella, D. L., Pizzimenti, M. A., Ge, J., Stilwell-Morecraft, K. S., ... Cheney, P. (2014). Recovery of precision grasping after motor cortex lesion does not require forced use of the impaired hand in *Macaca mulatta*. *Experimental Brain Research. Experimentelle Hirnforschung. Experimentation Cerebrale*, 232(12), 3929–3938.
- deCharms, R. C., & Zador, A. (2000). Neural representation and the cortical code. *Annual Review of Neuroscience*, 23, 613–647.
- Dechent, P., & Frahm, J. (2003). Functional somatotopy of finger representations in human primary motor cortex. *Human Brain Mapping*, 18(4), 272–283.
- DeFelipe, J., Hendry, S. H., Jones, E. G., & Schmechel, D. (1985). Variability in the terminations of GABAergic chandelier cell axons on initial segments of pyramidal cell axons in the monkey sensory-motor cortex. *The Journal of Comparative Neurology*, 231(3), 364–384.
- Diedrichsen, J., & Kriegeskorte, N. (2017). Representational models: A common framework for understanding encoding, pattern-component, and representational-similarity analysis. *PLoS Computational Biology*, 13(4), e1005508.

- Dum, R. P., & Strick, P. L. (1991). The origin of corticospinal projections from the premotor areas in the frontal lobe. *The Journal of Neuroscience: The Official Journal of the Society for Neuroscience*, 11(3), 667–689.
- Ejaz, N., Hamada, M., & Diedrichsen, J. (2015). Hand use predicts the structure of representations in sensorimotor cortex. *Nature Neuroscience*, 18(7), 1034–1040.
- Ejaz, N., Xu, J., Branscheidt, M., Hertler, B., Schambra, H., Widmer, M., ... Diedrichsen, J. (2018). Evidence for a subcortical origin of mirror movements after stroke: a longitudinal study. *Brain: A Journal of Neurology*, 141(3), 837–847.
- Ferrier, D. (1875). Experiments on the brain of monkeys.— No. I. *Proceedings of the Royal Society of London*, 23(156–163), 409–430.
- Fetz, E. E., & Cheney, P. D. (1980). Postspike facilitation of forelimb muscle activity by primate corticomotoneuronal cells. *Journal of Neurophysiology*, Vol. 44, pp. 751–772.
- Fetz, E. E., Cheney, P. D., & German, D. C. (1976). Corticomotoneuronal connections of precentral cells detected by post-spike averages of EMG activity in behaving monkeys. *Brain Research*, Vol. 114, pp. 505–510.
- Flesher, S. N., Downey, J. E., Weiss, J. M., Hughes, C. L., Herrera, A. J., Tyler-Kabara, E. C., ... Gaunt, R. A. (2021). A brain-computer interface that evokes tactile sensations improves robotic arm control. *Science*, 372(6544), 831–836.
- Florence, S. L., Wall, J. T., & Kaas, J. H. (1988). The somatotopic pattern of afferent projections from the digits to the spinal cord and cuneate nucleus in macaque monkeys. *Brain Research*, 452(1–2), 388–392.
- Florence, S. L., Wall, J. T., & Kaas, J. H. (1989). Somatotopic organization of inputs from the hand to the spinal gray and cuneate nucleus of monkeys with observations on the cuneate nucleus of humans. *The Journal of Comparative Neurology*, 286(1), 48–70.
- Foerster, O. (1936). The Motor Cortex In Man In The Light Of Hughlings Jackson's Doctrines. *Brain: A Journal of Neurology*, 59(2), 135–159.
- Friedman, R. M., Chen, L. M., & Roe, A. W. (2008). Responses of areas 3b and 1 in anesthetized squirrel monkeys to single- and dual-site stimulation of the digits. *Journal of Neurophysiology*, 100(6), 3185–3196.
- Friel, K. M., Barbay, S., Frost, S. B., Plautz, E. J., Hutchinson, D. M., Stowe, A. M., ... Nudo, R. J. (2005). Dissociation of sensorimotor deficits after rostral versus caudal lesions in the primary motor cortex hand representation. *Journal of Neurophysiology*, 94(2), 1312–1324.
- Fritsch, G., & Hitzig, E. (1870). Electric excitability of the cerebrum (Über die elektrische Erregbarkeit des Grosshirns). *Arch Anat Physiol Wissen*, 37, 300–332.
- Gallivan, J. P., McLean, D. A., Valyear, K. F., Pettepiece, C. E., & Culham, J. C. (2011). Decoding action intentions from preparatory brain activity in human parieto-frontal networks. *The Journal of Neuroscience: The Official Journal of the Society for Neuroscience*, 31(26), 9599–9610.

- Gandevia, S. C., Burke, D., & McKeon, B. B. (1983). Convergence in the somatosensory pathway between cutaneous afferents from the index and middle fingers in man. *Experimental Brain Research. Experimentelle Hirnforschung. Experimentation Cerebrale*, 50(2–3), 415–425.
- Gentner, R., & Classen, J. (2006). Modular organization of finger movements by the human central nervous system. *Neuron*, 52(4), 731–742.
- Gentner, R., Gorges, S., Weise, D., aufm Kampe, K., Buttmann, M., & Classen, J. (2010). Encoding of motor skill in the corticomuscular system of musicians. *Current Biology: CB*, 20(20), 1869–1874.
- Graziano, M. S. A., & Aflalo, T. N. (2007). Mapping behavioral repertoire onto the cortex. *Neuron*, 56(2), 239–251.
- Graziano, M. S. A., Taylor, C. S. R., & Moore, T. (2002). Complex Movements Evoked by Microstimulation of Precentral Cortex. *Neuron*, 34(5), 841–851.
- Harel, N., Lin, J., Moeller, S., Ugurbil, K., & Yacoub, E. (2006). Combined imaging-histological study of cortical laminar specificity of fMRI signals. *NeuroImage*, 29(3), 879–887.
- Harris, J. J., Jolivet, R., & Attwell, D. (2012). Synaptic Energy Use and Supply. *Neuron*, 75(5), 762–777.
- Haxby, J. V., Gobbini, M. I., Furey, M. L., Ishai, A., Schouten, J. L., & Pietrini, P. (2001). Distributed and overlapping representations of faces and objects in ventral temporal cortex. *Science*, 293(5539), 2425–2430.
- Haxby, James V., Connolly, A. C., & Guntupalli, J. S. (2014). Decoding Neural Representational Spaces Using Multivariate Pattern Analysis. *Annual Review of Neuroscience*, 37(1), 435–456.
- Heffner, R. S., & Masterton, R. B. (1983). The role of the corticospinal tract in the evolution of human digital dexterity. *Brain, Behavior and Evolution*, 23(3–4), 165–183.
- Hendry, S. H., Schwark, H. D., Jones, E. G., & Yan, J. (1987). Numbers and proportions of GABA-immunoreactive neurons in different areas of monkey cerebral cortex. *The Journal of Neuroscience: The Official Journal of the Society for Neuroscience*, 7(5), 1503–1519.
- Hikosaka, O., Tanaka, M., Sakamoto, M., & Iwamura, Y. (1985). Deficits in manipulative behaviors induced by local injections of muscimol in the first somatosensory cortex of the conscious monkey. *Brain Research*, 325(1–2), 375–380.
- Hlustík, P., Solodkin, A., Gullapalli, R. P., Noll, D. C., & Small, S. L. (2001). Somatotopy in human primary motor and somatosensory hand representations revisited. *Cerebral Cortex*, 11(4), 312–321.
- Hochstetter, K., Rupp, A., Stančák, A., Meinck, H.-M., Stippich, C., Berg, P., & Scherg, M. (2001). Interaction of Tactile Input in the Human Primary and Secondary

- Somatosensory Cortex—A Magnetoencephalographic Study. *NeuroImage*, 14(3), 759–767.
- Hsiao, S., & Yau, J. (2008). Neural basis of haptic perception. In M. Grunwald (Ed.), *Human Haptic Perception: Basics and Applications* (pp. 103–112). Basel: Birkhäuser Basel.
- Hsieh, C.-L., Shima, F., Tobimatsu, S., Sun, S.-J., & Kato, M. (1995). The interaction of the somatosensory evoked potentials to simultaneous finger stimuli in the human central nervous system. A study using direct recordings. *Electroencephalography and Clinical Neurophysiology/Evoked Potentials Section*, Vol. 96, pp. 135–142. doi:10.1016/0168-5597(94)00251-9
- Hughlings, J. (1870). A study of convulsions. *Transactions of the Saint Andrews Medical Graduates Association*, 3, 162–204.
- Hyvärinen, J., & Poranen, A. (1978). Receptive field integration and submodality convergence in the hand area of the post-central gyrus of the alert monkey. *The Journal of Physiology*, Vol. 283, pp. 539–556.
- Indovina, I., & Sanes, J. N. (2001). On somatotopic representation centers for finger movements in human primary motor cortex and supplementary motor area. *NeuroImage*, 13(6 Pt 1), 1027–1034.
- Ishibashi, H., Tobimatsu, S., Shigeto, H., Morioka, T., Yamamoto, T., & Fukui, M. (2000). Differential interaction of somatosensory inputs in the human primary sensory cortex: a magnetoencephalographic study. *Clinical Neurophysiology: Official Journal of the International Federation of Clinical Neurophysiology*, 111(6), 1095–1102.
- Iwamura, Y. (1998). Hierarchical somatosensory processing. *Current Opinion in Neurobiology*, 8(4), 522–528.
- Iwamura, Y., & Tanaka, M. (1978). Postcentral neurons in hand region of area 2: their possible role in the form discrimination of tactile objects. *Brain Research*, 150(3), 662–666.
- Iwamura, Y., Tanaka, M., Sakamoto, M., & Hikosaka, O. (1993). Rostrocaudal gradients in the neuronal receptive field complexity in the finger region of the alert monkey's postcentral gyrus. *Experimental Brain Research. Experimentelle Hirnforschung. Experimentation Cerebrale*, 92(3), 360–368.
- Jacob, F. (1977). Evolution and tinkering. *Science*, 196(4295), 1161–1166.
- Jankowska, E., Padel, Y., & Tanaka, R. (1975). Projections of pyramidal tract cells to alpha-motoneurons innervating hind-limb muscles in the monkey. *The Journal of Physiology*, 249(3), 637–667.
- Johansson, R. S., & Flanagan, J. R. (2009). Coding and use of tactile signals from the fingertips in object manipulation tasks. *Nature Reviews. Neuroscience*, 10(5), 345–359.
- Johansson, R. S., & Vallbo, Å. B. (1983). Tactile sensory coding in the glabrous skin of the human hand. *Trends in Neurosciences*, 6, 27–32.

- Johnson-Frey, S. H. (2004). The neural bases of complex tool use in humans. *Trends in Cognitive Sciences*, 8(2), 71–78.
- Jones, E. G. (1975). Lamination and differential distribution of thalamic afferents within the sensory-motor cortex of the squirrel monkey. *The Journal of Comparative Neurology*, 160(2), 167–203.
- Jones, E. G., & Powell, T. P. (1970). Connexions of the somatic sensory cortex of the rhesus monkey. 3. Thalamic connexions. *Brain: A Journal of Neurology*, 93(1), 37–56.
- Jörntell, H., Bengtsson, F., Geborek, P., Spanne, A., Terekhov, A. V., & Hayward, V. (2014). Segregation of tactile input features in neurons of the cuneate nucleus. *Neuron*, 83(6), 1444–1452.
- Kakei, S., Hoffman, D. S., & Strick, P. L. (1999). Muscle and movement representations in the primary motor cortex. *Science*, 285(5436), 2136–2139.
- Kinoshita, M., Matsui, R., Kato, S., Hasegawa, T., Kasahara, H., Isa, K., ... Isa, T. (2012). Genetic dissection of the circuit for hand dexterity in primates. *Nature*, 487(7406), 235–238.
- Kriegeskorte, N., & Diedrichsen, J. (2016). Inferring brain-computational mechanisms with models of activity measurements. *Philosophical Transactions of the Royal Society of London. Series B, Biological Sciences*, 371(1705). doi:10.1098/rstb.2016.0278
- Kriegeskorte, N., & Diedrichsen, J. (2019). Peeling the Onion of Brain Representations. *Annual Review of Neuroscience*, 42(1), 407–432.
- Kriegeskorte, N., & Douglas, P. K. (2019). Interpreting encoding and decoding models. *Current Opinion in Neurobiology*, 55, 167–179.
- Kriegeskorte, N., Mur, M., & Bandettini, P. (2008). Representational similarity analysis - connecting the branches of systems neuroscience. *Frontiers in Systems Neuroscience*, 2, 4.
- Kwong, K. K., Belliveau, J. W., Chesler, D. A., Goldberg, I. E., Weisskoff, R. M., Poncelet, B. P., ... Turner, R. (1992). Dynamic magnetic resonance imaging of human brain activity during primary sensory stimulation. *Proceedings of the National Academy of Sciences of the United States of America*, 89(12), 5675–5679.
- Laboy-Juárez, K. J., Langberg, T., Ahn, S., & Feldman, D. E. (2019). Elementary motion sequence detectors in whisker somatosensory cortex. *Nature Neuroscience*, 22(9), 1438–1449.
- Landgren, S., Phillips, C. G., & Porter, R. (1962). Cortical fields of origin of the monosynaptic pyramidal pathways to some alpha motoneurons of the baboon's hand and forearm. *The Journal of Physiology*, 161, 112–125.
- Lang, C. E., & Schieber, M. H. (2004). Reduced muscle selectivity during individuated finger movements in humans after damage to the motor cortex or corticospinal tract. *Journal of Neurophysiology*, 91(4), 1722–1733.

- Lawrence, D. G., & Hopkins, D. A. (1976). The development of motor control in the rhesus monkey: evidence concerning the role of corticomotoneuronal connections. *Brain: A Journal of Neurology*, 99(2), 235–254.
- Lawrence, D. G., & Kuypers, H. G. (1968). The functional organization of the motor system in the monkey. II. The effects of lesions of the descending brain-stem pathways. *Brain: A Journal of Neurology*, 91(1), 15–36.
- Lemon, R. N. (2008). Descending pathways in motor control. *Annual Review of Neuroscience*, 31, 195–218.
- Lipton, M. L., Liszewski, M. C., Noelle O’Connell, M., Mills, A., Smiley, J. F., Branch, C. A., ... Schroeder, C. E. (2010). Interactions within the Hand Representation in Primary Somatosensory Cortex of Primates. *The Journal of Neuroscience: The Official Journal of the Society for Neuroscience*, 30(47), 15895–15903.
- Liu, Y., & Rouiller, E. M. (1999). Mechanisms of recovery of dexterity following unilateral lesion of the sensorimotor cortex in adult monkeys. *Experimental Brain Research. Experimentelle Hirnforschung. Experimentation Cerebrale*, 128(1–2), 149–159.
- Logothetis, N. K., Pauls, J., Augath, M., Trinath, T., & Oeltermann, A. (2001). Neurophysiological investigation of the basis of the fMRI signal. *Nature*, 412(6843), 150–157.
- Logothetis, Nikos K. (2003). The Underpinnings of the BOLD Functional Magnetic Resonance Imaging Signal. *The Journal of Neuroscience: The Official Journal of the Society for Neuroscience*, 23(10), 3963–3971.
- Lyall, E. H., Mossing, D. P., Pluta, S. R., Dudai, A., & Adesnik, H. (2020). Synthesis of higher order feature codes through stimulus-specific supra-linear summation. *bioRxiv*
- Markram, H., Toledo-Rodriguez, M., Wang, Y., Gupta, A., Silberberg, G., & Wu, C. (2004). Interneurons of the neocortical inhibitory system. *Nature Reviews. Neuroscience*, 5(10), 793–807.
- Mata, M., Fink, D. J., Gainer, H., Smith, C. B., Davidsen, L., Savaki, H., ... Sokoloff, L. (1980). Activity-dependent energy metabolism in rat posterior pituitary primarily reflects sodium pump activity. *Journal of Neurochemistry*, 34(1), 213–215.
- Matsumura, M., Sawaguchi, T., Oishi, T., Ueki, K., & Kubota, K. (1991). Behavioral deficits induced by local injection of bicuculline and muscimol into the primate motor and premotor cortex. *Journal of Neurophysiology*, 65(6), 1542–1553.
- McKiernan, B. J., Marcario, J. K., Karrer, J. H., & Cheney, P. D. (1998). Corticomotoneuronal postspike effects in shoulder, elbow, wrist, digit, and intrinsic hand muscles during a reach and prehension task. *Journal of Neurophysiology*, 80(4), 1961–1980.
- Miles, R., Tóth, K., Gulyás, A. I., Hájos, N., & Freund, T. F. (1996). Differences between somatic and dendritic inhibition in the hippocampus. *Neuron*, 16(4), 815–823.

- Mirabella, G., Battiston, S., & Diamond, M. E. (2001). Integration of multiple-whisker inputs in rat somatosensory cortex. *Cerebral Cortex*, 11(2), 164–170.
- Morecraft, R. J., Ge, J., Stilwell-Morecraft, K. S., McNeal, D. W., Pizzimenti, M. A., & Darling, W. G. (2013). Terminal distribution of the corticospinal projection from the hand/arm region of the primary motor cortex to the cervical enlargement in rhesus monkey. *The Journal of Comparative Neurology*, 521(18), 4205–4235.
- Murata, Y., Higo, N., Oishi, T., Yamashita, A., Matsuda, K., Hayashi, M., & Yamane, S. (2008). Effects of motor training on the recovery of manual dexterity after primary motor cortex lesion in macaque monkeys. *Journal of Neurophysiology*, 99(2), 773–786.
- Nudo, R. J., Jenkins, W. M., Merzenich, M. M., Prejean, T., & Grenda, R. (1992). Neurophysiological correlates of hand preference in primary motor cortex of adult squirrel monkeys. *The Journal of Neuroscience: The Official Journal of the Society for Neuroscience*, 12(8), 2918–2947.
- Ogawa, S., Lee, T. M., Kay, A. R., & Tank, D. W. (1990). Brain magnetic resonance imaging with contrast dependent on blood oxygenation. *Proceedings of the National Academy of Sciences of the United States of America*, 87(24), 9868–9872.
- Ogawa, S., Lee, T. M., Nayak, A. S., & Glynn, P. (1990). Oxygenation-sensitive contrast in magnetic resonance image of rodent brain at high magnetic fields. *Magnetic Resonance in Medicine: Official Journal of the Society of Magnetic Resonance in Medicine / Society of Magnetic Resonance in Medicine*, 14(1), 68–78.
- Ogawa, S., Tank, D. W., Menon, R., Ellermann, J. M., Kim, S. G., Merkle, H., & Ugurbil, K. (1992). Intrinsic signal changes accompanying sensory stimulation: functional brain mapping with magnetic resonance imaging. *Proceedings of the National Academy of Sciences of the United States of America*, 89(13), 5951–5955.
- O'Herron, P., Chhatbar, P. Y., Levy, M., Shen, Z., Schramm, A. E., Lu, Z., & Kara, P. (2016). Neural correlates of single-vessel haemodynamic responses in vivo. *Nature*, 534(7607), 378–382.
- Passingham, R. E., Perry, V. H., & Wilkinson, F. (1983). The long-term effects of removal of sensorimotor cortex in infant and adult rhesus monkeys. *Brain: A Journal of Neurology*, 106 (Pt 3), 675–705.
- Pauling, L., & Coryell, C. D. (1936). The Magnetic Properties and Structure of Hemoglobin, Oxyhemoglobin and Carbonmonoxyhemoglobin. *Proceedings of the National Academy of Sciences of the United States of America*, 22(4), 210–216.
- Penfield, W., & Boldrey, E. (1937). Somatic motor and sensory representation in the cerebral cortex of man as studied by electrical stimulation. *Brain: A Journal of Neurology*, 60(4), 389–443.
- Penfield, W. G. (1947). Ferrier Lecture - Some observations on the cerebral cortex of man. *Proceedings of the Royal Society of London. Series B - Biological Sciences*, 134(876), 329–347.

- Penfield, W., & Rasmussen, T. (1950). The cerebral cortex of man; a clinical study of localization of function. 248. Retrieved from <https://psycnet.apa.org/fulltext/1951-01483-000.pdf>
- Phillips, C. G. (1973). Hughlings Jackson Lecture. Cortical Localization and “sensori Motor Processes” at the “middle Level” in Primates. *Proceedings of the Royal Society of Medicine*, 66(10), 987–1002.
- Phillips, C. G. (1975). Laying the Ghost of ‘Muscles Versus Movements.’ *The Canadian Journal of Neurological Sciences. Le Journal Canadien Des Sciences Neurologiques*, 2(3), 209–218.
- Phillips, C. G., & Porter, R. (1964). The Pyramidal Projection To Motoneurons Of Some Muscle Groups Of The Baboon’s Forelimb. *Progress in Brain Research*, 12, 222–245.
- Powell, T. P., & Mountcastle, V. B. (1959). The cytoarchitecture of the postcentral gyrus of the monkey *Macaca mulatta*. *Bulletin of the Johns Hopkins Hospital*, 105, 108–131.
- Rathelot, J.-A., Dum, R. P., & Strick, P. L. (2017). Posterior parietal cortex contains a command apparatus for hand movements. *Proceedings of the National Academy of Sciences of the United States of America*, 114(16), 4255–4260.
- Rathelot, J.-A., & Strick, P. L. (2006). Muscle representation in the macaque motor cortex: an anatomical perspective. *Proceedings of the National Academy of Sciences of the United States of America*, 103(21), 8257–8262.
- Rathelot, J.-A., & Strick, P. L. (2009). Subdivisions of primary motor cortex based on cortico-motoneuronal cells. *Proceedings of the National Academy of Sciences of the United States of America*, 106(3), 918–923.
- Reed, J. L., Pouget, P., Qi, H.-X., Zhou, Z., Bernard, M. R., Burish, M. J., ... Kaas, J. H. (2008). Widespread spatial integration in primary somatosensory cortex. *Proceedings of the National Academy of Sciences of the United States of America*, 105(29), 10233–10237.
- Reed, J. L., Qi, H.-X., Zhou, Z., Bernard, M. R., Burish, M. J., Bonds, A. B., & Kaas, J. H. (2010). Response properties of neurons in primary somatosensory cortex of owl monkeys reflect widespread spatiotemporal integration. *Journal of Neurophysiology*, 103(4), 2139–2157.
- Rouiller, E. M., Yu, X. H., Moret, V., Tempini, A., Wiesendanger, M., & Liang, F. (1998). Dexterity in adult monkeys following early lesion of the motor cortical hand area: the role of cortex adjacent to the lesion. *The European Journal of Neuroscience*, 10(2), 729–740.
- Ruben, J., Krause, T., Taskin, B., Blankenburg, F., Moosmann, M., & Villringer, A. (2006). Sub-area-specific Suppressive Interaction in the BOLD responses to simultaneous finger stimulation in human primary somatosensory cortex: evidence for increasing rostral-to-caudal convergence. *Cerebral Cortex*, 16(6), 819–826.

- Russell, J. R., & DeMyer, W. (1961). The quantitative cortical origin of pyramidal axons of *Macaca rhesus*: With some remarks on the slow rate of axolysis. *Neurology*, 11(2), 96–96.
- Sanes, J. N., Donoghue, J. P., Thangaraj, V., Edelman, R. R., & Warach, S. (1995). Shared neural substrates controlling hand movements in human motor cortex. *Science*, 268(5218), 1775–1777.
- Sasaki, S., Isa, T., Pettersson, L.-G., Alstermark, B., Naito, K., Yoshimura, K., ... Ohki, Y. (2004). Dexterous finger movements in primate without monosynaptic corticomotoneuronal excitation. *Journal of Neurophysiology*, 92(5), 3142–3147.
- Schieber, M. H., & Hibbard, L. S. (1993). How somatotopic is the motor cortex hand area? *Science*, 261(5120), 489–492.
- Schieber, M. H., & Poliakov, A. V. (1998). Partial inactivation of the primary motor cortex hand area: effects on individuated finger movements. *The Journal of Neuroscience: The Official Journal of the Society for Neuroscience*, 18(21), 9038–9054.
- Schieber, M. H. (2002). Motor cortex and the distributed anatomy of finger movements. *Advances in Experimental Medicine and Biology*, 508, 411–416.
- Schwartz, W. J., Smith, C. B., Davidsen, L., Savaki, H., Sokoloff, L., Mata, M., ... Gainer, H. (1979). Metabolic mapping of functional activity in the hypothalamo-neurohypophysial system of the rat. *Science*, 205(4407), 723–725.
- Shanks, M. F., & Powell, T. P. (1981). An electron microscopic study of the termination of thalamocortical fibres in areas 3b, 1 and 2 of the somatic sensory cortex in the monkey. *Brain Research*, 218(1–2), 35–47.
- Shinoda, Y., Yokota, J., & Futami, T. (1981). Divergent projection of individual corticospinal axons to motoneurons of multiple muscles in the monkey. *Neuroscience Letters*, 23(1), 7–12.
- Siero, J. C., Hermes, D., Hoogduin, H., Luijten, P. R., Petridou, N., & Ramsey, N. F. (2013). BOLD consistently matches electrophysiology in human sensorimotor cortex at increasing movement rates: a combined 7T fMRI and ECoG study on neurovascular coupling. *Journal of Cerebral Blood Flow & Metabolism*, 33(10), 1448–1456.
- Simons, D. J. (1985). Temporal and spatial integration in the rat SI vibrissa cortex. *Journal of Neurophysiology*, 54(3), 615–635.
- Stoney, S. D., Jr, Thompson, W. D., & Asanuma, H. (1968). Excitation of pyramidal tract cells by intracortical microstimulation: effective extent of stimulating current. *Journal of Neurophysiology*, 31(5), 659–669.
- Strick, P. L., & Preston, J. B. (1982). Two representations of the hand in area 4 of a primate. I. Motor output organization. *Journal of Neurophysiology*, 48(1), 139–149.
- Suminski, A. J., Tkach, D. C., Fagg, A. H., & Hatsopoulos, N. G. (2010). Incorporating Feedback from Multiple Sensory Modalities Enhances Brain–Machine Interface

- Control. *The Journal of Neuroscience: The Official Journal of the Society for Neuroscience*, 30(50), 16777–16787.
- Sur, M., Merzenich, M. M., & Kaas, J. H. (1980). Magnification, receptive-field area, and “hypercolumn” size in areas 3b and 1 of somatosensory cortex in owl monkeys. *Journal of Neurophysiology*, Vol. 44, pp. 295–311.
- Takei, T., & Seki, K. (2010). Spinal interneurons facilitate coactivation of hand muscles during a precision grip task in monkeys. *The Journal of Neuroscience: The Official Journal of the Society for Neuroscience*, 30(50), 17041–17050.
- Taylor, C. S. R., & Gross, C. G. (2003). Twitches versus movements: a story of motor cortex. *The Neuroscientist: A Review Journal Bringing Neurobiology, Neurology and Psychiatry*, 9(5), 332–342.
- Thakur, P. H., Fitzgerald, P. J., & Hsiao, S. S. (2012). Second-order receptive fields reveal multidigit interactions in area 3b of the macaque monkey. *Journal of Neurophysiology*, 108(1), 243–262.
- Tower, S. S. (1940). Pyramidal Lesion In The Monkey. *Brain: A Journal of Neurology*, 63(1), 36–90.
- Walther, A., Nili, H., Ejaz, N., Alink, A., Kriegeskorte, N., & Diedrichsen, J. (2016). Reliability of dissimilarity measures for multi-voxel pattern analysis. *NeuroImage*, 137, 188–200
- Woolsey, T. A., & Van der Loos, H. (1970). The structural organization of layer IV in the somatosensory region (SI) of mouse cerebral cortex. The description of a cortical field composed of discrete cytoarchitectonic units. *Brain Research*, 17(2), 205–242.
- Yau, J. M., Connor, C. E., & Hsiao, S. S. (2013). Representation of tactile curvature in macaque somatosensory area 2. *Journal of Neurophysiology*, 109(12), 2999–3012.
- Yau, J. M., Kim, S. S., Thakur, P. H., & Bensmaia, S. J. (2016). Feeling form: the neural basis of haptic shape perception. *Journal of Neurophysiology*, 115(2), 631–642.
- Zhang, N., Yacoub, E., Zhu, X.-H., Ugurbil, K., & Chen, W. (2009). Linearity of blood-oxygenation-level dependent signal at microvasculature. *NeuroImage*, 48(2), 313–318.
- Zhang, N., Zhu, X.-H., & Chen, W. (2008). Investigating the source of BOLD nonlinearity in human visual cortex in response to paired visual stimuli. *NeuroImage*, 43(2), 204–212.

Chapter 2

2 Stability of representational geometry across a wide range of fMRI activity levels

In this first project, I examined the stability of multivariate representational analysis of fMRI data. The degree to which brain representations measured with fMRI are stable has important implications for the kinds of inferences one can make with this analysis framework, and has direct implications for the rest of the work presented in my thesis.

2.1 Abstract

Fine-grained activity patterns, as measured with functional magnetic resonance imaging (fMRI), are thought to reflect underlying neural representations. Multivariate analysis techniques, such as representational similarity analysis (RSA), can be used to test models of brain representation by quantifying the representational geometry (the collection of pair-wise dissimilarities between activity patterns). One important caveat, however, is that nonlinearities in the coupling between neural activity and the fMRI signal may lead to significant distortions in the representational geometry estimated from fMRI activity patterns. Here we tested the stability of representational dissimilarity measures in primary sensory-motor (S1 and M1) and early visual regions (V1/V2) across a large range of activation levels. Participants were visually cued with different letters to perform single finger presses with one of the 5 fingers at a rate of 0.3–2.6 Hz. For each stimulation frequency, we quantified the difference between the 5 activity patterns in M1, S1, and V1/V2. We found that the representational geometry remained relatively stable, even though the average activity increased over a large dynamic range. These results indicate that the representational geometry of fMRI activity patterns can be reliably assessed, largely independent of the average activity in the region. This has important methodological implications for RSA and other multivariate analysis approaches that use the representational geometry to make inferences about brain representations.

2.2 Introduction

Multivariate analysis of activity patterns has profoundly changed functional magnetic resonance imaging (fMRI) data analysis. Traditional fMRI studies have examined differences in overall activity levels in extended brain regions. In this approach, local fine-grained patterns of activity are removed by smoothing, as they are typically not consistent across individuals. However, it was realized that one could decode the experimental condition from activity patterns within individuals, even if the average activity is the same between conditions (Haxby et al., 2001). Decodability is often interpreted as evidence that the region represents something about the underlying distinction between conditions (Haxby et al., 2014), i.e., that another area can potentially read out information about the distinction (de-Wit et al., 2016; deCharms and Zador, 2000). Extending this idea, the degree to which different pairs of activity patterns are dissimilar may tell us something about the structure of the underlying neural population code. For example, a region involved in object recognition should show large dissimilarities between activity patterns associated with objects from different categories, but smaller dissimilarities between objects of the same category (Kriegeskorte et al., 2008b). The relationship between all pair-wise dissimilarities defines what we call the representational geometry. Representational similarity analysis (RSA, Kriegeskorte et al., 2008a), pattern component modelling (PCM, Diedrichsen et al., 2018) and encoding models (Naselaris et al., 2011) all analyse this representational geometry to test between models of brain representations (Diedrichsen and Kriegeskorte, 2017).

When testing representational models with fMRI data, we base our analysis on the Blood Oxygenation Level Dependent (BOLD) signal. To what degree can we make inferences about neural representations using this indirect measure of neural activity? There are a number of reasons why representational fMRI analysis may be limited (see discussion). One important problem, which is the main focus of this paper, is that the measured representational geometry may depend strongly on the overall activity in a region. This is of concern as we often make comparisons across regions, participants, or attentional states with different activity levels. Although RSA is in theory independent of average activity, it is possible that the patterns and their dissimilarities distort with increasing

activation. The relationship between the pair-wise pattern dissimilarities is only guaranteed to remain the same if all voxel activities in a region scale (up to a multiplicative constant) according to the same function. Thus, even though there is evidence that the relationship between neural activity and the average BOLD is fairly linear in M1 (Siero et al., 2013) and V1 (Boynton et al., 1996; Heeger et al., 2000), these findings do not guarantee that the representational geometry would also scale in an orderly fashion.

There are a number of potential mechanisms that could lead to substantial distortions of the representational geometry when measured with fMRI. For example, the spatial point-spread function of BOLD may differ across activity levels. Recent work using optical imaging suggests that although vasodilation of arterioles is relatively coupled with the pre- and post-synaptic activity of the surrounding neural tissues (O'Herron et al., 2016), the authors observed many instances of vasodilatory responses in the absence of local changes in neural activity. Notably, they propose that this decoupling may change with increasing neural activity. We interpret this result as cause for concern, as this effect could cause an increasing spread of the BOLD signal to neighboring voxels as activity increases. Because such spread would affect different activity patterns differently, it could lead to severe distortions of the representational geometry, which would make it difficult to draw conclusions about the representational content of neural population codes using fMRI data. Therefore, it is important to empirically test if the representational geometry remains stable across a wide range of overall activity levels.

We investigated this question with an experiment that allowed us to assess patterns in sensory-motor regions (S1 and M1) and in primary and secondary visual cortices (V1 and V2) using RSA. Ejaz et al. (2015) demonstrated a stable representational geometry across humans for individual finger movements in M1 and S1, in which the thumb had the most distinct activity pattern and neighboring fingers showed higher similarities than non-neighboring fingers. Similarly, it has been shown that letters (Miyawaki et al., 2008) as well as colours (Brouwer and Heeger, 2009), can be decoded from activity in visual cortices. We therefore cued finger presses with coloured letter cues presented on a screen. We chose a specific letter and colour for each finger, such that the perceptual similarities

between stimuli would be different from the dissimilarities of motor actions. To increase the overall activity in both regions, we varied the letter flashing and finger pressing frequency between 0.3 Hz and 2.6 Hz. For individual finger presses on our isometric device (see methods), a rate of 2.6 Hz is close to the upper performance limit.

In interpreting the results, it is important to distinguish between changes in the representational geometry that arise from the fact that the neural activity patterns change qualitatively with higher stimulation frequency, and changes that arise through distortions when measuring the representational geometry using BOLD. We designed our task assuming that the underlying neural activity patterns would scale by a single multiplicative factor with increasing speed, allowing us to identify distortions arising in the neural-to-BOLD coupling.

We note that the data have been already included in a recent publication from our lab (Diedrichsen et al., 2018) as an example to highlight the technical aspects of fitting different types of PCM models. Although not the focus of the paper, the results already indicate that, on a group level, the representational geometry in M1 remains relatively unchanged across movement speeds. However, because possible distortion may be idiosyncratic across individuals, we here re-investigate this issue with dedicated analyses within the framework of RSA.

2.3 Methods

2.3.1 Participants

We measured cortical activity patterns in 5 female and 3 male participants (mean Age = 25.5 (2.41) years). All participants were self-reported right handers (mean Edinburgh questionnaire laterality quotient = 91.25 (7.82)), and made individuated finger presses of the right hand. Motor cortex data from these participants were used as example data in a method article describing non-linear pattern component models (Diedrichsen et al., 2018).

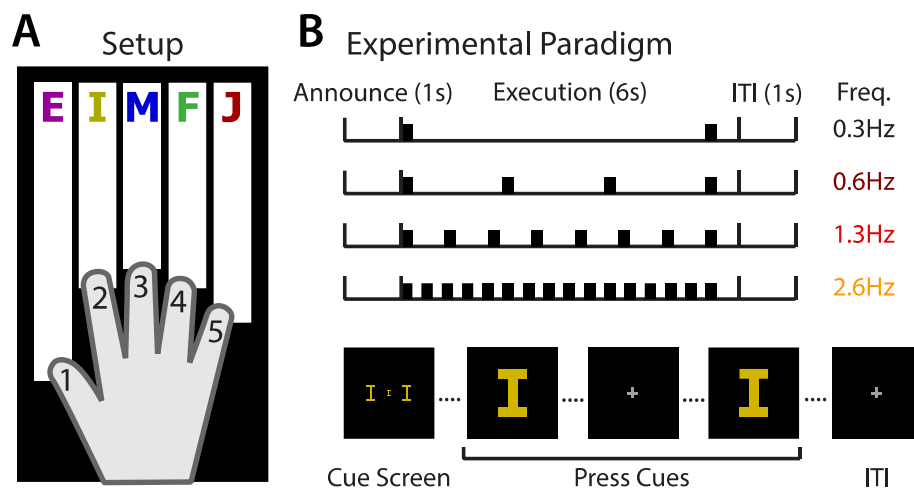


Figure 2.1: Experimental paradigm

(a) Participants made short, isometric presses of an individual finger onto a keyboard while in an MR scanner. Each finger press was cued with a unique colour-letter combination.

(b) A cue at the start of each trial (1s) instructed participants which finger they would press. Participants then executed presses when prompted by a larger cue presentation. The cues flashed either 2, 4, 8, or 16 presses in 6 seconds (0.3, 0.6, 1.3, 2.6Hz). A 1s inter-trial-interval (ITI) separated each trial. Random periods of rest were interleaved between trials in each block. This design yielded 20 conditions (5 fingers /letters x 4 frequencies).

2.3.2 Apparatus and stimuli

The motor behaviour was monitored by a keyboard-like device. The device had a key for each finger of the right hand, with a force transducer (Honeywell-FS series, dynamic range=0–16N, resolution <0.02N) mounted under each key. A bevel on each key ensured fingertip placement across participants was consistent. Forces were recorded at a sampling rate of 200 Hz.

To evoke visual responses, we presented coloured letter stimuli on the screen at the same frequency as the finger presses. The aim was to pick letters and colours that would induce a dissimilarity structure that would differ considerably from that of the fingers. Therefore, we chose similar letters and colours for fingers which evoke different activity profiles (see Fig. 2.1A for finger-letter-colour pairs). The letters were presented centrally and peripherally (Fig. 2.1B). The size of the letters on the screen were 8x10 cm, subtending a visual angle of approximately 7°. The screen background was black. Participants were instructed to maintain visual fixation on a gray cross presented centrally on the screen. Cues were presented centered on the fixation cue. Five lines were presented in the lower third of the screen, one for each of the five fingers. The locations of these lines were dynamically updated to indicate the real-time force applied to each key of the fingerboard device.

2.3.3 Behavioural task

In the MR scanner, participants completed a paced finger pressing task. Each trial lasted for 8 s and was divided into three phases (Fig. 2.1B). In the announce phase (1s), participants saw a visual cue indicating which finger of their right hand they were to press in the current trial. During the following execution phase (6s), participants made 2, 4, 8, or 16 isometric presses of the finger (0.3, 0.6, 1.3, and 2.6Hz pressing frequency). Each press was paced by a visual metronome, which flashed the letter cue from the announce phase for 100ms each. The first and the last press always occurred at the beginning and end of the execution phase, with the intermediate presses being cued at a constant rate (Fig. 2.1B). Following this, there was an inter-trial interval of 1s before the

next trial started. Throughout the entire experiment, participants were instructed to refrain from moving their wrist or fingers of either hand when not instructed to do so.

There were 20 possible conditions (5 fingers/letters x 4 pressing frequencies). The task was divided into 8 runs of 40 trials each, with two repeats per condition. Trial order within each run was randomized. Seven periods of rest (13s) were randomly interspersed between trials in each run. Each run lasted 411s. Participants were instructed to produce a minimum of 2N, but not to exceed a maximum of 4N with each finger press. Minimum and maximum force thresholds were visually presented on screen above the finger force lines. Between presses, the force applied to each key needed to be below 0.75N before another press could be registered. The fixation cross turned white for each correct press. Participants trained on this task prior to the scanning portion of the experiment to ensure stable performance.

2.3.4 fMRI data acquisition

Functional images were acquired using a Siemens Magnetom 7T MRI scanner with a 32-channel head coil at Western University (London, Ontario, Canada). Volumes were acquired using an interleaved, multiband slice acquisition (TR = 1000ms, 44 slices, 1.4 mm isotropic voxels, no gap between slices, in-plane acceleration factor = 3, multi-band factor = 4). The first three images of each functional run were discarded to allow magnetization to reach equilibrium. The slices covered the dorsal aspects of the cerebrum, encompassing M1 through to V1. A T1-weighted anatomical scan (3D MPRAGE sequence, TR = 6000ms, 0.75 mm isotropic voxels, 208 vol) was also acquired at the start of the scan. Fieldmaps were collected at the end of the imaging session.

2.3.5 Preprocessing and first-level model

First-level fMRI analyses were conducted with SPM12 (<http://www.fil.ion.ucl.ac.uk/spm/>). Functional images were realigned to correct for motion across runs. Within this process, we utilized a B0 fieldmap to correct for magnetic field inhomogeneities. Due to the short TR, no slice timing corrections were applied. The functional data was co-registered to the individual anatomical scan, but no normalization was applied.

The pre-processed images were analysed with a general linear model (GLM) with separate task regressors for each condition (20 regressors) for each run. Each regressor was a boxcar function that was on for 6s of the trial duration and off otherwise. These regressors were then convolved with a hemodynamic response function with a peak onset of 4.5s and a post-stimulus undershoot minimum at 11s.

We used the SPM FAST autocorrelation model in conjunction with restricted-maximum likelihood (ReML) estimation to estimate the long-range temporal dependencies in the functional timeseries. This relies on a minor modification of the standard SPM analysis routine. SPM proceeds in a two-step estimation process. First, SPM estimates an ordinary least square regression to collect sufficient statistics on the voxels in order to select voxels that are used for autocovariance estimation using ReML. By default, the inclusion of voxels is decided using an omnibus F-test (any difference in any condition vs. zero) with a threshold set to 0.001. This means voxels that are probably “involved” in the task of interest will be included. Using the FAST option to estimate the temporal covariance effectively attenuates low-temporal frequencies. This means it is unnecessary to apply a separate high-pass filter. Without additional high-pass filtering, however, very few voxels will be significant in the omnibus F-test in the first step because the data is dominated by low-frequency noise (which is now only removed in the second stage with the FAST option). Therefore, we modified the estimation procedure to specify separate masks that defined which voxels are included in the first and second steps of the analysis. Here, we were interested in optimal inferences for gray-matter. Therefore, the coefficients of this model were estimated from all gray-matter voxels using a gray-matter mask. We found that on several data sets, this analysis procedure improves the reliability of activity pattern estimates as compared to the standard high-pass filtering and subsequent temporal autocorrelation correction with FAST.

2.3.6 Region of interest (ROI) definitions

We used Freesurfer software (Dale et al., 1999) to extract the white-gray matter and pial surfaces from each participant's anatomical image. These surfaces were inflated to a sphere and aligned using sulcal depth and curvature information to the Freesurfer average atlas (fsaverage, Fischl et al., 1999). Following alignment, both hemispheres in each

participant were resampled into a 163,842 vertex grid. This allowed us to reference similar areas of the cortical surface in each participant by selecting the corresponding vertex on the group atlas.

Anatomical regions of interest (ROI) were defined using a procedure established in previous work (Wiestler and Diedrichsen, 2013; Ejaz et al., 2015). All ROIs were defined using a probabilistic cytoarchitectonic atlas (Fischl et al., 2008) projected onto the common group surface. For M1 and S1, we constrained the resulting ROIs to the hand and arm region by choosing the area of the cytoarchitectonically defined strip 2.5 cm above and below the hand knob (Yousry et al., 1997). To avoid cross-contamination between M1 and S1 activities along the central sulcus, voxels with more than 25% of their volume originating from the opposite side of the central sulcus were excluded. The primary and secondary visual cortices (V1/V2) were grouped as one ROI. The group area was then projected onto the individual volume using the individual surface reconstruction.

2.3.7 Multivariate fMRI analysis

Multi-voxel analyses were conducted within each ROI (M1, S1, and V1/V2), using the RSA (Nili et al., 2014) and PCM toolboxes (Diedrichsen et al., 2018). For each ROI, we extracted the beta-weights from the first-level GLM for each condition in each imaging run. These beta-weights were then spatially pre-whitened using multivariate noise-normalization to suppress correlated noise across voxels (Walther et al., 2016). The mean pattern was not removed from each run to preserve information about activity from baseline in each voxel.

We then calculated the squared cross-validated Mahalanobis distance (crossnobis; Walther et al., 2016; Diedrichsen et al., 2016) between activity patterns:

$$d^2(x_y, x_z) = (\mathbf{x}_y - \mathbf{x}_z)_A^T \Sigma^{-1} (\mathbf{x}_y - \mathbf{x}_z)_B$$

where $(\mathbf{x}_y - \mathbf{x}_z)_A$ corresponds to the difference between the activity patterns of conditions y and z in run A , and Σ refers to the voxel-wise noise covariance matrix (Walther et al., 2016). We repeated this procedure over all possible leave-one-run-out

cross-validation folds and then averaged the resulting dissimilarities across folds. This procedure leads to an unbiased distance estimate, which on average will be zero if there is no reliable difference between the two patterns. This also means that the crossnobis estimator can become negative. The large advantage for this measure, however, is that zero is meaningfully defined and hence ratios between distances can be interpreted in a meaningful way.

The representational geometry is characterized by the dissimilarities between all possible pairs of condition activity patterns, that can be collected into a representational dissimilarity matrix (RDM). The RDM is a (# conditions x # conditions) symmetric matrix, with zeros along the diagonal. Dissimilarities were calculated for the left hemisphere M1 and S1 ROIs (contralateral to the side of finger movements). For V1/V2 ROIs, we first calculated dissimilarities for each hemisphere, then averaged the dissimilarities across hemispheres within each participant. We used classical multi-dimensional scaling (eigenvalue decomposition) to visualize a low-dimensional projection of the representational geometry (Diedrichsen et al., 2018) in figure 2.3.

2.3.8 Stability of representational geometry across stimulation-frequencies

To assess the stability of the representational geometry across frequency conditions, we correlated the RDMs across all 6 possible frequencies pairs within each participant. For each frequency condition (j), we had 10 pairwise dissimilarities ($d_{i,j}$, where i corresponds to one of the 10 dissimilarities for frequency condition j). We calculated a Pearson correlation without subtracting the mean across the 10 dissimilarities first, as zero is a fixed and meaningful value for the unbiased crossnobis distance (see section 2.3.7). The RDM correlation between frequency conditions j and k then becomes

$$r_{j,k} = \frac{\sum_{i=1}^{10} d_{i,j} d_{i,k}}{\sqrt{\sum_{i=1}^{10} d_{i,j}^2 d_{i,k}^2}}$$

Because the RDM is a symmetric matrix, we correlated only the dissimilarities in the lower triangular of each RDM (excluding the zero diagonal values).

To compare the correlation values to a meaningful noise ceiling (see section 2.3.9), we split the data into odd and even runs and calculated crossnobis distances for each partition separately. We then calculated the correlation either between odd runs for frequency condition j and even runs for frequency condition k , or the other way around. The two correlations were then averaged for each participant and cross-frequency pair.

2.3.9 Reliability of representational geometries

Even if the representational geometry was perfectly stable across frequencies, the resultant correlations would not be 1 given the noise in our measurements. Therefore, to interpret these cross-frequency RDM correlations meaningfully, we used the reliability of each RDM to estimate a noise-ceiling for each of the 6-possible cross-frequency pairs. We measured the split-half reliability of the RDM at each frequency (r_j, r_k) using the same procedure used to calculate the cross-frequency correlations, but this time correlating the RDMs for odd and even runs within frequencies. If the true activity patterns for frequency condition j and k were identical, the expected cross-frequency correlation would be

$$E(r_{j,k}) = \sqrt{r_j * r_k}.$$

This prediction therefore provides an appropriate noise ceiling for the measured cross-frequency correlations. We then scaled the measured cross-frequency correlations to their corresponding noise ceilings, such that a value of 1 indicates the RDMs of the two frequency conditions were highly similar after correcting for measurement noise. Due to the cross-validated calculation of the cross-frequency correlations, we can encounter scaled correlations > 1 (where the cross-frequency correlation is larger than expected). We tested if the rescaled cross-frequency correlations were significantly lower than 1 using a one-tailed sign-test. Deviations significantly lower than 1 indicated that the cross-frequency RDM correlations were lower than expected given the reliability of each RDM.

2.3.10 Bayesian analysis to quantify the evidence for no RDM distortion

Given that we are also interested in quantifying the evidence for the Null-hypothesis (no distortions), we conducted a Bayesian analysis. For this, we first needed to determine what size of deviation from perfect stability would matter for model comparison, i.e., we needed to determine the effect size of the alternative hypothesis. As an example for a difficult model comparison problem, we used the muscle model and natural statistics model RDMs from Ejaz et al. (2015). Both models specify how finger movements are represented in the sensory-motor cortex. The natural statistics model hypothesizes that fingers that frequently move together evoke cortical activity patterns that are more similar. In contrast, the muscle model hypothesizes that finger movements that engage similar muscles would have a high overlap. Comparing between these models is difficult because the predicted distances from each model are highly correlated ($r = 0.9$).

As a slightly easier model comparison, we used the contrast between the somatotopic model and the natural statistics model (Ejaz et al., 2015). The somatotopic model hypothesizes that cortical activity patterns for single finger movements are arranged in an orderly fashion along the central sulcus, with some overlap between neighboring fingers. The RDMs of the somatotopic and natural statistics model were only moderately correlated ($r = 0.68$).

We simulated 1000 RDMs under each of the three models, then distorted the distances for each simulated RDM by increasing or decreasing each distance by a specific percentage of the true value. At each level of simulated distortion, we calculated the average correlation with the true model. We also determined whether the resulting RDM was closer to the true model or to the competing model with a Pearson correlation with a fixed intercept. Each misclassification was counted as a *model confusion*. Model RDMs that are more distinct would result in lower confusion rates at the same levels of distortion.

Next, we evaluated the probability of the observed cross-frequency RDM correlations from each ROI under the Null-hypothesis (no distortion, corrected $r = 1$), and various

levels of the alternative hypothesis (some distortion, corrected $r < 1$). As a distribution of the differences, we assumed a Gaussian distribution with a mean of 1 and the empirical standard deviation (σ) of the corresponding cross-frequency correlations:

$$H_0 \sim N(1, \sigma).$$

For the alternative models, we shifted the Gaussian to be centered on the average correlation for each distortion level from our simulation (r_D):

$$H_D \sim N(r_D, \sigma).$$

To obtain a Bayes factor, we averaged the empirical differences in correlations for each participant across all non-neighboring frequency pairs, and then evaluated the probability of this group data under each of the alternative models. A Bayes factor ≥ 3 is considered to be positive evidence for the hypothesis in question, and factors ≥ 20 indicate strong positive evidence (Raftery and Kass, 1995). This approach allowed us to determine the distortion levels for which we observe positive evidence in favour of the alternative model (i.e., the data is probable under this level of distortion) and the levels at which we have positive evidence in favour of the null model (i.e., the data is more likely under the null model).

2.4 Results

We measured cortical BOLD activity patterns as participants saw digits flashed repeatedly on the screen (Fig. 2.1B), and made short, isometric presses of each finger of the right hand (Fig. 2.1A). We systematically increased the stimulation and pressing frequencies (Fig. 2.1B) to increase the overall activity in the visual and motor regions. Our main question was whether the representational geometry – i.e., the collection of relative dissimilarities between different conditions, would remain relatively stable across a large range of overall activity. Behaviourally, participants were able to follow the pacing and to perform the task with relatively high accuracy and matched forces (see Table 2.1).

	Pressing freq. (Hz)	Force (N)						
Cued freq.	0.3Hz		0.6Hz		1.3Hz		2.6Hz	
Thumb	0.33 (0.02)	3.04 (0.08)	0.66 (0.03)	3.12 (0.05)	1.32 (0.04)	3.18 (0.07)	2.65 (0.10)	3.13 (0.07)
Index	0.32 (0.03)	2.82 (0.07)	0.65 (0.04)	2.91 (0.07)	1.33 (0.02)	2.99 (0.05)	2.67 (0.21)	2.97 (0.07)
Middle	0.34 (0.02)	3.62 (0.16)	0.67 (0.02)	3.53 (0.14)	1.34 (0.03)	3.52 (0.14)	2.70 (0.14)	3.39 (0.11)
Fourth	0.33 (0.04)	2.94 (0.08)	0.67 (0.04)	2.99 (0.05)	1.34 (0.03)	3.07 (0.05)	2.63 (0.24)	2.98 (0.07)
Little	0.33 (0.02)	2.99 (0.06)	0.65 (0.04)	2.99 (0.05)	1.32 (0.05)	3.11 (0.04)	2.66 (0.21)	2.97 (0.05)

Table 2.1: Finger pressing behaviour during MRI data acquisition.

Mean and (in parentheses) between-subject standard error of behavioural measure of the finger pressing task. The pressing frequency is reported in Hertz (Hz), and forces in Newtons (N). Participants (n=8) were able to approximately match the instructed frequency and keep the pressing forces relatively stable.

Figure 2.2A shows a surface representation of the activity patterns in the left hemisphere hand region of primary motor and sensory cortices (M1 and S1) from one participant. The overlapping nature of the activity patterns for the different fingers is clearly visible, as well as an overall gradient with the thumb activating more ventral and the little finger more dorsal aspects of the hand region. The overall intensity of the activity increased with increasing pressing frequency, but the spatial distribution of the activity associated with each finger movement appeared to remain stable. Overall, we observed an approximately 5-fold increase in M1 and S1 (Fig. 2.2B), with less activity evoked in visual cortices (V1/ V2).

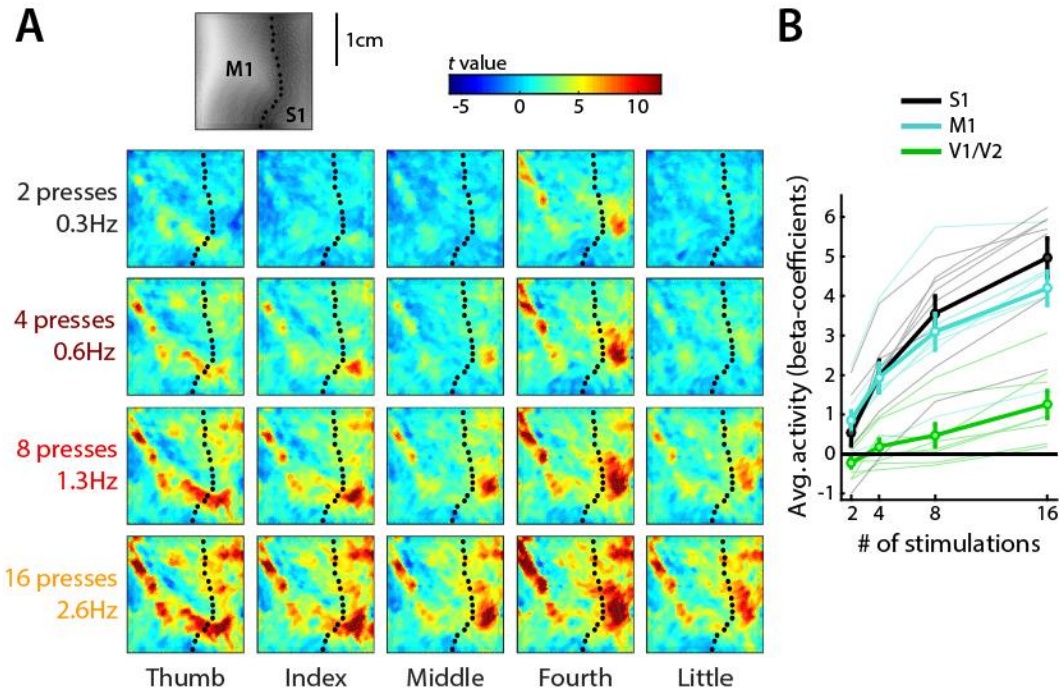


Figure 2.2: Scaling of fMRI activity patterns

(A) BOLD activity patterns from the hand area of the primary sensorimotor cortices of an example participant projected onto a flat, surface reconstruction of their cortex. Dotted lines indicate the fundus of the central sulcus. The top insert reflects sulcal depth (darker colours reflect larger depths) and denotes location of M1 and S1. Colour maps reflect t-values of activity against rest. Each column corresponds to one finger (thumb to little), and each row one pressing frequency (0.3 to 2.6Hz). The activity increases with increasing pressing frequency.

(B) Activity (beta-coefficients) in contralateral M1, S1, and bilateral V1/V2 as a function of pressing/stimulation frequency. Data from each participant are plotted. The group average for each region are plotted in bold. Error bars reflect s.e.m. across participants.

Our main interest was whether intensity-dependent variations in neural-to-BOLD coupling would lead to distortions of the representational geometry. Therefore, to assess this, we calculated the dissimilarity between pairs of activity patterns for each condition of the same frequency (i.e., the representational geometry), for each ROI in each participant. We then examined how stable this geometry remained despite the nearly 5-fold increase in overall activity. As a first step, we visualized the group average representational geometry in M1 (S1 representational geometries are very similar to those in M1: see Ejaz et al., 2015) and V1/V2 using a multi-dimensional scaling plot.

For M1 (Fig. 2.3A), we observed the expected representational geometry with the thumb having the most unique pattern and the other fingers being arranged according to their neighborhood relationship (Ejaz et al., 2015). As pressing frequency increased, this arrangement scaled up and substantially moved away from resting baseline (Fig. 2.3A, cross), but the overall geometry remained the same. This stability can also be appreciated when visualizing the 10 pairwise dissimilarities between fingers for each frequency (Fig. 2.4A, E).

In the visual cortices (V1/V2), we observed a distinct arrangement of the conditions, with the representational geometry relating to the letters and colours presented for each finger. Similarly to M1 and S1, this structure scaled up with increasing stimulation frequency (Fig. 2.3B). However, the lowest stimulation frequency was not very successful in eliciting either average activity or very reliable activity patterns (see below).

To quantify the stability of the representational geometry across different levels of activity, we correlated the dissimilarities in M1, S1, and V1/V2 (Fig. 2.4A, E, J) across frequencies within each participant. The average cross-frequency correlations (Pearson correlation without intercept – see methods) was $r = 0.92$ in M1 (Fig. 2.4B) and $r = 0.94$ in S1 (Fig. 2.4F). In V1/V2 (Fig. 2.4J), cross-frequency correlations were lower when they involved the lowest stimulation frequency (average of all cross-frequency correlations was 0.69), but increased with stimulation frequency (the average cross-frequency correlation between the RDMs of the two highest frequencies was 0.95).

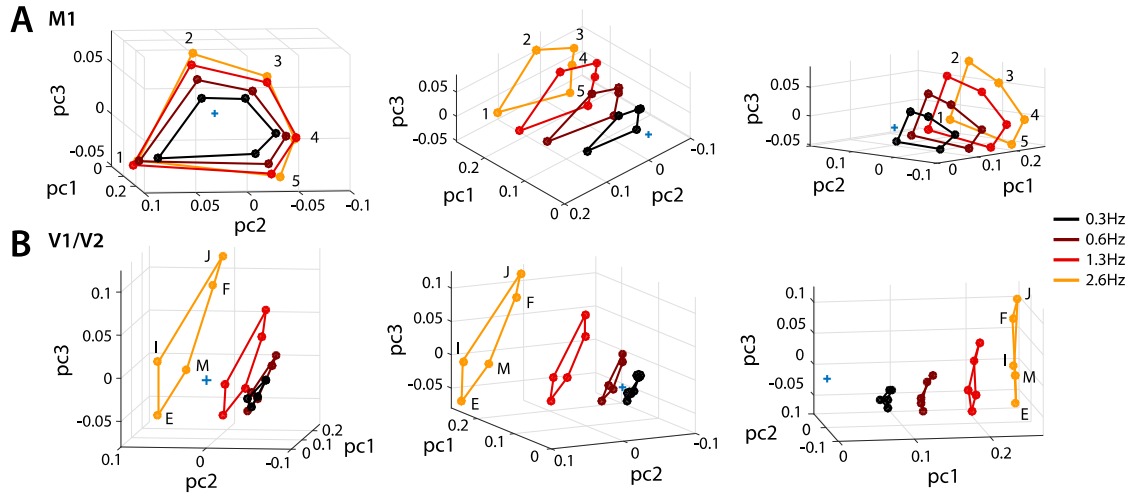


Figure 2.3: Multidimensional scaling of group average representational geometries

Multidimensional scaling of group average representational geometries for M1 (A) and bilateral V1/V2 (B). Colours correspond to pressing/stimulation frequency. Numbers indicate fingers (1 = thumb, 5 = little finger). Letters correspond to the flashed letter cue (1=E, 2=I, 3=M, 4=F, 5=J). Note that the conditions are connected differently for M1 and V1/V2. Panels in the same row present different views of the same space, defined by the first three eigenvectors. The blue cross indicates baseline.

Figure 2.4: Stability of representational geometry across stimulation frequencies

(A) Average dissimilarity between all possible pairs of the five activity patterns measured at each frequency in M1. Colours indicate pressing/stimulation frequency, and shaded regions reflect s.e.m. across participants.

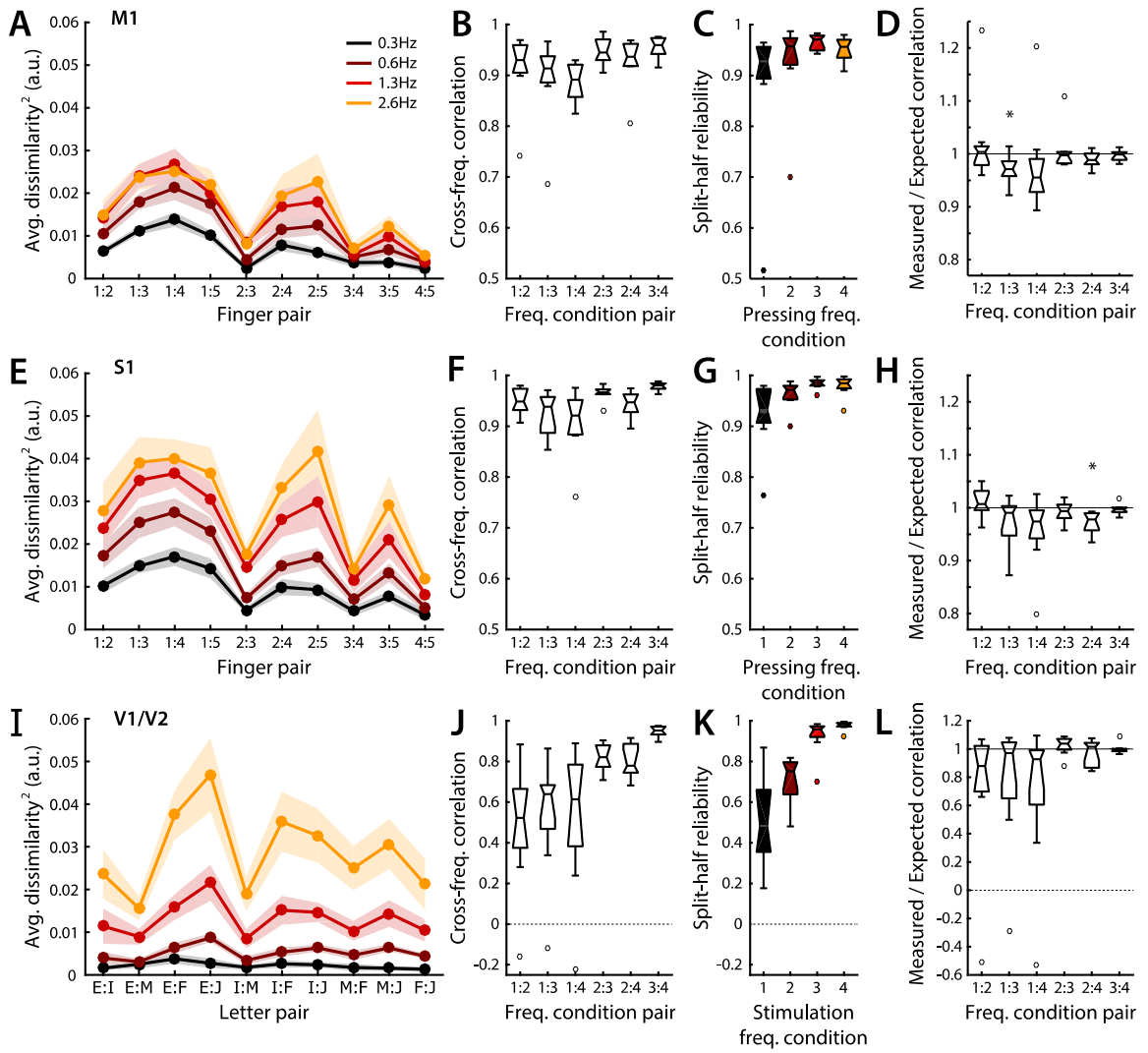
(B) Cross-frequency correlations (see methods) between dissimilarities depicted in A. The box plot extends from the 25th to 75th percentiles, and whiskers extend to the full range of the data. The line in the center of each box denotes the median. Outliers (circles) are points more than 1.5 times the box length away from the median.

(C) Within participant split-half reliabilities (Pearson correlation with a forced intercept) of the dissimilarities depicted in A.

(D) Measured cross-frequency correlations from B scaled by their respective expected correlations (noise ceiling, see methods). Values < 1 indicate the observed correlation (stability) is lower than what would be expected given the internal reliability of each RDM. Deviations from 1 were evaluated with one-tailed signed rank tests. Asterisks indicate significant deviations ($p < 0.05$). The outlier data in M1 does not drive this result.

(E-H) Results for S1.

(I-L) Results for V1/V2. Note that the representational geometry in visual regions is different from the one found in M1/S1, reflecting the finger-to-letter assignment. Due to low stimulation intensity, visual regions have lower reliabilities for low stimulation frequencies.



Given measurement noise in the data, however, the cross-frequency correlations are expected to be < 1 even if they are perfectly stable. Therefore, to quantify the stability of the representational geometry, we calculated a noise-ceiling (the expected correlation if the true patterns were identical across frequencies-see Methods) for each cross-frequency pair. We first determined the split-half reliabilities of the RDMs within each frequency. In M1 and S1, the average split-half reliabilities across participants (Fig. 2.4C, G) was high ($r > 0.88$) for all pressing frequencies. In V1/V2 (Fig. 2.4K), the reliabilities of the dissimilarities measured at the slowest stimulation frequencies were lower, likely due to low levels of evoked activity, but increased comparably to reliabilities measured for M1 and S1 at higher frequencies (average split-half reliabilities across participants in V1/V2 for all stimulation frequencies was 0.78). We then estimated the noise-ceilings for each cross-frequency pair by calculating the geometric means of pairs of split-half reliabilities for different frequencies within each participant (see Methods).

Comparison between the measured and the expected (noise ceiling) correlations confirmed that the representational geometries remained as stable as could be expected based on the level of measurement noise across a broad range of overall activities. The right-most column in figure 2.4 shows the measured cross-frequency correlations as a ratio of their respective noise-ceilings. Values < 1 indicate that the measured correlations were lower than expected given an estimate of measurement noise for that cross-frequency pair, whereas values > 1 indicate the opposite. In V1/V2, one-tailed sign-tests indicated the measured cross-frequency correlations did not significantly differ from their estimated noise ceilings (p -values evaluated without corrections for multiple comparisons). In M1, only the measured correlations for the lowest and third highest frequency (Fig. 2.4D, pair 1 vs. 3) deviated significantly from the expected correlations ($p = 0.035$). In S1, the only significant deviations were for frequency condition pair 2 vs. 4 (Fig. 2.4H, $p = 0.004$). Although these deviations in M1 and S1 are statistically significant, the magnitude of these deviations were minor (average rescaled cross-frequency correlations in M1 and S1 = 0.97). More importantly, the correlations between the RDMs measured at the lowest and highest activity level were not significantly different from the noise ceiling estimates.

To assess whether these relatively minor distortions would be of practical relevance, we assessed their influence on model inference through simulations. For different levels of distortions, we determined the model confusion rate for a difficult model comparison problem (model RDMs are correlated with $r = 0.9$, see Methods), and a moderate model comparison problem ($r = 0.68$). As can be seen in figure 2.5A, the model confusion rate increased with increasing levels of RDM distortion. However, at the observed distortion rates (dashed lines in Fig. 2.5A), the confusion rates were below 12%, even for the difficult model inference.

To quantify the statistical evidence that our data shows no distortion (the Null-hypothesis), we calculated the Bayes Factor (BF, see Methods) of the Null against distortions of various sizes. Because we were interested in distortions that would arise due to intensity-dependent variations in neural-to-BOLD coupling, we analysed the empirical differences between 1 and the cross-frequency correlations (corrected to their respective noise-ceiling) for all non-neighboring cross-frequency pairs (averaged across pairs within each participant). Figure 2.5B shows the log Bayes factor for various levels of distortion for the three ROI. We obtained positive evidence ($|\text{BF}| \geq 3$) in favour of the null at a distortion of $r = 0.95$ for M1 and for $r = 0.93$ for S1, which were associated with a model confusion rate of 5–17% and 9–19%. For V1/V2, we excluded the lowest stimulation frequency, as we could not measure the representational structure reliably here. We observed positive evidence against a higher distortion level ($r = 0.91$) corresponding to a confusion range of approximately 12–28%. Evidence in favour of the Null hypothesis for these high distortion levels indicates the true distortion is substantially lower. Indeed, the average of the non-neighboring scaled cross-frequency correlations in M1, S1, and V1/V2 were close to 1 (M1: $r = 0.98$, S1: $r = 0.97$, V1/V2: $r = 0.97$). The evidence for the alternative hypothesis at these levels of distortion was weak in M1 ($|\text{BF}| = 2.8$) and positive in S1 ($|\text{BF}| = 9$). The associated model confusion rates were 0–6% in M1 and 2–12% in S1, respectively. We did not observe positive evidence for RDM distortions at any level in V1/V2.

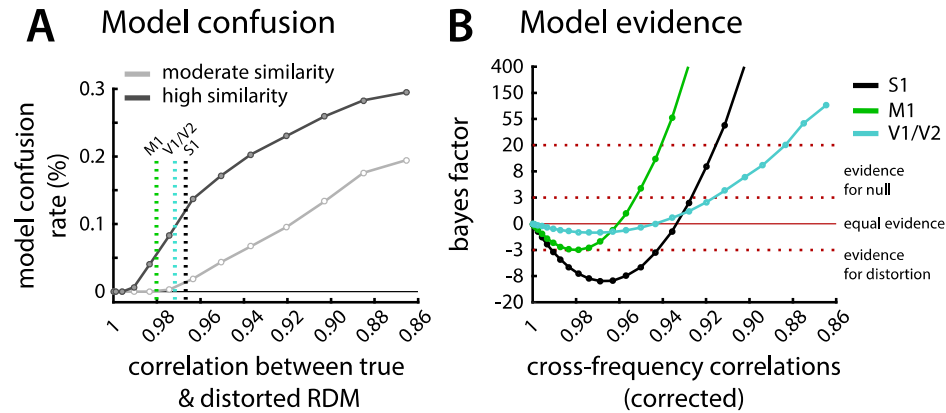


Figure 2.5: The effect of RDM distortions on representational model comparisons.

(A) Simulated model confusion rates between two highly correlated (dark gray, $r = 0.9$) and two moderately correlated (light gray, $r = 0.68$) model RDMs (see section 2.10). Dotted lines reflect the average observed cross-frequency correlations (scaled to noise-ceilings) from each of the three ROIs. RDMs are more commonly misclassified as distortion increases (shown here as a decrease in the correlation between the true and distorted RDM). The magnitude of misclassification depends on how similar the two model RDMs are.

(B) Bayes factors (BF) for evidence of the null (no distortion) over the alternative (distortion) models for increasing levels of RDM distortion (x-axis). Negative BF indicate evidence in favor of the alternative model, which means that the cross-frequency RDM correlations are more probable under the corresponding level of distortion. In contrast, positive BF indicate evidence in favor of the null model, suggesting that the cross-frequency RDM correlations exhibit a lower level of distortion than the corresponding level tested. The dashed red lines indicate the thresholds for positive evidence ($|\text{BF}| \geq 3$) and strong evidence ($|\text{BF}| \geq 20$).

Together, these results demonstrate that the relationship between crossnobis dissimilarities remains relatively stable across a broad range of overall activity in sensorimotor cortices, and to a lesser extent in and primary and secondary visual cortices.

2.5 Discussion

Here we critically investigated whether there are measurable distortions of the representational geometry as measured by BOLD as overall neural activity increases. We tested this assumption by stimulating both sensory-motor and visual regions at increasing frequencies. We assumed that on the neural level, each repeated event should elicit approximately the same activity pattern. Therefore, the temporally integrated patterns should scale in an orderly fashion across frequencies. Importantly, this does not imply that neural activity would increase linearly with the number of events. Indeed, previous findings have shown that the neural response to subsequent finger taps is strongly attenuated in M1 (Hermes et al., 2012). However, as pointed out in the introduction, this non-linearity between behavioural and average BOLD does not provide insight into whether the representational geometry would distort.

Indeed, we found that in M1 and S1 the representational geometry scales in a relatively orderly manner, even though the local activity increased over a large dynamic range – likely close to the achievable maximum for this paradigm. The drop in correlation across pressing frequencies (as compared to the noise ceiling derived from within-frequency consistency) was minor ($r=0.97$ on average). It also needs to be kept in mind that some of the observed distortions may have been due to real changes in the representational geometry of the neural activity patterns - after all our assumption that the neural representational geometry would be completely stable may not be true. Thus, our results provide an upper bound for distortions that can be attributed the neural-to-BOLD coupling. Our ability to identify the correct representational model at this level of distortion remained good, even for a difficult model comparison.

Our results in V1/V2 were slightly weaker. While the measured distortions were at a similar level as in M1/S1, the variability of our RDM estimates were much higher in than in sensorimotor regions, especially for lower stimulation frequencies. This likely reflects

limitations in our task design, which succeeded in driving the overall activity level in M1 and S1 across a large range, but was not optimal to elicit maximal activity in visual regions.

Overall, our findings provide an important extension of previous studies that report linear coupling between neural activity and BOLD responses in M1/S1 (Siero et al., 2013) and V1 (Boynton et al., 1996; Heeger et al., 2000). Showing that BOLD signal and neural activity are linearly coupled on average does not guarantee that the fine-grained activity patterns would also retain their representational geometry. For this, every individual voxel would have to obey the same scaling function. Testing this commonly-held assumption, we provide here the strongest empirical evidence to date that the dissimilarities of multivariate fMRI activity patterns are stable across a wide range of activation levels. Our findings are broadly consistent with a PCM-style analysis of the same data (Diedrichsen, Yokoi, & Arbuckle, 2018), which already showed the stability of the representational structure on the group level in M1. The current paper extends these results by quantifying the stability on the individual level, in multiple brain regions, and by estimating the effect the distortions may have on model comparison.

These findings have important implications for multivariate fMRI analyses. In general, most papers rely explicitly or implicitly on the assumption that the representational geometry as measured with fMRI veridically reflects the representational geometry of the underlying neural population code. While this strong assumption may still be violated for other reasons (see below), we at least show here that the representational geometry can be meaningfully compared across a large range of overall activation levels. Thus, under appropriate conditions, representational geometries can be compared across different regions, individuals, or patient populations. Furthermore, from our data it appears justified to compare RDMs between different attentional states or different levels of learning, even if these differ in their average activity. Given our results, changes in the representational geometry across these conditions are likely due to real changes in the underlying neural population code, rather than due to distortions induced by neural-to-BOLD coupling.

For RSA, these findings also have implications for the choice of a dissimilarity measure. Not all measures make equally strong assumptions about the relation between the underlying neural representational geometry and the one measured with fMRI. For example, a common practice in RSA is to evaluate rank-correlation between measured and predicted RDMs. Arguably, this approach makes interpretations more robust against minor distortions in the measurement process (Kriegeskorte, Mur, & Bandettini, 2008; Nili et al., 2014). Our results indicate that the exact ratio-relationship between dissimilarity measures can be meaningfully interpreted across a large range of average activation states. For this to be true, we of course need to use a dissimilarity measure that provides a meaningful zero point unbiased by noise – a condition met by the crossnobis estimator (Diedrichsen et al., 2016; Kriegeskorte & Diedrichsen, 2016; Walther et al., 2016). The additional information in the exact ratio-relationships allow for more powerful inference about the underlying representations (Diedrichsen & Kriegeskorte, 2017).

The stability of the representational geometry is also good news for alternative approaches that test representational models. PCM (Diedrichsen et al., 2011; Diedrichsen, Yokoi, and Arbutle 2018) and encoding models (Naselaris, Kay, Nishimoto, & Gallant, 2011) make inferences about the underlying representational geometry in a very similar way to RSA (Diedrichsen & Kriegeskorte, 2017). Therefore, PCM and encoding approaches are subject to similar assumptions as RSA – and our findings generalize, such that inferences using these two methods will also be stable across activity levels.

Do these results suggest that one can make inferences about the representational geometry of the underlying neural population code from fMRI measures? While our results are reassuring in some aspects, there are two important caveats that we did not address in the current paper. First, fMRI samples neural activity with dramatic spatial averaging, even when using sub-millimeter resolution. Representations that exist at a finer spatial scale in the neural population code will be under-represented in BOLD activity patterns, while representations at a large spatial scale will be over-represented (see Kriegeskorte & Diedrichsen, 2016). Therefore, the representational geometry of BOLD activity patterns may differ systematically from the underlying neural code.

Secondly, the physiological processes underlying the BOLD signal and underlying extracellular neural recording are fundamentally different: While the BOLD signal reflects to a large degree the metabolically expensive processes of ion transport after excitatory postsynaptic potentials (Attwell & Laughlin, 2001; Harris, Jolivet, & Attwell, 2012), extracellular recordings reflect neural spiking. Crudely stated, therefore, BOLD reflects more the input to a region, while neural extracellular recordings reflect the output. Additionally, most extracellular recordings are biased towards large output neurons, as these provide the clearest extracellular signal (Firmin et al., 2014; Harris et al., 2016), whereas the BOLD signal indiscriminately averages metabolic activity. These important caveats need to be kept in mind when drawing parallels between representational analysis of extracellular recordings and BOLD signal.

2.5.1 Conclusion

One common assumption in multivariate fMRI analyses is that the relationship between activity patterns can be meaningfully interpreted. Intensity-dependent variations in neural-to-BOLD coupling, however, could lead to substantial distortions of multivariate measures when overall activity increases. Our results demonstrate that, across a broad range of overall activation states in M1 and S1 the ratio-relationships between pair-wise dissimilarities remain stable. This suggests that it is viable to leverage more powerful techniques, such as the use of cross-validated dissimilarities and likelihood-based RSA (Diedrichsen et al., 2016; Diedrichsen & Kriegeskorte, 2017), for model comparison. The finding also applies to other multivariate techniques that analyse the relationship of BOLD activity patterns.

2.6 References

- Adrian E. Raftery, & Robert E. Kass. (1995). Bayes Factors. *Journal of the American Statistical Association*, 90(430), 773–795.
- Attwell, D., & Laughlin, S. B. (2001). An Energy Budget for Signaling in the Grey Matter of the Brain. *Journal of Cerebral Blood Flow & Metabolism*, 21(10), 1133–1145.
- Boynton, G. M., Engel, S. A., Glover, G. H., & Heeger, D. J. (1996). Linear systems analysis of functional magnetic resonance imaging in human V1. *Journal of Neuroscience*, 16(13), 4207–21.
- Brouwer, G. J., & Heeger, D. J. (2009). Decoding and reconstructing color from responses in human visual cortex. *The Journal of Neuroscience*, 29(44), 13992–14003.
- Dale, A. M., Fischl, B., & Sereno, M. I. (1999). Cortical surface-based analysis. I. Segmentation and surface reconstruction. *NeuroImage*, 9(2), 179–194.
- de-Wit, L., Alexander, D., Ekroll, V., & Wagemans, J. (2016). Is neuroimaging measuring information in the brain? *Psychonomic Bulletin and Review*, 23(5), 1415–1428.
- deCharms, R. C., & Zador, A. (2000). Neural Representation and the Cortical Code. *Annual Review of Neuroscience*, 23(1), 613–647.
- Diedrichsen, J., & Kriegeskorte, N. (2017). Representational models: A common framework for understanding encoding, pattern-component, and representational-similarity analysis. *PLOS Computational Biology*, 13(4), e1005508.
- Diedrichsen, J., Provost, S., & Zareamoghaddam, H. (2016). On the distribution of cross-validated Mahalanobis distances. *arXiv*.
- Diedrichsen, J., Ridgway, G. R., Friston, K. J., & Wiestler, T. (2011). Comparing the similarity and spatial structure of neural representations: A pattern-component model. *NeuroImage*, 55(4), 1665–1678.
- Diedrichsen, J., Yokoi, A., & Arbuttle, S. A. (2018). Pattern component modeling: A flexible approach for understanding the representational structure of brain activity patterns. *NeuroImage*, 180, 119–133.
- Ejaz, N., Hamada, M., & Diedrichsen, J. (2015). Hand use predicts the structure of representations in sensorimotor cortex. *Nature Neuroscience*, 18(7).
- Firmin, L., Field, P., Maier, M. A., Kraskov, A., Kirkwood, P. A., Nakajima, K., ... Glickstein, M. (2014). Axon diameters and conduction velocities in the macaque pyramidal tract. *Journal of Neurophysiology*, 112(6), 1229–1240.
- Fischl, B., Rajendran, N., Busa, E., Augustinack, J., Hinds, O., Yeo, B. T. T., ... Zilles, K. (2008). Cortical Folding Patterns and Predicting Cytoarchitecture. *Cerebral Cortex*, 18(8), 1973–1980.

- Fischl, B., Sereno, M. I., Tootell, R. B., & Dale, A. M. (1999). High-resolution intersubject averaging and a coordinate system for the cortical surface. *Human Brain Mapping*, 8(4), 272–84.
- Harris, J. J., Jolivet, R., & Attwell, D. (2012). Synaptic Energy Use and Supply. *Neuron*, 75(5), 762–777.
- Harris, K. D., Quiroga, R. Q., Freeman, J., & Smith, S. L. (2016). Improving data quality in neuronal population recordings. *Nature Neuroscience*, 19(9), 1165–74.
- Haxby, J. V., Connolly, A. C., & Guntupalli, J. S. (2014). Decoding Neural Representational Spaces Using Multivariate Pattern Analysis. *Annual Review of Neuroscience*, 37(1), 435–456.
- Haxby, J. V., Gobbini, M. I., Furey, M. L., Ishai, A., Schouten, J. L., & Pietrini, P. (2001). Distributed and Overlapping Representations of Faces and Objects in Ventral Temporal Cortex. *Science*, 293(5539), 2425–2430.
- Heeger, D. J., Huk, A. C., Geisler, W. S., & Albrecht, D. G. (2000). Spikes versus BOLD: what does neuroimaging tell us about neuronal activity? *Nature Neuroscience*, 3(7), 631–633.
- Hermes, D., Siero, J. C. W., Aarnoutse, E. J., Leijten, F. S. S., Petridou, N., & Ramsey, N. F. (2012). Dissociation between Neuronal Activity in Sensorimotor Cortex and Hand Movement Revealed as a Function of Movement Rate. *Journal of Neuroscience*, 32(28), 9736–9744.
- Kriegeskorte, N., & Diedrichsen, J. (2016). Inferring brain-computational mechanisms with models of activity measurements. *Philosophical Transactions of the Royal Society of London. Series B, Biological Sciences*, 371(1705), 20160278.
- Kriegeskorte, N., Mur, M., & Bandettini, P. (2008). Representational similarity analysis - connecting the branches of systems neuroscience. *Frontiers in Systems Neuroscience*, 2, 4.
- Kriegeskorte, N., Mur, M., Ruff, D. A., Kiani, R., Bodurka, J., Esteky, H., ... Bandettini, P. A. (2008). Matching categorical object representations in inferior temporal cortex of man and monkey. *Neuron*, 60(6), 1126–41.
- Miyawaki, Y., Uchida, H., Yamashita, O., Sato, M., Morito, Y., Tanabe, H. C., ... Kamitani, Y. (2008). Visual image reconstruction from human brain activity using a combination of multiscale local image decoders. *Neuron*, 60(5), 915–929.
- Naselaris, T., Kay, K. N., Nishimoto, S., & Gallant, J. L. (2011a). Encoding and decoding in fMRI. *NeuroImage*, 56(2), 400–410.
- Naselaris, T., Kay, K. N., Nishimoto, S., & Gallant, J. L. (2011b). Encoding and decoding in fMRI. *NeuroImage*, 56(2), 400–410.
- Nili, H., Wingfield, C., Walther, A., Su, L., Marslen-Wilson, W., & Kriegeskorte, N. (2014). A Toolbox for Representational Similarity Analysis. *PLoS Computational Biology*, 10(4), e1003553.

- O'Herron, P., Chhatbar, P., Levy, M., Shen, Z., Schramm, A., Lu, Z., & Kara, P. (2016). Neural correlates of single-vessel haemodynamic responses in vivo. *Nature*, 534, 378–394.
- Siero, J. C., Hermes, D., Hoogduin, H., Luijten, P. R., Petridou, N., & Ramsey, N. F. (2013). BOLD consistently matches electrophysiology in human sensorimotor cortex at increasing movement rates: a combined 7T fMRI and ECoG study on neurovascular coupling. *Journal of Cerebral Blood Flow & Metabolism*, 3397(10), 1448–1456.
- Walther, A., Nili, H., Ejaz, N., Alink, A., Kriegeskorte, N., & Diedrichsen, J. (2016). Reliability of dissimilarity measures for multi-voxel pattern analysis. *NeuroImage*, 137, 188–200.
- Wiestler, T., & Diedrichsen, J. (2013). Skill learning strengthens cortical representations of motor sequences. *ELife*, 2013(2).
- Yousry, T. A., Schmid, U. D., Alkadhi, H., Schmidt, D., Peraud, A., Buettner, A., & Winkler, P. (1997). Localization of the motor hand area to a knob on the precentral gyrus. A new landmark. *Brain*, 120(1), 141–157.

Chapter 3

3 Structure of population activity in primary motor cortex for single finger flexion and extension

In the previous chapter I validated the stability of representational analyses with fMRI data. In my next project, I used this analysis framework to examine how M1 is organized to control finger flexion and extension movements. Under the movement co-occurrence hypothesis, one would predict that since flexion and extension of the same finger can never co-occur (from a kinematic perspective), finger flexion and extension should be associated with distinct brain representations. I tested this prediction using human fMRI and compared the results to neural spiking patterns recorded in two monkeys performing an identical task.

3.1 Abstract

How is the primary motor cortex (M1) organized to control fine finger movements? We investigated the population activity in M1 for single finger flexion and extension, using 7T functional magnetic resonance imaging (fMRI) in female and male human participants, and compared these results to the neural spiking patterns recorded in two male monkeys performing the identical task. fMRI activity patterns were distinct for movements of different fingers, but quite similar for flexion and extension of the same finger. In contrast, spiking patterns in monkeys were quite distinct for both fingers and directions, similar to what was found for muscular activity patterns. The discrepancy between fMRI and electrophysiological measurements can be explained by two (non-mutually exclusive) characteristics of the organization of finger flexion and extension movements. Given that fMRI reflects predominantly input and recurrent activity, the results can be explained by an architecture in which neural populations that control flexion or extension of the same finger produce distinct outputs, but interact tightly with each other and receive similar inputs. Additionally, neurons tuned to different movement directions for the same finger (or combination of fingers) may cluster closely together, while neurons that control different finger combinations may be more spatially separated. When measuring this organization with fMRI at a coarse spatial scale, the activity

patterns for flexion and extension of the same finger would appear very similar. Overall, we suggest that the discrepancy between fMRI and electrophysiological measurements provides new insights into the general organization of fine finger movements in M1.

3.2 Introduction

Dexterous movements of fingers require accurate coordination of different hand muscles. Hand muscles are innervated by motoneurons in the ventral horn of the spinal cord, which receive direct and indirect projections from the hand region of the contralateral primary motor cortex (M1) (Lemon, 2008). In monkey species capable of better finger individuation, direct (monosynaptic) projections from M1 to ventral horn motor neurons are more pronounced (Heffner & Masterton, 1983; Bortoff & Strick, 1993). Lesions to the corticospinal tract (Tower, 1940; Lawrence & Kuypers, 1968; Lawrence & Hopkins, 1976; Sasaki et al., 2004) or to M1 (permanent: Liu & Rouiller, 1999; Darling et al., 2009; reversible: Schieber & Poliakov, 1998) result in a significant loss of finger individuation. Such symptoms are also reported in human stroke patients who have damage to the hand area of M1 or the descending corticospinal pathway (Lang & Schieber, 2003; Xu et al., 2017). These results indicate that M1 is important for the fine control of individuated finger movements.

What is less well understood is how this cortical control module for finger movements is organized. Here, we studied this question by investigating cortical activation patterns evoked during flexion and extension of individual fingers. Previous electrophysiological work in macaque monkeys (Schieber & Hibbard, 1993; Schieber & Poliakov, 1998) have indicated that motor cortical neurons have complex tuning functions, often responding to movements of multiple fingers and to both flexion and extension movements. Therefore, there exists no clearly organized “map”, with separate regions dedicated to the control of a single finger. Instead, the population of M1 neurons involved in hand control must be organized by some other principle.

One plausible principle is that the statistics of natural hand use shapes the organization of neuronal populations in the hand region of M1. This idea predicts that movements that commonly co-occur in every-day life are represented in overlapping substrates in M1

(Graziano & Aflalo, 2007). In humans, fingers with high correlations between their joint-angle velocities during every-day hand movements (Ingram, et al., 2008) have been shown to have more similar M1 activity patterns, as measured with fMRI (Ejaz et al., 2015). The correlation structure of every-day finger movements nearly fully explained the relative similarities of M1 finger activity patterns, and fit the data better than a model that used the similarity of the required muscle activity patterns (i.e., predicting that movements that use similar muscles also have similar activity patterns) or a somatotopic model (i.e., predicting that fingers are represented in an orderly finger map).

In this paper, we asked to what degree this kinematic hypothesis could generalize to movements of the same finger in different directions. We measured the activity evoked in the hand area of M1 using high-field fMRI while human participants performed near-isometric single finger flexion and extension presses with their right hand. By extrapolating the model used in Ejaz et al. (2015) to this situation, we predicted that each movement should have its own, clearly separated representation in M1, as flexion and extension movements of the same finger can never co-occur. Indeed, it has been recently suggested that human motor cortex has multiple representations of each finger, one dedicated to flexion and one to extension (Huber et al., 2020).

We found, however, that the measured M1 fMRI patterns for flexion and extension of the same finger were strikingly similar, much more similar than would be expected for two movements that cannot co-occur. This similarity was not the result of co-contraction during the task. To better understand these results, we investigated the representational structure of single-neuron activity in M1 of two macaque monkeys trained on the same flexion-extension task (data from Schieber & Rivlis, 2005; Schieber & Rivlis, 2007). The spiking patterns in monkeys were quite distinct for fingers and directions. From these results, we propose two, non-mutually exclusive hypotheses about the organization of finger movement representations in the primary motor cortex.

3.3 Methods

3.3.1 Human participants

Nine healthy participants were recruited for the study (5 males and 4 females, mean age=24.78, SD=4.68; mean Edinburgh handedness score=90.11, SD=11.34). Participants completed 3 experimental sessions. During the first training session, participants learned to perform the finger individuation task. In the scanner session, participants performed the finger individuation task while undergoing fMRI. In the EMG session, participants performed the finger individuation task while muscle activities were recorded. All participants provided informed consent before the beginning of the study, and all procedures were approved by the Office for Research and Ethics at the University of Western Ontario.

3.3.2 Experimental design of human finger individuation task

In all three (training, scanning, and EMG) sessions, the five fingers of the right hand were individually clamped between two keys (Fig. 3.1A). Foam padding on each key ensured each finger was comfortably restrained. Force transducers (Honeywell-FS series, dynamic range=0-16N, resolution<0.02N, sampling rate=200Hz) above and below each key monitored the forces applied by each finger in extension and flexion directions.

During the task, participants viewed a screen that presented two rows of five bars (Fig. 3.1B). These bars corresponded to flexion or extension direction for each of the five fingers of the right hand. The forces applied by each finger were indicated on the visual display as five solid white lines (one per finger). On each trial, participants were cued to make an isometric, single-finger flexion or extension press at one of three forces levels (1, 1.5, or 2N for extension; 1.5, 2, or 2.5N for flexion) through the display of a white target box (Fig. 3.1B). Extension forces were chosen to be lower than flexion forces, as extension finger presses are more difficult (Valero-Cuevas, Zajac, & Burgar, 1998; Li, et al., 2003) and can lead to more enslaving (i.e., co-articulation) of non-instructed fingers (Yu, Duinen, & Gandevia, 2010). This design yielded two levels of matched target forces for flexion and extension presses (1.5 and 2N). The forces were similar to the low forces

required in the monkey task design. The finger displacement required to achieve these force thresholds was minimal, such that the finger presses were close to isometric.

Each trial lasted 6000ms and consisted of four phases (Fig. 3.1B): a cue phase (1500ms), a press phase (2000ms), a hold phase (1000ms), and a 1500ms inter-trial interval. This trial structure was designed to mirror the NHP task (see NHP methods and also Schieber, 1991). During the cue phase, a white box appeared in one of the ten finger bars presented on screen, indicating the desired finger and direction. The desired pressing force was reflected by the relative location of the cue within the finger bar. After 1500ms, the cue turned green. This instructed the participant to initiate the finger press. Participants had up to 2000ms after the cue turned green to reach the specified force. Once the pressing force was within the target box (target force $\pm 12.5\%$) the cue turned blue. Participants were trained to hold the force constant within this interval for 1000ms. When this time had elapsed, the cue disappeared and the participants were instructed to release the press by relaxing their hand. Importantly, participants were instructed not to actively move the finger in the opposite direction. A new trial started every 6s. For the scanning session, periods of rest were randomly intermixed between trials (see below). The muscle recording sessions lacked these rest periods, but otherwise had the same trial structure.

Trials of the 30 conditions (5 fingers x 2 directions x 3 forces) were presented in a pseudo-random order. Trials were marked as errors if the participant was too slow (i.e., did not initiate movement within 2000ms of the go-cue), pressed the wrong finger or in the wrong direction, or if the participant did not reach at least 0.5N force with the cued finger in the cued direction. Due to the pre-training, the participants had low error rates in both the fMRI (mean error rate across conditions = $1.48\% \pm 1.05\%$ sem) and EMG (mean error rate across conditions = $1.30\% \pm 0.97\%$) sessions, and accurately produced the required target forces (fMRI: mean peak force accuracy = $108.93\% \pm 2.56\%$ of the target forces; EMG: mean accuracy = $107.80\% \pm 2.19\%$). Therefore, we included all trials in subsequent analyses.

We also did not exclude any trials based on finger co-activation. Overall, participants were able to individuate their fingers relatively well. During fMRI extension trials, the

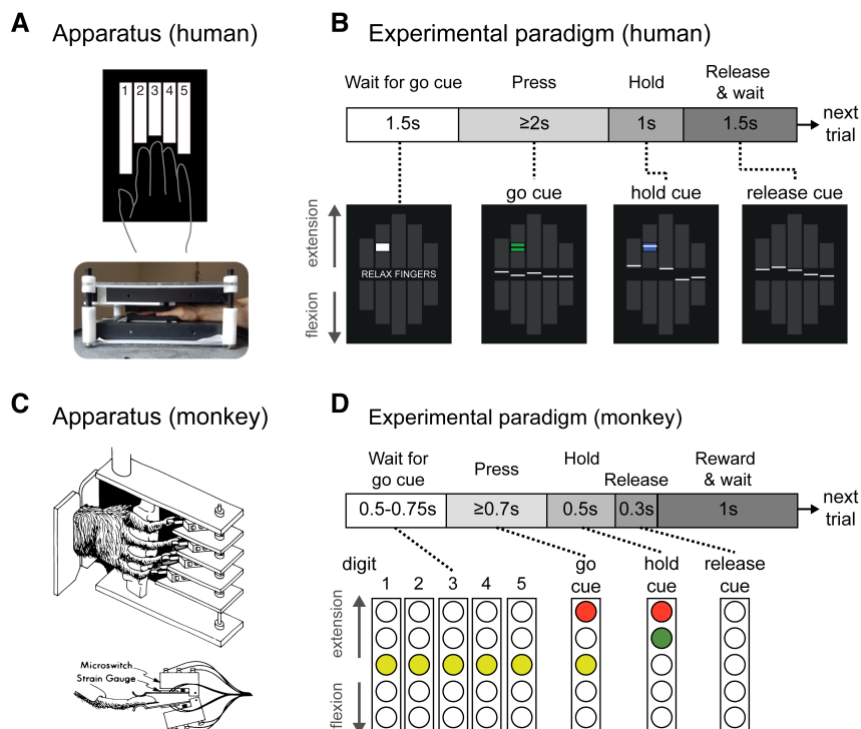


Figure 3.1: Experiment paradigms

(A) Human participants made isometric single finger presses in the flexion and extension directions on a custom-built keyboard. Each finger of the right hand was clamped between two keys, and each key was associated with a force transducer either above (keyboard on top of hand) or below (keyboard under the hand) the key to monitor forces applied in the flexion and extension directions, respectively.

(B) Schematic illustration for a single trial in the fMRI and EMG sessions, with associated visual feedback shown below. The white lines represent the produced force for each finger. Applying flexion to a finger key moved the associated line down (vice-versa for extension). The cue box (centred at target force) was initially presented as white at the trial start, and turned green to cue the participant to make the finger press (here, index finger extension). The box turned blue to instruct participants to maintain the current force. At the end of the press hold, the cue box disappeared and participants relaxed their hand.

(C) The monkey hand configuration and device (illustration from Schieber, 1991).

(D) Trial schematic for the monkey task. The columns represent 5 LED cues (one per finger) which instructed the monkey both what finger and what direction to press. The monkeys had up to 700ms from the onset of the go cue to press the cued finger in the cued direction. They were trained to hold the press for 500ms before relaxing the finger.

forces applied through the non-instructed fingers were, on average, 14.01% ($\pm 1.41\%$) of the forces applied by the instructed finger. During fMRI flexion, forces produced by non-instructed fingers was 20.51% ($\pm 1.49\%$) of the force produce by the instructed finger. Most enslaving occurred during presses of the middle, fourth, and little fingers, all of which are difficult to individuate (Schieber, 1991). Note, however, that the presence of enslaving does not compromise the main finding of our paper. To some degree, neural activity patterns related to flexion and extension of single fingers will always depend on the biomechanical coupling between fingers, either because the cortical activation patterns need to overcome that coupling, or because coupling does occur, which then influences the recurrent sensory input. Our main conclusions are based on comparisons between flexion and extension presses, and remain valid whether we study the actions of isolated fingers, or groups of fingers (see discussion).

3.3.3 fMRI acquisition and analysis

3.3.3.1 *Image acquisition*

We used high-field functional magnetic resonance imaging (fMRI, Siemens 7T Magnetom with a 32 channel head coil at Western University, London, Ontario, Canada) to measure the blood-oxygen-level dependent (BOLD) responses in human participants. For each participant, evoked-BOLD responses were measured for isometric, single-finger presses in the flexion and extension directions.

There were 2 repeats of each condition during each imaging run (5 fingers \times 2 directions \times 3 force levels \times 2 repeats = 60 trials). Trial order in each run was randomized. In addition, 5 rest conditions of 6000ms were randomly interspersed between trials within each run. Each run lasted approximately 390 seconds. Participants performed 8 such runs during the scanning session.

During each run, 270 functional images were obtained using a multiband 2D-echoplanar imaging sequence (GRAPPA, in-plane acceleration factor=2, multi-band factor=2, repetition time [TR]=1500ms, echo time [TE]=20ms, flip angle [FA]=45 deg). Per image, we acquired 32 interleaved slices (without gap) with isotropic voxel size of 1.5mm. The first 2 images in the sequence were discarded to allow magnetization to reach

equilibrium. To estimate magnetic field inhomogeneities, we acquired a gradient echo field map at the end of the scanning session. Finally, a T1-weighted anatomical scan was obtained using a magnetization-prepared rapid gradient echo sequence (MPRAGE) with a voxel size of 0.75mm isotropic (3D gradient echo sequence, TR=6000ms, 208 volumes).

3.3.3.2 *Image preprocessing and first-level analysis*

Functional images were first realigned to correct for head motion during the scanning session (3 translations: x,y,z; 3 rotations: pitch, roll, yaw), and co-registered to each participant's anatomical T1-image. Within this process, we used a B0 fieldmap to correct for image distortions arising from magnetic field inhomogeneities (Hutton et al., 2002). Due to the relatively short TR (1.5s), no slice-timing correction was applied. Nor was the data spatially smoothed or normalized to a standard template.

The minimally preprocessed data were then analysed using a general linear model (GLM; Friston et al., 1994) using SPM12 (fil.ion.ucl.ac.uk/spm/). Each of the finger-direction-force conditions were modeled with separate regressors per run, resulting in 30 regressors per run (30*8 runs = 320 task regressors), along with an intercept for each run. The regressor was a boxcar function that started at the presentation of the go-cue and lasted for the trial duration, spanning the press, hold, and release periods of each trial. The boxcar functions were convolved with a hemodynamic response function with a delayed onset of 1000ms and a post-stimulus undershoot at 7500ms. Given the low error rate, we did not exclude any trials from this analysis. To model the long-range temporal autocorrelations in the functional timeseries, we used the SPM FAST autocorrelation model with restricted-maximum likelihood estimation (see Arbuckle et al., 2019 for details). High-pass filtering was then achieved by temporally pre-whitening the functional data with this temporal autocorrelation estimate. This analysis resulted in one activation estimate (“beta-weights”) for each of the 30 conditions per run for each participant. For visual display (as in Figure 2) and further analysis, the beta values were divided by the root-mean-square error from the first-level GLM to yield a t-value per voxel for each condition in each run.

3.3.3.3 *Surface reconstruction and ROI definition*

Each participant's T1-image was used to reconstruct the pial and white-grey matter surfaces using Freesurfer (Fischl, Sereno, & Dale, 1999). Individual surfaces were aligned across participants and spherically registered to match a template atlas (Fischl, Sereno, Tootell, & Dale, 1999) using a sulcal-depth map and local curvature as minimization criteria. M1 was defined as a single region of interest (ROI) on the group surface using probabilistic cytoarchitectonic maps aligned to the template surface (Fischl et al., 2008). We defined M1 as being the surface nodes with the highest probability for Brodmann area 4 and who fell within 2.5cm above and below the hand knob anatomical landmark (Yousry et al., 1997). To avoid cross-contamination between M1 and S1 activities along the central sulcus, voxels with more than 25% of their volume in the grey matter on the opposite side of the central sulcus were excluded.

3.3.3.4 *Multivariate fMRI analysis*

We used the cross-validated squared Mahalanobis dissimilarity (i.e., crossnobis dissimilarity) to quantify differences between fMRI activity patterns for each pressing condition within each participant (Walther, et al., 2016; Diedrichsen, et al., 2020). Cross-validation ensures the dissimilarity estimates are unbiased, such that if two patterns differ only by measurement noise, the mean of the estimated dissimilarities would be zero. This also means that estimates can sometimes become negative (Diedrichsen, Provost, & Zareamoghaddam, 2016). Therefore, dissimilarities significantly larger than zero indicate that two patterns are reliably distinct.

The fMRI activity patterns were first-level GLM beta-weights for voxels within the M1 ROI mask. Analyses were conducted using functions from the RSA (Nili et al., 2014) and PCM (Diedrichsen, Yokoi, & Arbutckle, 2018) MATLAB toolboxes. The crossnobis dissimilarity d between the fMRI activity patterns (\mathbf{x}) for conditions i and j was calculated as

$$d_{i,j} = \frac{1}{M} \sum_m^M (\mathbf{x}_i - \mathbf{x}_j)_m^T \Sigma^{-1} (\mathbf{x}_i - \mathbf{x}_j)_{\sim m}$$

where the activity patterns from run m are multiplied with the activity patterns averaged over all runs except m ($\sim m$). Σ is the voxel-wise noise covariance matrix, estimated from the residuals of the GLM, and slightly regularized to ensure invertibility. Multivariate noise-normalization removes spatially correlated noise and yields generally more reliable dissimilarity estimates (Walther et al., 2016).

The dissimilarities are organized in a representational dissimilarity matrix (RDM). The RDM is a symmetric matrix (number of conditions x number of conditions in size) with off-diagonal values corresponding to the paired distance between two conditions. Values along the diagonal are zero, as there is no difference between a pattern paired with itself.

We calculated an RDM for the matched force conditions separately (i.e., the 1.5N and 2N presses, 10 conditions each), and then averaged the resulting RDMs within each participant. This yielded one RDM per participant containing the crossnobis dissimilarities between presses of the five fingers in either direction (10 conditions, 45 dissimilarity pairs).

3.3.3.5 *Estimating spatial tuning of fingers and direction*

We considered the possibility that fingers and directions could be encoded at different spatial scales in M1. We therefore estimated the spatial covariance of tuning for fingers and directions. Within each imaging run, we averaged the fMRI activity patterns (t-values) for each condition across the matched forces (1.5 and 2N). This yielded a vector of 10 activity values per voxel (one value per each finger per direction), which we refer to as an activity profile. We modeled the activity profile values ($y_{i,j}$) of each voxel and partition using three components:

$$y_{i,j} = f_i + d_j + q_{i,j}$$

where f_i is the main effect of finger i , d_j is the main effect of direction j , and $q_{i,j}$ is the finger x direction interaction effect. We used ordinary least-squares regression to estimate the finger and direction components. The residual from the regression was taken as estimate of the interaction component.

We first reconstructed the activity profiles using only the finger component (f), and then estimated the covariance of the finger activity profiles between voxel pairs in M1. These covariances were calculated in a cross-validated fashion: we averaged the reconstructed activity profiles for odd and even runs separately, and then then computed the covariance of the activity profile of different voxels across independent partitions of the data. Given that the estimates for all components contained some noise, normal covariance estimates are biased by the spatial structure of the noise. Cross-validation alleviates the influence of noise on (co-) variance estimation, as the average of the product of noise across odd and even runs is zero.

We then binned the covariances based on the spatial distance between each voxel pair and averaged the covariances within each bin. The first bin included only the cross-partition covariance between each voxel and itself (i.e., the cross-validated estimate of the voxel variances). The second bin contained the covariances between immediately and diagonally neighbouring voxels (1.5 to 2.6mm), the third bin the second layer of direct and diagonally neighbouring voxels (>2.6 to 5.2mm), and so on, up to a total distance of 20.8mm. Finally, we normalized the binned covariances by the cross-validated voxel variances (value of the first bin) to obtain an estimate of the spatial autocorrelation function (ACF) for fingers in M1.

We used the same procedure to estimate the ACF for direction. Importantly, we included both the direction (d) and the finger x direction interaction (q) components in the activity profile reconstruction. We included the interaction component as we hypothesized that the tuning of voxels to flexion and extension patterns would be different across fingers.

Finally, we estimated the smoothness of the finger and direction ACFs (Diedrichsen, Ridgway, Friston, & Wiestler, 2011). To do this, we fitted a function that decayed exponentially with the square of the distance (δ) between voxels (v):

$$ACF(v_x, v_{x+\delta}) = \exp\left(-\frac{\delta^2}{2s^2}\right)$$

Here, s is the standard deviation of the ACF. If neighbouring voxels are relatively independent (i.e., low covariance), the value of s will be small. While we can use s to express the smoothness of the ACF, the smoothness can also be expressed as the full-width-half-maximum (FWHM) of the Gaussian smoothing kernel that – when applied to spatially independent data – would yield the same ACF. The standard deviation of this Gaussian kernel is $\sqrt{1/2s}$, and the FWHM is calculated as:

$$FWHM = 2s\sqrt{\log(2)}$$

We applied this approach to the reconstructed finger and direction activity profiles separately to estimate the FWHM of fingers and direction M1. The goodness of fit (evaluated with R^2) of the fitted exponential decays were both high (mean R^2 of finger ACF=0.960 \pm 0.008 sem, mean R^2 of direction ACF=0.908 \pm 0.020 sem). Although there was a significant difference between the finger and direction model R^2 (two-sided paired t-test: $t_s=2.412$, $p=0.0424$), the mean difference was quite small (0.052 \pm 0.021sem).

3.3.3.6 Centre-of-Gravity (CoG) Analysis

We analysed the activity patterns to determine if there were significant differences in the spatial arrangement of finger flexion and extension, as proposed by Huber et al. (2020). To ensure our analysis closely matched this previous report, we restricted the CoG analysis to include only surface nodes from Brodmann area 4a, as based on the probabilistic atlas (Fischl et al., 2008). We also restricted the analysis to the hand region by selecting only vertices within 1.5cm of the hand knob anatomical landmark. On the flattened activity maps for each finger, we then calculated the centre-of-gravity (CoG) of each map as the average spatial location (\hat{x} , \hat{y}) of each surface node (i), weighted by its respective t -value (t):

$$\hat{x} = \frac{\sum_{i=1}^P x_i t_i}{\sum_{i=1}^P t_i}$$

$$\hat{y} = \frac{\sum_{i=1}^P y_i t_i}{\sum_{i=1}^P t_i}$$

In the above calculations, we set negative t -values equal to zero, thereby focusing our spatial analysis on regions that showed activity increases. We used a two-factor repeated-measures MANOVA to test for significant differences between the measured CoGs for different fingers and directions. To summarize the structure of the spatial arrangement, we calculated the pairwise Euclidean distances between the CoG coordinates for each condition, and arranged them into an RDM.

3.3.4 EMG recording and analysis

3.3.4.1 *EMG recordings and preprocessing*

In a separate session, we recorded hand and forearm muscle activity to ensure participants performed the task as instructed. During the EMG session, participants were seated upright, whereas during the fMRI session participants lay prone in the scanner. In both sessions, however, we ensured that the arm was in a relaxed position, the palm of the hand was supported by the device, the wrist slightly extended, and the elbow joint slightly bend. Thus, wrist and forearm posture, both known to influence muscle activity during finger movements (Beringer, et al., 2020; Mogk & Keir, 2003) were matched across the two sessions. Participants' skin was cleaned with rubbing alcohol. Surface EMG of distal muscles of the hand were recorded with self-adhering Ag/AgCl cloth electrodes (H59P-127 repositionable monitoring electrodes, Kendall, Mansfield, Massachusetts, USA). Electrodes were cut and positioned in line with a muscle in a bipolar configuration with an approximate 1cm inter-electrode distance. Surface EMG of proximal limb muscles were recorded with surface electrodes (Delsys Bagnoli-8 system with DE-2.1 sensors). The contacts were coated with a conductive gel. Ground electrodes were placed on the ulna at the wrist and elbow. The signal from each electrode was sampled at 2000Hz, de-meaned, rectified, and low-pass filtered (fourth order butterworth filter, $f_c=40\text{Hz}$).

3.3.4.2 *Multivariate EMG analysis*

We used the crossnobis dissimilarity to quantify differences between patterns of muscle activities for each movement condition, similar to the fMRI analysis. This metric is invariant to scaling of the EMG signals from each electrode, and has been established in

previous work (Ejaz, Hamada, & Diedrichsen, 2015). Briefly, we first calculated the average square-root EMG activity for each electrode and trial by averaging over the press and hold time windows (mean window= 1800ms, up to a max window of 3000ms). We then subtracted the mean value for each electrode across conditions for each run independently to remove any drifts in the signal. These values were then divided by the standard deviation of that electrode across trials and conditions to avoid arbitrary scaling. Finally, we calculated the crossnobis dissimilarity between pairs of EMG activity patterns for different conditions across runs.

3.3.5 Experimental design of monkey finger individuation task

The behavioural task performed by two male *Macaca mulatta* monkeys (monkeys C and G) has been described previously (Schieber, 1991; Schieber & Rivlis, 2007). Briefly, the monkeys were trained to perform cued single finger flexion and extension presses. Each monkey sat in a primate chair and, similar to the human device described above, their right hand was clamped in a device that separated each finger into a different slot (Fig. 3.1C). Each slot was comprised of two microswitches (one in the flexion direction and one in the extension direction). One switch was closed by flexing the finger, the other by extending the finger. The absolute degree of movement required to close either switch was minimal (a few millimeters), and therefore the force required to make and hold a successful press was small- similar to the human finger individuation task. Therefore, like the fMRI task behaviour, these finger movements are very close to isometric presses.

A series of LED instructions were presented to the monkey during each trial (Fig. 3.1D). A successful trial occurred when the monkey pressed the cued finger in the cued direction without closing any other switch. Similar to our human experiment design, the monkeys were trained to hold the cued switch closed for 500ms, before relaxing the finger (Fig. 3.1D). At the end of a successful trail, the monkey received a water reward. The monkey's wrist was also clamped in this device, and some trials required the monkey to flex or extend the wrist. Wrist trials were not included in the current analysis. Flexion and extension trials of each finger and wrist were pseudorandomly ordered. In the case of a behavioural error, trials were repeated until successful. Therefore, we excluded all trials

with an error and also the successful trials that followed error trials to avoid potential changes in the baseline firing rate of the recorded neuron.

In contrast to the human task, the required force level for the monkeys was the same for all trials – therefore, they did not receive continuous visual feedback about the force produced. Instead, they received small tactile feedback when the switch closed, a feature that was absent from the human task. In spite of these small differences in feedback, the task requirements were well matched across species: Both monkey and humans were required to produce low, well-controlled forces with a single finger, while keeping forces on the non-instructed fingers minimal, either to avoid unwanted switch-closure, or excessive movement of the associated visual feedback.

3.3.6 Analysis of single cell spiking data

3.3.6.1 *Spike rate calculation*

Single cells were isolated and spike times were recorded while monkeys performed the finger individuation task. The details of the recordings are reported previously (Poliakov & Schieber, 1999). Each trial was labeled with a series of behavioural markers, indicating the time of trial onset, presentation of condition cue, switch closure, and reward onset. For the spike rate traces plotted in Figure 3.4, we calculated the spike rate per 10ms bin, aligned to press onset, and smoothed the binned rates with a Gaussian kernel (FWHM=50ms). For the dissimilarity analysis (see below), we calculated the average spike rate over time per trial starting at go cue onset (when the monkey was instructed as to which finger and direction to press) until the end of the hold phase (500ms after switch closure). This time window encompassed a short period of time prior to the start of the finger press and the entire hold duration of the press (Monkey C: mean window= 739ms; Monkey G: mean window=773ms).

3.3.6.2 *Multivariate spiking analysis*

Similar to the human fMRI and EMG analyses, we computed crossnobis dissimilarities between spiking patterns for different conditions within each monkey. To cross-validate the estimated distances, we restricted our analysis to include cells for which we had at

least two successful trials for each finger in both directions. This criteria yielded 44801 trials from 238 cells in monkey C (median number of trials per cell=168, median number of trials per condition per cell=19) and 5535 trials from 45 cells in monkey G (median number of trials per cell=115, median number of trials per condition per cell=12). After calculating the average spike rates, we arranged the spike rates into vectors per condition (Fig. 3.4B). In order to account for the Poisson-like increase of variability with increasing mean firing rates, we applied the square-root transform to the average firing rates (Yu et al., 2009).

For each cell per condition, we randomly split the square-root spike rates from different trials into one of two partitions. The random splits contained approximately the same number of trials, which ensured that each condition was approximately equally represented in each partition. We then averaged the spike rates within each partition. This yielded two independent sets of spiking patterns per monkey (10 patterns- 5 fingers x 2 directions). Per partition, we normalized each neuron's spike pattern by dividing by the neuron's max rate across conditions, and then re-weighted the normalized spike rates per cell according to the number of trials per cell (cells with more trials were up-weighted, vice versa for cells with fewer trials). Finally, we calculated pairwise cross-validated Euclidean distances between the two sets of patterns. We repeated this RDM calculation procedure 1000x per monkey, each time using a different random partitioning of the data. We then averaged the RDMs across iterations to yield one RDM estimate per monkey. We note that results were not dependent on the normalization we chose- results were qualitatively consistent when using raw firing rates, z-scoring the firing rates, not applying trial re-weighting, and various combinations of these approaches.

3.3.7 Kinematic finger model RDM

As in Ejaz et al. (2015), we used the statistics of naturalistic hand movements to predict the relative similarity of single finger representations in M1. In the text we refer to this model as the kinematic model. To construct the kinematic model RDM, we used hand movement statistics from an independent study in which 6 male participants wore a cloth glove imbedded with motion sensory (CyberGlove, Virtual Technologies) while they performed everyday activities (Ingram et al., 2008). These statistics included the

velocities about joint angles specific to each of the five fingers of the participants' right hands. Positive velocities indicated finger flexion, and negative velocities indicated finger extension.

Because the movement in our finger pressing task was restricted to movements about the metacarpal (MCP) joint of each finger, we used the MCP joint velocities to predict cortical M1 finger similarity. First, we split the data for each joint velocity into two vectors: one for flexion and one for extension, taking the absolute of the velocities in this process. During periods of finger flexion, we set the extension velocity to zero, and vice versa. This resulted in 10 velocity vectors (5 fingers x 2 directions). Then, to account for differences in scaling, we normalized each velocity vector to a length of 1. Finally, we calculated the dissimilarities between pairs of these processed velocity vectors. We averaged these RDMs across the six participants in the natural statistics dataset, yielding one kinematic model RDM.

3.3.8 Experimental design and statistical analysis

3.3.8.1 *Statistical analysis of dissimilarities*

We summarized the RDMs by classifying dissimilarities into finger-specific and direction-specific dissimilarities for each participant and dataset. Finger-specific dissimilarities were the dissimilarities between conditions where different fingers were pressed in the same direction (10 pairs for flexion, 10 pairs for extension). Direction-specific dissimilarities were the dissimilarities between conditions where the same finger was pressed in different directions (5 pairs total). Within each category, dissimilarities were averaged. For the human data, we used one-sided, one-sample t-tests to test if mean finger and direction dissimilarities were greater than zero. To compare between the average finger and direction dissimilarities, we used two-sided paired t-tests. We report the mean and standard error of the dissimilarities where appropriate in the text.

3.3.8.2 *Statistical analysis of RDM correlations*

Pearson's correlations between the vectorized upper-triangular elements of the RDMs were used to compare different RDMs (Ejaz et al., 2015). To calculate the stability of

RDMs, we calculated the Pearson's correlations between all possible pairs of the participants' RDMs. This yielded 36 correlations (one per unique participant pair). We Fisher-Z transformed these correlations and calculated the mean and standard error. We used these values to calculate the lower and upper bounds of the 95% confidence interval, assuming normality. Finally, the mean and confidence bounds were transformed back to correlations. We report these values in the text as $r = \text{mean} [\text{lower bound} - \text{upper bound}]$. The same method was applied to correlations between measured RDMs and model predictions. Note that because we used a within-subject design, the muscle model predictions were specific to each human participant. In contrast, the kinematic model prediction was the same for each participant because data for this model was obtained from an independent study. Paired t-tests were performed on Fisher-z transformed correlations to compare fits between models.

3.3.8.3 *Estimating noise ceiling for RDM model fits*

Since the dissimilarities between fMRI patterns can only be estimated with noise, even a perfect model fit would not result in a perfect correlation with the RDM of each participant. Therefore, we estimated the noise ceiling, which places bounds on the expected model correlations if the model is a perfect fit. We first calculated the average correlation of each participant's RDM with the group mean RDM (Nili et al., 2014), treating the mean RDM as the perfect model. The resulting average correlation is an overestimate of the best possible fit, as each RDM is correlated with a mean that includes that RDM (and hence also the measurement error of that RDM). To then estimate a lower bound, we calculated the correlation between a participant's RDM and the group mean RDM in which that individual was removed.

3.4 Results

3.4.1 M1 fMRI activity patterns differ strongly for different fingers, not for direction

We measured activity patterns evoked in M1 in human participants ($n=9$) while they performed a near-isometric finger flexion-extension task in a 7T MRI scanner. Participants' right hands were clamped in a device that had force transducers mounted

both above (extension) and below (flexion) each finger (Fig. 3.1A) to record forces produced at the distal phalanges. The device limited the overall degree of movement to a few millimeters, thereby making the task near-isometric. On each trial, participants were cued to press a single finger in one direction, while keeping the other fingers as relaxed as possible (Fig. 3.1B). They had to reach the required force level, hold it for 1 second, and then simply relax their hand to let the force passively return to baseline. This aspect of the task instruction was critical to ensure that participants did not activate the antagonist muscles during release.

Figure 3.2 shows the activity patterns measured in left M1 (contralateral to movement) for three participants during right-handed finger presses at 2N. As previously observed (Ejaz et al., 2015), the activity patterns did not consist of focal regions of activity dedicated to each finger. Rather, the spatial patterns were complex and involved multiple overlapping regions within the M1 hand area. Furthermore, the inter-subject variability in the spatial organization of these patterns was considerable.

One common observation across all participants, however, was that the activity patterns were different between different fingers (e.g., index flexion vs. fourth flexion), but rather similar for flexion and extension of the same finger (e.g., index flexion vs. index extension). We used representational similarity analysis (RSA) to quantify these observations by calculating a measure of dissimilarity (crossnobis dissimilarity, see Methods) between each pair of fMRI patterns. Large dissimilarity values indicate that the two patterns are quite distinct with little overlap. A value of zero indicates that the two patterns are identical and only differ by noise. We restricted the analysis to conditions with matched force levels across flexion and extension. The group-averaged representational dissimilarity matrix (RDM) is shown in figure 3.3A. Both within the finger flexion and extension conditions, there was a characteristic structure with the thumb activity pattern being the most distinct and neighbouring fingers tending to have more similar activity patterns. Across directions, activity patterns evoked by pressing the same finger in different directions were the most similar. This representational structure was quite stable across participants (average inter-participant Pearson's $r=0.790$, 95% CI: [0.754-0.820]).

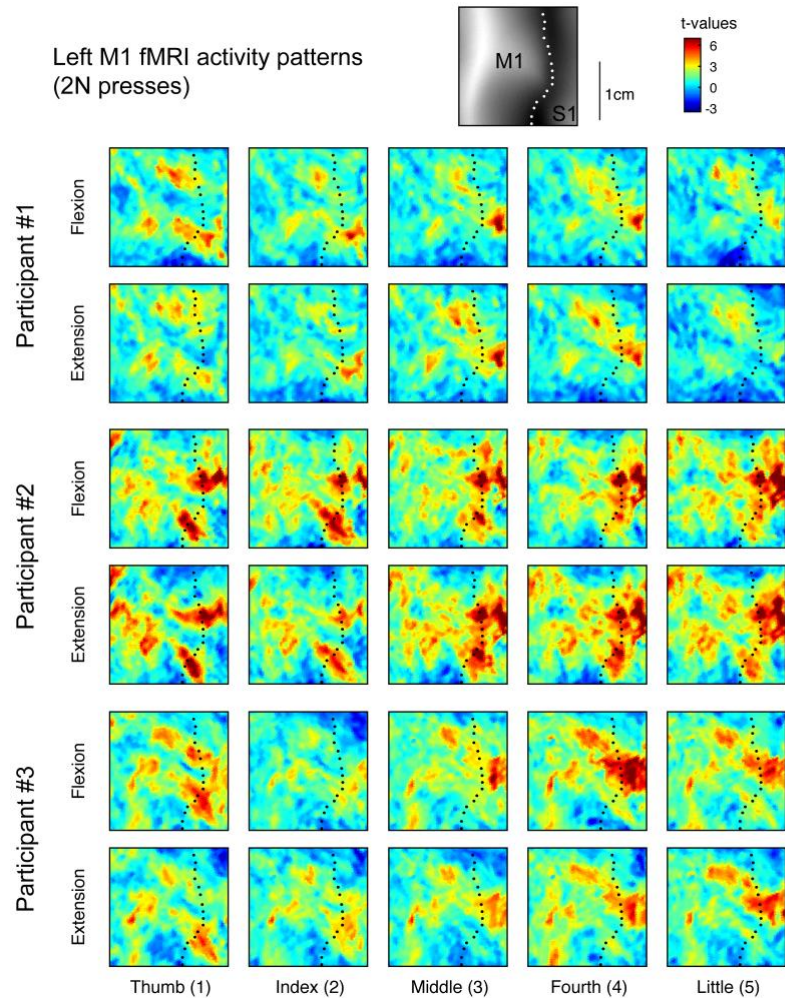


Figure 3.2: fMRI activity patterns for finger flexion and extension in human M1

Evoked fMRI activity maps (t -values) for three participants for each of the 5 fingers pressing in the extension and flexion directions at 2N. Results were normalized to a surface-based atlas. Maps are shown in the hand-knob region of the left (contralateral) hemisphere. The black dotted line shows the fundus of the central sulcus. The upper inset shows the average sulcal depth.

To obtain predictions for flexion and extension movements, we needed to adapt the natural usage model, proposed by Ejaz et al. (2015). This model used kinematic finger data, specifically the joint-angle velocities of the metacarpal (MCP) joints, recorded while subjects participated in their normal, every-day tasks (data from Ingram et al., 2008).

Fingers were predicted to have more similar representations if their movement velocities, across flexion and extension, were positively correlated. For the current experiment, we split the data into periods of finger flexion and finger extension (see methods), resulting in 10 time series, and calculated the correlation between them (after taking the absolute value).

The estimated kinematic RDM (Fig. 3.3B) showed similar structures within flexion and extension movements. The thumb was the most distinct compared to the other fingers, and for the remaining fingers there was a clear similarity structure with neighbouring fingers more similar than non-neighbouring. This structure very closely mirrored those found for fMRI activity patterns: flexion and extension fMRI RDMs correlated strongly with the corresponding kinematic models for flexion ($r=0.727$ [0.635-0.800]) and extension ($r=0.797$ [0.684-0.873]) RDMs (Fig. 3.3C, white). Compared to the noise ceiling (grey bar in Fig 3C, which reflects the best possible model fit given measurement noise: see methods) the natural use model accounted for 79.9% and 84.9% of the variance in the flexion and extension fMRI RDMs, respectively.

In contrast, the kinematic model completely failed to predict the relationships between activity patterns for flexion and extension. Because flexion and extension of the same finger can never co-occur, the kinematic model predicts that the movements are associated with quite distinct cortical activity patterns. The measured fMRI patterns, however, were rather similar for these two actions. As a result, the full kinematic model was not a good fit to the full fMRI RDM ($r=0.086$ [0.038-0.133]), much below the noise ceiling ($r=0.875$ [0.822-0.913]).

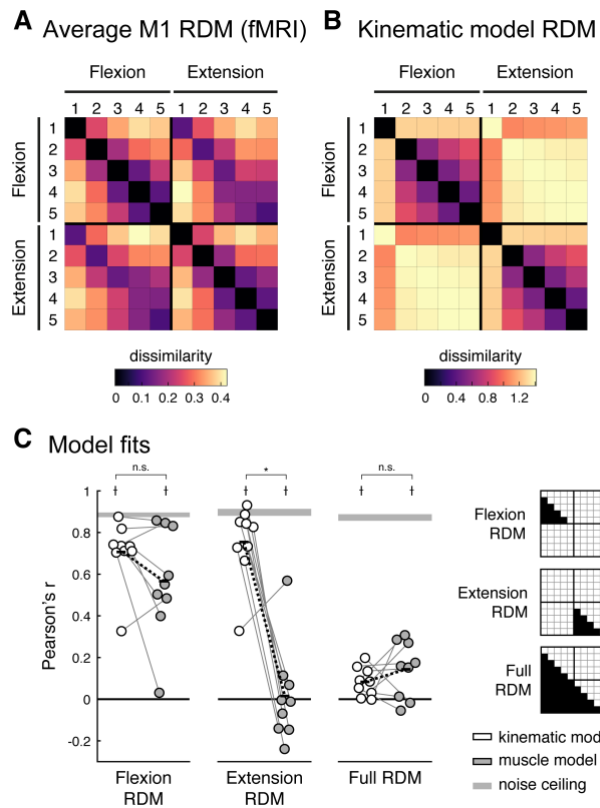


Figure 3.3: Representational structure of fingers and direction in human M1

(A) Group average of the fMRI representational dissimilarity matrix (RDM).

(B) Predicted RDM from the kinematic model. To aid visual inspection, the values of the RDMs in A and B are plotted as the square-root of the dissimilarities. All statistical analyses of the RDMs are done on squared distances.

(C) Model fits (Pearson's r) of the kinematic (white) and muscle (grey) models to the M1 RDM for flexion, extension, and the full RDMs (the indices for each RDM are shown on the right). The muscle model was specific to each participant and was estimated from the EMG data. The grey bars denote noise ceilings (theoretically the best possible fits). Each dot reflects one participant, and thin grey lines connect fits of each model to the same participant. Black bars denote the means, and black dashed lines denoted the mean paired difference. *significant differences between model fits (one-sided paired t-test, $p < 0.05$); † significantly lower than the noise ceiling (two-sided paired t-test, $p < 0.05$); n.s. not significant ($p > 0.05$).

Thus, although the statistics of movement co-occurrence was a good predictor for representational similarity between the activity patterns for different fingers (i.e., within flexion or extension), this simple model failed to predict the relative organization of the patterns for flexion and extension of the same finger. Even though flexion and extension of the same finger cannot co-occur, their fMRI activity patterns were highly similar. In the remainder of the paper, we explore a number of possible explanations for this finding and propose a candidate model of the organization.

3.4.2 Similarities of cortical representations for presses in different directions cannot be explained by the patterns of muscle activity

We first considered the possibility that the structure of similarity between flexion and extension presses can be explained by the patterns of muscle activity required by these movements. Specifically, it is possible that participants co-contracted both agonist and antagonist muscles, or that they activated the antagonistic muscles when returning to baseline. Given the temporally sluggish nature of the blood-oxygen level-dependent (BOLD) signal measured with fMRI, either behaviour could cause the cortical activity patterns evoked during flexion to resemble activity patterns during extension (and vice versa). Therefore, we conducted a control experiment with the same participants outside the MR scanner, during which we recorded surface electromyography (EMG) from 14 sites of the hand and forearm in the participants (Fig. 3.4A), while they performed the same isometric finger flexion-extension task as in the fMRI session. Performance on the task was comparable to that during the fMRI scan.

As an example, the participant-averaged EMG data from an electrode placed above the abductor digiti minimi (ADM) muscle (Fig. 3.4B) showed that the ADM muscle was recruited only during the flexion of the little finger. During extension of the same finger, the muscle was silent, both during hold and release. In general, we found very little evidence for co-contraction of the antagonist muscle.

For a quantitative analysis, we averaged the muscle activity from the time of the go-cue to the end of the hold phase. The EMG patterns averaged across participants (Fig. 3.4C)

already allow for two observations. First, the muscle activities for the same movement at different force levels were very similar and increased with increasing force. The average correlation across force levels for each finger-direction combination was high, indicating the same muscles were consistently recruited to perform the same finger press across different force levels (within participant correlations: $r=0.860$ [0.808-0.898]). Second, quite distinct muscle groups were recruited to produce forces with the same finger in different directions. The average correlation between the pattern of muscle activity recruited to press the same finger in different directions was low (within participant correlations: $r=0.244$ [0.150-0.334]).

We then derived a muscle-based RDM by calculating the crossnobis dissimilarity between normalized activity patterns for each condition. As for the fMRI analysis, we included the patterns for the matched force conditions only. The group averaged matrix RDM (Fig. 3.4D) was only moderately stable across participants (average inter-participant Pearson's $r=0.480$ [0.379-0.570]), likely reflecting the fact that there was some degree of inter-individual variation in electrode placement.

We tested to what degree the patterns of muscle activity, specific to each participant, could explain the cortical similarity structure between individual finger movements within the flexion or extension directions. For the flexion direction, the fit of the muscle model ($r=0.611$ [0.408-0.757]) was lower than that for the kinematic model in 6 out of 9 participants (Fig. 3.3C), but the difference did not reach statistical significance (one-sided paired t-test kinematic>muscle: $t_8=1.775$, $p=0.0569$). For the extension direction, the muscle model fit substantially worse ($r=0.020$ [-0.147-0.187]), significantly less than the kinematic model (one-sided paired t-test kinematic>muscle: $t_8=5.588$, $p=2.59e-4$). This generally confirms the results reported in Ejaz et al. (2015) that the relative similarities of M1 finger flexion activity patterns is better explained by the correlation structure of everyday movements than the correlation structure of the required muscle activity patterns. Our new results now show that this observation generalized also to extension movements.

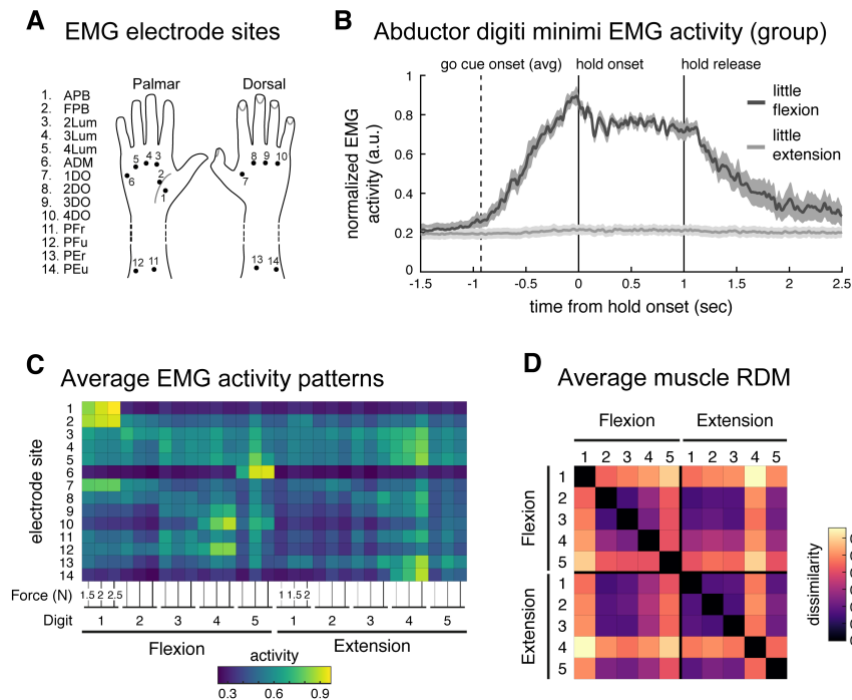


Figure 3.4: Quantifying similarity of muscle activity patterns during finger flexion and extension

(A) Fourteen surface electrode sites. APB, abductor pollicis brevis; FPB, flexor pollicis brevis; 2-4Lum, lumbricals; ADM, abductor digiti minimi; 1-4DO, interossei dorsales; PFr/u, flexor digitorum profundus (radial/ulnar regions); PEr/u, extensor digitorum profundus (radial/ulnar)

(B) Group averaged normalized EMG (normalized, per participant, to peak activity from this electrode across trials) from the ADM muscle (electrode #6) during 2N little finger (5) flexion (dark grey) and extension (light grey) trials, aligned to hold onset (0s). During extension movement (light grey trace, >1000ms), this flexor muscle was not recruited. Shaded areas reflect standard error of the mean. Traces were smoothed with a gaussian kernel (FWHM=25ms).

(C) Average muscle activity across participants, normalized by peak activation across conditions (per participant), recorded from the 14 electrode sites during the flexion extension task. Each condition was measured under 3 force conditions.

(D) Group average representational dissimilarity matrix (RDM) of the muscle activity patterns. As in figure 2, the RDM is plotted as square-root dissimilarities to aid visual inspection.

Critically, however, the muscle activity model did not provide a good explanation for the similarity between flexion and extension patterns. The fit for the full muscle model ($r=0.146$ [0.055-0.235]) was as poor as for the kinematic model (two-sided paired t-test muscle vs. kinematic: $t_8=1.082$, $p=0.3108$) and significantly below the noise ceiling (two-sided paired t-test noise ceiling vs. muscle: $t_8=12.701$, $p=1.39e-6$). Thus, neither the co-occurrence of movements, nor the pattern of muscle activities can explain the high similarity of activity patterns for finger flexion and extension in M1.

3.4.3 M1 spiking output differs equally for fingers and direction

To what degree is the high similarity between flexion and extension patterns a function of fMRI as the measurement modality? To approach this question, we analysed the spiking activity of output neurons in M1 during an equivalent single-finger individuation task in two trained non-human primates (*Macaca mulatta*, data from Schieber & Rivlis, 2005 & 2007). To facilitate this, we had designed the behavioural task for the human fMRI experiment to closely match the task for the monkeys, such that we could make strong comparisons across species and measurement modalities. Figure 3.5A shows the condition averaged firing rate traces from a single neuron from this data set. This neuron displayed strong preference (increased firing rates) for flexion of the middle finger and extension of the index finger. As previously reported (Schieber & Hibbard, 1993), the population of M1 neurons demonstrated complex, heterogeneous tuning across fingers and directions.

To compare the representational structure from spiking data to that obtained with fMRI, we calculated the mean firing rate for each neuron from the go-cue onset to the end of the hold phase during each trial. We then calculated dissimilarities between the population responses for different conditions (see Methods), similar to the analysis of the human EMG and fMRI data. The average RDM is shown in Figure 3.5C. Similar to the structure of representations in human M1, the thumb activity patterns for both directions were the most distinct, and neighbouring fingers had more similar activity patterns. In contrast to the fMRI data, however, the spiking patterns for flexion and extension of the same finger were quite distinct.

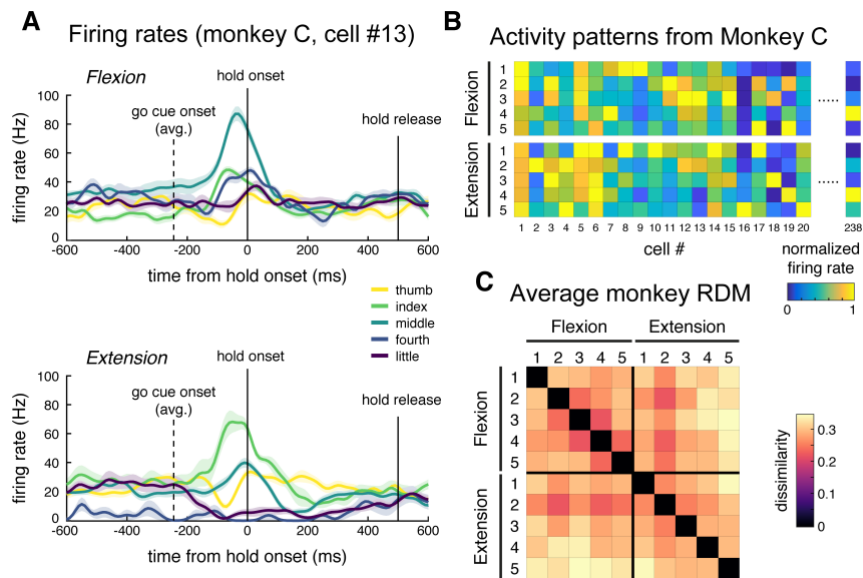


Figure 3.5: Analysis of M1 spiking activity during monkey single finger flexion and extension

(A) Trial averaged firing rates from one cell (monkey C). Traces are aligned to press onset (0s). This cell demonstrates selective tuning to middle finger flexion and index finger extension. Firing rates were calculated for 10ms bins and smoothed with a gaussian kernel (FWHM=50ms). Shaded areas reflect standard error across trials.

(B) Averaged firing rates for a subset of cells from monkey C, arranged by condition. Cell #13 is plotted in A. Firing rates are normalized to the peak rate per cell.

(C) Average monkey RDM (square-root dissimilarities).

To quantify this observation, we averaged dissimilarities between different fingers pressing in the same direction (finger-specific) and the same finger pressing in different directions (direction-specific). The finger and direction-specific dissimilarities were close in magnitude for both monkeys (Fig. 3.6A). Also, the human EMG patterns had roughly matched direction and finger-specific dissimilarities (Fig. 3.6B). In contrast, the same analysis on the human fMRI data showed a clear and significant difference between these two kinds of dissimilarities (Fig. 3.6C).

For a statistical comparison, we then calculated the ratio between dissimilarities between different directions and dissimilarities between different fingers (Fig. 3.6D). The fMRI ratio was significantly lower than 1 (mean ratio=0.298 \pm 0.071; one-sided one-sample t-test: $t_8=-9.858$, $p=4.72e-6$), indicating stronger representation of fingers compared to direction. In contrast, both the spiking patterns (monkey C ratio=1.173, monkey G ratio=1.025) and the human muscle patterns (mean ratio=0.984 \pm 0.051) differed similarly for different fingers and different directions, with the muscle ratios being significantly larger than those for human fMRI (two-sided paired t-test: $t_8=9.733$, $p=1.04e-5$). Thus, we found a clear difference between the structure of fMRI patterns and the structures of spiking and muscle activity patterns.

We suggest that this difference is informative about the general organization of finger flexion and extension movements in M1. The discrepancy between the two measurement modalities can likely be attributed to two (non-mutually exclusive) differences between fMRI and electrophysiology. First, the fMRI signal is dominated by excitatory inputs and local synaptic signaling, and only partly reflects the spiking activity of output neurons (Logothetis et al., 2001). Therefore, the overlapping fMRI activity patterns for flexion and extension might reflect similar inputs and shared local processes within these cortical areas, while the output spiking of these two population remains quite distinct in order to produce the different patterns of muscle activity required for fine finger control.

Second, fMRI samples a proxy of neuronal activity in a coarse manner, averaging across \sim 200,000 cortical neurons per mm³ in M1 (Young, Collins, & Kaas, 2013). Thus, even high-resolution fMRI is biased to functional organization at a coarse spatial scale

Figure 3.6: Comparing strength of finger and direction representations across datasets

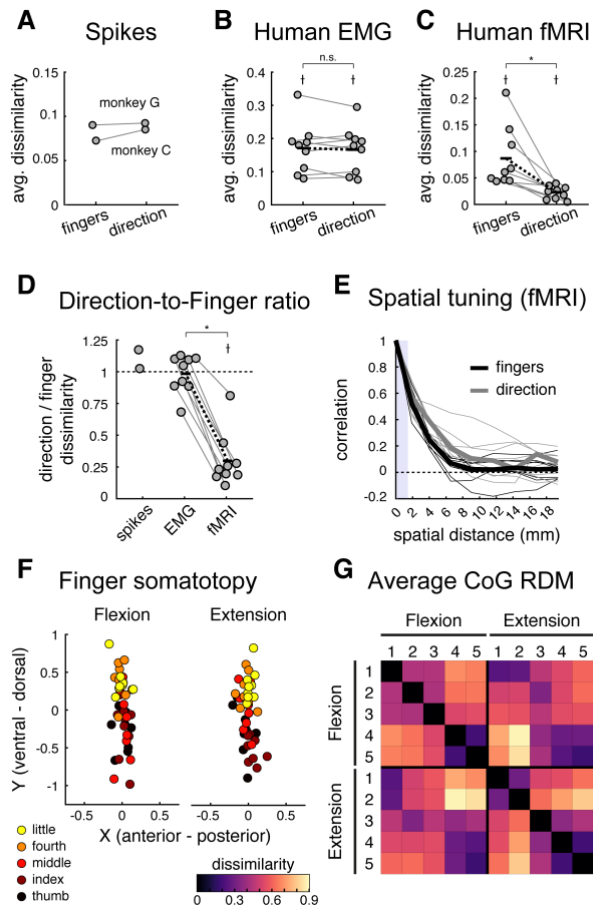
The average finger and direction-specific dissimilarities for the spiking (A), human EMG (B), and human fMRI (C) datasets. Each dot denotes one participant, and lines connect dots from the same participants. Black bars denote the means, and black dashed lines reflect the mean paired differences. † dissimilarities significantly larger than zero (one-sided t-test, $p < 0.05$). *significant difference between finger and direction dissimilarities (two-sided paired t-test, $p < 0.05$).

(D) The ratio of the direction-to-finger dissimilarities for each dataset. Values < 1 indicate stronger finger representation. † dissimilarities significantly lower than one (one-sided t-test, $p < 0.05$). *significant differences between dissimilarity ratios (two-sided paired t-test, $p < 0.05$).

(E) Estimated spatial autocorrelations of finger (black) and direction (grey) pattern components in human M1, plotted as a function of spatial distance between voxels. No significant difference was observed between finger and direction tuning in M1. The thick lines denote the median spatial autocorrelation functions, and small lines are drawn for each participant for each pattern component. The vertical shaded bar denotes the distance between voxel size, for which correlations can be induced by motion correction.

(F) Centre-of-gravity (CoG) of activation elicited by single finger presses in the flexion or extension direction for each participant. CoGs were aligned across participants prior to plotting by subtracting the centre of the informative region within each participant (i.e the mean CoG across all conditions). A somatotopic gradient for finger flexion and extension in Brodmann area 4a is visible with the thumb being more ventral and the little finger more dorsal.

(G) Group average RDM of the paired Euclidean distance between condition CoGs.



(Kriegeskorte & Diedrichsen, 2016), and so our results could be caused by an organization where neurons tuned to different movement directions for the same finger (or combination of fingers) are clustered together, while neurons that control different fingers or finger combinations are more spatially separated.

3.4.4 Spatial organization of finger- and direction-related fMRI patterns

To investigate the second explanation directly, we attempted to determine whether the activity patterns associated with different fingers were organized on a coarser spatial scale than the patterns associated with flexion and extension of a given finger. Using the fMRI data, we calculated the covariance of the finger-specific and direction-specific activations for each pair of voxels within M1, and binned these covariances according to the spatial distance between voxel pairs (see Methods). If direction is encoded at a finer spatial scale than fingers, we would expect finger effects to be correlated over larger spatial distances.

In contrast to this prediction, the spatial correlation functions for fingers and direction were quite similar (Fig. 3.6E). We estimated the full-width at half-maximum (FWHM) of the spatial autocorrelation functions. To account for outliers, we evaluated the median FWHMs. The median FWHM of the finger spatial kernel in M1 was 3.22mm (mean=3.44mm \pm 0.24 sem), comparable to previous reports (Diedrichsen et al., 2011; Wiestler, McGonigle, & Diedrichsen, 2011). The median FWHM of the direction spatial kernel in M1 was 4.65mm (mean=4.77mm \pm 0.84 sem), and there was no significant difference between the two (two-sided paired Wilcoxon signed-rank test, finger vs. direction: $W=11$, $p=0.2031$; two-sided paired t-test finger vs. direction: $t_8=-1.417$, $p=0.1942$). Therefore, we did not find any direct empirical support for the idea that differences between flexion and extension patterns are organized at a finer spatial scale than differences between fingers. However, our analysis was itself limited by the spatial resolution of 7T fMRI, such that we cannot rule out the possibility that subpopulations for different directions are interdigitated at a sub-voxel scale.

Additionally, we did not find evidence of a substantial spatial separation of flexion vs. extension movements, as was suggested by Huber et al. (2020). These authors observed two sets of digit maps in Brodmann area 4a, with one set being more activated for whole hand grasping, and the other more activated for whole hand retraction movements. From this, the authors suggested that each individual finger map has a preferential function role in guiding flexion and extension movements. To test this idea with our fMRI data, we calculated the centre-of-gravity (CoG) of the activity maps for each finger pressing in the flexion and extension directions in Brodmann area 4a (see Methods).

As shown in figure 3.6F, both finger flexion and extension CoGs revealed the expected overall somatotopic gradient, with thumb movements activating more ventrolateral areas and the little finger activating more dorsomedial areas in 4a (2-factor repeated-measures MANOVA, finger factor: Wilks' $\Lambda_{(4,32)}=0.28$, $p=2.2075e-6$). However, there was no significant difference in these digit maps across flexion and extension movements (2-factor repeated-measures MANOVA, direction factor: Wilks' $\Lambda_{(1,8)}=0.88$, $p=0.6427$; finger x direction interaction: Wilks' $\Lambda_{(4,32)}=0.65$, $p=0.0793$). We then calculated the pairwise Euclidean distances between the condition CoGs (Fig. 3.6G) and compared the between and within finger distances, as done previously. Replicating the results from the fMRI RSA analysis, we found that pressing different fingers resulted in more spatially distinct activation patterns compared to pressing the same finger in different directions (mean ratio= 0.67 ± 0.04 ; one-sided one-sample t-test ratio <1 : $t_8=-8.003$, $p=4.356e-5$). This finding is inconsistent with the idea of separate flexion and extension finger maps.

3.5 Discussion

Here we investigated how the population activity in M1 is organized for control of flexion and extension of single fingers. We analysed M1 population activity measured in humans with 7T fMRI and spiking data from NHPs while participants made isometric single finger presses in either direction. Importantly, we ensured the behavioural tasks in both experiments were carefully matched to allow us to compare results across the two datasets.

We first demonstrated that the representational structure of single finger flexion or extension presses in human M1 measured with fMRI were relatively well explained by the natural statistics of every-day movements, replicating the flexion results reported in Ejaz et al. (2015) and extending them to single finger extension movements. The same model, however, failed to correctly predict the relationship between flexion and extension movements. Because flexion and extension of the same finger cannot temporally co-occur, the model predicted quite separate representations for the two actions. In our data, however, we observed the opposite effect – cortical M1 activity patterns measured with fMRI in humans were very similar for the flexion and extension of the same finger, as compared to the quite distinct patterns for different fingers. We also analysed spiking data from a similar task in two monkeys and found that the similarity of finger flexion and extension were specific to fMRI: In the monkey electrophysiological recordings, different movement directions were associated with distinct patterns of neuronal activity.

The discrepancy between the fMRI and electrophysiological measures suggest a specific organization of finger flexion and extension movements in M1 (Fig. 3.7). This suggested architecture has two characteristics that likely contribute to the observed difference between measurement modalities.

First, we hypothesize that neurons that contribute to the flexion of a finger receive similar sensory input as neurons that contribute to the extension of the same finger (dashed line, Fig. 3.7). There is evidence in the literature to support such an organization. In macaque M1, single neurons tuned to torque production at the shoulder integrate information from the shoulder and elbow joints to facilitate rapid corrective responses to mechanical arm perturbations (Pruszynski et al., 2011). Thus, these neurons receive common sensory input about the shoulder and elbow joints, but the output is largely specific to movements about the shoulder. Additionally, units controlling flexion and extension of the same finger a likely to directly communicate with each other (curved solid arrows, Fig. 3.7). Such coordination would be necessary to orchestrate fast alternation of finger movements and to finely control the grip force during object manipulation.

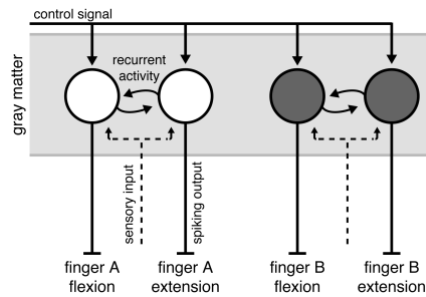


Figure 3.7: Summary model of M1 organization

Output neurons in M1 produce complex patterns of muscular activity. We refer to groups of neurons that, together, evoke a complex pattern of muscle activity that results in single finger movements as functional units (circles). These functional units receive a control signal input for the upcoming movement (solid lines with arrows). Functional units that evoke movements of the same finger in opposite directions receive common inputs (dashed lines) and share strong recurrent connections (circular lines). The spiking output (solid lines without arrows) of these units, however, is directionally specific. Additionally, under the spatial scale model, functional units tuned to finger movements in different directions are clustered together according to their finger tuning.

This organization would lead to highly similar fMRI activity patterns. In cortical grey matter, the BOLD signal measured with fMRI reflects mainly excitatory postsynaptic potentials (EPSPs), caused by input to a region or recurrent activity within a region (Logothetis et al., 2001). This is because much of the metabolic costs associated with signal transmission arise from re-establishing resting membrane potential of neurons after an EPSP (Attwell & Laughlin, 2001; Magistretti & Allaman, 2015; Yu et al., 2018). Given that the input to subpopulations controlling flexion and extension of the same finger will be highly temporally correlated, the fMRI activity patterns for the two movements should also be very similar.

At the same time, the two subpopulations need to produce distinct spiking outputs. To do so, the populations must receive a control signal input that defines whether to flex or extend a finger. Indeed, in our fMRI data, although flexion and extension patterns for the same finger were highly similar, we could still discriminate between the patterns. This control signal would influence how neurons react to sensory inputs and the information they exchange. Thus, the observed local variations in metabolic activity would be dissociated from the local neural firing rates (Picard, Matsuzaka, & Strick, 2013).

As a second characteristic, we also hypothesize that units controlling muscle patterns that produce flexion and extension of the same effector are spatially co-localized to support fast and efficient communication. Because fMRI samples activity in a coarse manner, even high-resolution fMRI is biased to functional organization at a coarse spatial scale (Kriegeskorte & Diedrichsen, 2016). Therefore, features that exist at fine spatial scales in the neural population are under-represented in fMRI activity patterns. Our results could therefore be caused by an organization where neurons tuned to different movement directions for the same finger (or combination of fingers) are clustered together, while neurons that control different fingers or finger combinations are more spatially separated. We did not find any evidence for a difference in spatial organization of fingers and direction in the fMRI data. However, given that this comparison itself is limited by the spatial resolution of fMRI, we cannot rule out that differences in the fine-grained spatial organization also contributed to the observed effect.

Although we experimentally studied the flexion and extension of single fingers, we do not suggest that isolated finger movements are explicitly represented in M1. Rather, M1 output neurons will produce a complex pattern of muscle activity. This complexity likely arises because the neuronal populations are optimized to produce muscle activities which elicit combinations of finger movements that are useful in everyday tasks (Poliakov & Schieber, 1999; Gentner & Classen, 2006; Ejaz et al., 2015). When we measure activity patterns related to movements of isolated fingers, we simply observe the specific combination of neuronal populations that need to be active to move a single finger (Schieber, 1990). The core of our hypothesis is that populations of neurons that produce opposing muscular patterns form a functional unit with increased communication, common sensory input, and potentially also spatial co-localization.

Our findings are at odds with the organization suggested by Huber et al. (2020). Using high-resolution functional imaging in humans, the authors reported evidence of two spatially distinct finger maps in M1, one for flexion and one for extension. Consistent with Huber et al., we found that individuated finger activity patterns in M1 are fractured and have multiple hotspots (Fig. 3.2). However, we found no evidence for a clear spatial separation of flexion and extension finger into two action maps (Fig 3.6F-G). Even though the spatial resolution of BOLD imaging in our study was lower than that of the blood-volume based method employed by Huber et al., we should have been able to detect larger spatial separations between flexion and extension movements than between individual fingers. Instead, the opposite was the case. Both the RSA and the spatial analyses showed greater differences between fingers than between directions. These results, however, are not unexpected. Partial inactivation of neurons in the hand area of macaque M1 result in a complex loss of flexion and/or extension movements of different fingers (Schieber & Poliakov, 1998), and electrophysiological recordings from this same area show flexion and extension preference is not spatially clustered (Schieber & Hibbard, 1993). We believe that the differences between our results and those of Huber et al. are likely explained by the fact that Huber et al. did not study flexion and extension of individual fingers, but relied on a large spatial gradient detected between whole-hand grasping and retraction. We think this is problematic, as the control requirements of individual finger movements is qualitatively different from those of whole hand grasping.

That is, neuronal activity during whole hand grasping is not the sum of the neural activity during individuated finger flexion movements (Ejaz et al., 2015), but rather engages a different control mechanism. Consistent with this idea, electrophysiological studies have shown that the neural control of whole hand and individuated finger movements relies on different neural subpopulations (Muir & Lemon, 1983; Lemon, 2008).

There are of course many caveats when comparing results across different recording methodologies, experimental setups, and species. While we tried to make the behavioural tasks across human and macaques as similar as possible, species differences or the extensive training for the non-human primates may account for some of the differences.

Overall, however, we believe that the comparison between fMRI and spiking provides some interesting insights into the organization of the hand region of the primary motor cortex. Cortical representations of single finger movements are not purely dictated by the kinematics of hand usage. We posit that the deviation from this organization appears to reflect a control process, where neurons tuned to movements of a specific finger receive common sensory input and share local recurrent processes. These tightly coordinated populations then produce the spiking output that needs to be quite distinct for the flexion and extension of the same finger.

3.6 References

- Arbuckle, S. A., Yokoi, A., Pruszynski, J. A., & Diedrichsen, J. (2019). Stability of representational geometry across a wide range of fMRI activity levels. *Neuroimage*, 186, 155-163.
- Attwell, D., & Laughlin, S. B. (2001). An energy budget for signaling in the grey matter of the brain. *J. Cereb. Blood Flow Metab.*, 21, 1133-1145.
- Beringer, C. R., Mansouri, M., Fisher, L. E., Collinger, J. L., Munin, M. C., Boninger, M. L., & Gaunt, R. A. (2020). The effect of wrist posture on extrinsic finger muscle activity during single joint movements. *Sci. Rep.*, 10, 8377.
- Bortoff, G. A., & Strick, P. L. (1993). Corticospinal terminations in two new-world primates: further evidence that corticomotoneuronal connections provide part of the neural substrate for manual dexterity. *J. Neurosci.*, 13, 5105-5118.
- Darling, W. G., Pizzimenti, M. A., Rotella, D. L., Peterson, C. R., Hynes, S. M., Ge, J., . . . Morecraft, R. J. (2009). Volumetric effects of motor cortex injury on recovery of dexterous movements. *Exp. Neurol.*, 220, 90-108.
- Diedrichsen, J., Berlot, E., Mur, M., Schütt, H. H., & Kriegeskorte, N. (2020). Comparing representational geometries using the unbiased distance correlation. *arXiv*.
- Diedrichsen, J., Provost, S., & Zareamoghaddam, H. (2016). On the distribution of cross-validated Mahalanobis distances. *arXiv*.
- Diedrichsen, J., Ridgway, G. R., Friston, K. J., & Wiestler, T. (2011). Comparing the similarity and spatial structure of neural representations: a pattern-component model. *Neuroimage*, 55, 1665-1678.
- Diedrichsen, J., Yokoi, A., & Arbuckle, S. A. (2018). Pattern component modeling: A flexible approach for understanding the representational structure of brain activity patterns. *NeuroImage*, 180, 119-133.
- Ejaz, N., Hamada, M., & Diedrichsen, J. (2015). Hand use predicts the structure of representations in sensorimotor cortex. *Nat. Neurosci.*, 18, 1034-1040.
- Firmin, L., Field, P., Maier, M. A., Kraskov, A., Kirkwood, P. A., Nakajima, K., . . . Glickstein, M. (2014). Axon diameters and conduction velocities in the macaque pyramidal tract. *J. Neurophysiol.*, 112, 1229-1240.
- Fischl, B., Rajendran, N., Busa, E., Augustinack, J., Hinds, O., Yeo, B. T., . . . Zilles, K. (2008). Cortical folding patterns and predicting cytoarchitecture. *Cereb. Cortex*, 18, 1973-1980.
- Fischl, B., Sereno, M. I., & Dale, A. M. (1999). Cortical surface-based analysis. II: Inflation, flattening, and a surface-based coordinate system. *Neuroimage*, 9, 195-207.
- Fischl, Sereno, M. I., Tootell, R. B., & Dale, A. M. (1999). High-resolution intersubject averaging and a coordinate system for the cortical surface. *Hum. Brain Mapp.*, 8, 272-284.

- Friston, K. J., Jezzard, P., & Turner, R. (1994). Analysis of functional MRI time-series. *Human Brain Mapping*, 1, 153-171.
- Gentner, R., & Classen, J. (2006). Modular organization of finger movements by the human central nervous system. *Neuron*, 52, 731-742.
- Graziano, M. S., & Aflalo, T. N. (2007). Mapping behavioral repertoire onto the cortex. *Neuron*, 56, 239-251.
- Heffner, R. S., & Masterton, R. B. (1983). The role of the corticospinal tract in the evolution of human digital dexterity. *Brain Behav. Evol.*, 23, 165-183.
- Huber, L., Finn, E. S., Handwerker, D. A., Bönstrup, M., Glen, D. R., Kashyap, S., . . . Bandettini, P. A. (2020). Sub-millimeter fMRI reveals multiple topographical digit representations that form action maps in human motor cortex. *Neuroimage*, 208, 116463.
- Hutton, C., Bork, A., Josephs, O., Deichmann, R., Ashburner, J., & Turner, R. (2002). Image distortion correction in fMRI: A quantitative evaluation. *Neuroimage*, 16, 217-240.
- Ingram, J. N., Körding, K. P., Howard, I. S., & Wolpert, D. M. (2008). The statistics of natural hand movements. *Exp. Brain Res.*, 188, 223-236.
- Kriegeskorte, N., & Diedrichsen, J. (2016). Inferring brain-computational mechanisms with models of activity measurements. *Philos. Trans. R. Soc. Lond. B Biol. Sci.*, 371.
- Lang, C. E., & Schieber, M. H. (2003). Differential impairment of individuated finger movements in humans after damage to the motor cortex or the corticospinal tract. *J. Neurophysiol.*, 90, 1160-1170.
- Lang, C. E., & Schieber, M. H. (2004). Human finger independence: limitations due to passive mechanical coupling versus active neuromuscular control. *J. Neurophysiol.*, 92, 2802-2810.
- Lawrence, D. G., & Hopkins, D. A. (1976). The development of motor control in the rhesus monkey: evidence concerning the role of corticomotoneuronal connections. *Brain*, 99, 235-254.
- Lawrence, D. G., & Kuypers, H. G. (1968). The functional organization of the motor system in the monkey. I. The effects of bilateral pyramidal lesions. *Brain*, 91, 1-14.
- Lemon, R. N. (2008). Descending pathways in motor control. *Annu. Rev. Neurosci.*, 31, 195-218.
- Li, Z.-M., Pfaeffle, H. J., Sotereanos, D. G., Goitz, R. J., & Woo, S. L.-Y. (2003). Multi-directional strength and force envelope of the index finger. *Clin. Biomech.*, 18, 908-915.
- Liu, Y., & Rouiller, E. M. (1999). Mechanisms of recovery of dexterity following unilateral lesion of the sensorimotor cortex in adult monkeys. *Exp. Brain Res.*, 128, 149-159.

- Logothetis, N. K., Pauls, J., Augath, M., Trinath, T., & Oeltermann, A. (2001). Neurophysiological investigation of the basis of the fMRI signal. *Nature*, 412, 150-157.
- Magistretti, P. J., & Allaman, I. (2015). A cellular perspective on brain energy metabolism and functional imaging. *Neuron*, 86, 883-901.
- Mogk, J. P., & Keir, P. J. (2003). The effects of posture on forearm muscle loading during gripping. *Ergonomics*, 46, 956-975.
- Muir, R. B., & Lemon, R. N. (1983). Corticospinal neurons with a special role in precision grip. *Brain Res.*, 261, 312-316.
- Nili, H., Wingfield, C., Walther, A., Su, L., Marslen-Wilson, W., & Kriegeskorte, N. (2014). A toolbox for representational similarity analysis. *PLoS Comput. Biol.*, 10, e1003553.
- Picard, N., Matsuzaka, Y., & Strick, P. L. (2013). Extended practice of a motor skill is associated with reduced metabolic activity in M1. *Nat. Neurosci.*, 16, 1340-1347.
- Poliakov, A. V., & Schieber, M. H. (1999). Limited functional grouping of neurons in the motor cortex hand area during individuated finger movements: A cluster analysis. *J. Neurophysiol.*, 82, 3488-3505.
- Pruszynski, J. A., Kurtzer, I., Nashed, J. Y., Omrani, M., Brouwer, B., & Scott, S. H. (2011). Primary motor cortex underlies multi-joint integration for fast feedback control. *Nature*, 478, 387-390.
- Sasaki, S., Isa, T., Pettersson, L.-G., Alstermark, B., Naito, K., Yoshimura, K., . . . Ohki, Y. (2004). Dexterous finger movements in primate without monosynaptic corticomotoneuronal excitation. *J. Neurophysiol.*, 92, 3142-3147.
- Schieber. (1991). Individuated finger movements of rhesus monkeys: a means of quantifying the independence of the digits. *J. Neurophysiol.*, 65, 1381-1391.
- Schieber, M. H. (1990). How might the motor cortex individuate movements? *Trends Neurosci.*, 13, 440-445.
- Schieber, M. H., & Hibbard, L. S. (1993). How somatotopic is the motor cortex hand area? *Science*, 261, 489-492.
- Schieber, M. H., & Poliakov, A. V. (1998). Partial inactivation of the primary motor cortex hand area: effects on individuated finger movements. *J. Neurosci.*, 18, 9038-9054.
- Schieber, M. H., & Rivlis, G. (2005). A spectrum from pure post-spike effects to synchrony effects in spike-triggered averages of electromyographic activity during skilled finger movements. *J. Neurophysiol.*, 94, 3325-3341.
- Schieber, M. H., & Rivlis, G. (2007). Partial reconstruction of muscle activity from a pruned network of diverse motor cortex neurons. *J. Neurophysiol.*, 97, 70-82.
- Tower, S. S. (1940). Pyramidal lesion in the monkey. *Brain*, 63, 36-90.

- Valero-Cuevas, F. J., Zajac, F. E., & Burgar, C. G. (1998). Large index-fingertip forces are produced by subject-independent patterns of muscle excitation. *J. Biomech.*, 31, 693-703.
- Walther, A., Nili, H., Ejaz, N., Alink, A., Kriegeskorte, N., & Diedrichsen, J. (2016). Reliability of dissimilarity measures for multi-voxel pattern analysis. *Neuroimage*, 137, 188-200.
- Wiestler, T., & Diedrichsen, J. (2013). Skill learning strengthens cortical representations of motor sequences. *eLife*, 2.
- Wiestler, T., McGonigle, D. J., & Diedrichsen, J. (2011). Integration of sensory and motor representations of single fingers in the human cerebellum. *J. Neurophysiol.*, 105, 3042-3053.
- Xu, J., Ejaz, N., Hertler, B., Branscheidt, M., Widmer, M., Faria, A. V., . . . Diedrichsen, J. (2017). Separable systems for recovery of finger strength and control after stroke. *J. Neurophysiol.*, 118, 1151-1163.
- Young, N. A., Collins, C. E., & Kaas, J. H. (2013). Cell and neuron densities in the primary motor cortex of primates. *Front. Neural Circuits*, 7, 30.
- Yousry, T. A., Schmid, U. D., Alkadhi, H., Schmidt, D., Peraud, A., Buettner, A., & Winkler, P. (1997). Localization of the motor hand area to a knob on the precentral gyrus. A new landmark. *Brain*, 120 (Pt 1), 141-157.
- Yu, B. M., Cunningham, J. P., Santhanam, G., Ryu, S. I., Shenoy, K. V., & Sahani, M. (2009). Gaussian-process factor analysis for low-dimensional single-trial analysis of neural population activity. *J. Neurophysiol.*, 102, 614-635.
- Yu, W. S., Duinen, H., & Gandevia, S. C. (2010). Limits to the control of the human thumb and fingers in flexion and extension. *J. Neurophysiol.*, 103, 278-289.
- Yu, Y., Herman, P., Rothman, D. L., Agarwal, D., & Hyder, F. (2018). Evaluating the gray and white matter energy budgets of human brain function. *Journal of Cerebral Blood Flow & Metabolism*, 38, 1339-1353.

Chapter 4

4 Mapping the integration of sensory information across fingers in human sensorimotor cortex

In my final project, I examined how somatosensory inputs from the fingers are integrated in S1. Sensory inputs from all fingers must be integrated during everyday hand use. However, previous work studying sensory integration across fingers have been restricted to studying how inputs from two fingers interact. Therefore, the full nature of finger interactions is unknown. In this chapter, I addressed this gap and characterized the magnitude of multi-finger interactions that occur in S1.

4.1 Abstract

The integration of somatosensory signals across fingers is essential for dexterous object manipulation. Previous experiments suggest that neural populations in the primary somatosensory cortex (S1) are responsible for this integration. However, the integration process has not been fully characterized, as previous studies have mainly used two-finger stimulation paradigms. Here, we addressed this gap by stimulating all 31 single- and multi-finger combinations. We measured population-wide activity patterns evoked during finger stimulation in human S1 and primary motor cortex (M1) using 7T functional magnetic resonance imaging (fMRI). Using multivariate fMRI analyses, we found clear evidence of unique non-linear interactions between fingers. In Brodmann area (BA) 3b, interactions predominantly occurred between pairs of neighboring fingers. In BA 2, however, we found equally strong interactions between spatially distant fingers, as well as interactions between finger triplets and quadruplets, suggesting the presence of rich, non-linear integration of somatosensory information across fingers.

4.2 Introduction

When writing with a pen or manipulating a Rubik's cube in one hand, the sensorimotor system needs to integrate somatosensory information from multiple fingers to estimate the object's shape, position, and movement within the hand. The mechanism that underlies this integration, however, remains poorly understood. We hypothesized that, in

order to support flexible behavioural responses to any pattern of sensory stimulation across the hand, sensory inputs from neighbouring and non-neighbouring fingers need to be integrated in a non-linear fashion. This non-linear code could then provide the neural substrate necessary to detect any specific pattern of stimulation across the hand, and provide the basis for learning a flexible mapping between sensory inputs and motor responses of the hand.

Stimulation to the fingers is relayed from mechanoreceptors via the cuneate nucleus to the thalamus, with signals from different fingers remaining largely segregated (Florence, Wall, & Kaas, 1988, 1989). Signals from different fingers begin to interact substantially only in S1 and M1 (Hsieh et al., 1995). Cortical sensory processing is critical for dexterous hand control, as perturbing either the transmission of somatosensory information from the hand to the cortex (Moberg, 1958; Monzée, Lamarre, & Smith, 2003; Chemnitz, Dahlin, & Carlsson, 2013), or lesioning S1 (Carlson, 1981; Hikosaka et al., 1985; Brochier et al., 1999) grossly impairs fine manual dexterity. We refer here to S1 and M1 collectively as sensorimotor cortex. In the primate brain this comprises six cytoarchitecturally distinct Brodmann areas (BA): 4a, 4p, 3a, 3b, 1, and 2 (Brodmann, 1909; Powell & Mountcastle, 1959; Geyer et al., 1996). Inputs from the thalamic somatosensory nuclei vary across these regions, with BA 3a and BA 3b receiving most of the inputs, BA 4a and BA 4p receiving a substantial amount, and BA 1 and BA 2 receiving progressively fewer (Jones & Powell, 1970; Jones, 1975; Shanks & Powell, 1981; Darian-Smith & Darian-Smith, 1993). In nonhuman primates, neurons in BA 3b have receptive fields mainly devoted to single fingers, whereas in BA 1 and BA 2, receptive fields encompass multiple fingers (Hyvärinen & Poranen, 1978b; Sur, 1980; Iwamura et al., 1993). Measuring the coarse spatial organization for fingers in these regions with fMRI reveals comparable findings in humans, with finger representations becoming more spatially overlapping in posterior subregions of S1 (Krause et al., 2001; Martuzzi, et al., 2014; Besle et al., 2014). At the single-neuron level, paired finger stimulation generally results in lower firing rates relative to what would be expected from summing the firing rates resulting from single finger stimulation (Friedman, Chen, & Roe, 2008; Lipton et al., 2010; Reed et al., 2010; Thakur, Fitzgerald, & Hsiao, 2012).

Together, these findings have been interpreted as evidence that inputs from multiple fingers are integrated in the sensorimotor cortex (Iwamura, 1998; Yau et al., 2016).

Everyday object manipulation often demands the integration of information across all fingers of the hand. In contrast, most previous studies have typically examined stimulation of only a few pairs of fingers. Consequently, the full nature of the interactions that occur between somatosensory inputs from all five fingers is not well characterized. Furthermore, it is unclear whether these previously reported suppressive interactions reflect the encoding of specific patterns of multi-finger stimulation (i.e., non-linear finger integration) or simply divisive normalization (Carandini & Heeger, 2011; Brouwer et al., 2015), where the inputs coming from individual fingers are linearly combined, but the net activity suppressed through a diffuse inhibition. Studies of finger integration in humans also share these limitations (Gandevia, Burke, & McKeon, 1983; Hsieh et al., 1995; Biermann et al., 1998; Ishibashi et al., 2000; Hoechstetter et al., 2001; Ruben et al., 2006).

Here, we addressed this gap by studying all 31 possible finger combinations by simultaneously stimulating one, two, three, four, or five fingers of the right hand. We measured activity patterns evoked in the hand area of the sensorimotor cortex using 7T fMRI while human participants experienced passive tactile stimulation. Consistent with previous work, we found progressive overlap of single finger representation in sensorimotor cortex. By analyzing the multivoxel activity patterns in each subregion, we also found clear evidence for progressively stronger multi-finger interactions in posterior S1 and M1.

4.3 Results

4.3.1 Finger stimulation evokes broadly distributed activity in sensorimotor cortex

Using high-resolution 7T fMRI, we measured the activity patterns evoked by passive finger stimulation in the brains of 10 human participants. Stimulation was delivered independently to each fingertip of the right hand by indenting the skin with a small rod pushed by a pneumatic piston. We tested the entire set of 31 single- and multi-finger

combinations. To keep participants engaged during the experiment, they were instructed to detect rare mismatches between the stimulated combination and a visual probe presented after the stimulation (see Methods).

Figure 4.1A shows the group-average percent signal change (relative to rest) during right-hand finger stimulation on a flattened surface view of the cortical hand regions in S1 and M1 of the left hemisphere. During single-finger stimulation, evoked activity was low, but as more fingers were stimulated, we observed an increase in overall activity across subregions of the sensorimotor cortex. To statistically evaluate activity, we subdivided the hand region into six anatomically defined Brodmann areas using a cytoarchitectonic atlas (Fischl et al., 2008), spanning from BA 4a to BA 2 (see Methods). In each BA subregion, activity increased when more fingers were stimulated (all $F_{(4,36)} \geq 4.730$, all $p \leq 0.0036$; see Fig. 4.1B).

This activity increase does not provide a detailed view of how sensory information from different fingers is integrated in the human sensorimotor cortex. As a starting point to address this question, we quantified how dissimilar the local single-finger activity patterns were from each other. We used a crossvalidated estimate of the dissimilarity measure (crossnobis, see Methods), such that a value of zero indicated that patterns only differed by noise, and larger dissimilarity values indicated that the patterns were increasingly distinct. The average dissimilarities showed that single-finger stimulation evoked distinct finger patterns in all subregions (Fig. 4.1C), similar to the distribution of average activity. Indeed, all considered BA regions showed highly significant finger-specific pattern differences (one-sided t-test > 0 : all $t_9 \geq 3.012$, all $p \leq 0.0073$, Bonferroni corrected α -value = 0.0083). Dissimilarities between all 2-, 3-, and 4-finger combinations showed a similar spatial distribution, although the overall magnitude of the dissimilarities was reduced compared to the single-finger patterns (Fig. 4.1D). This finding is expected because multi-finger combinations also share an increasing number of fingers.

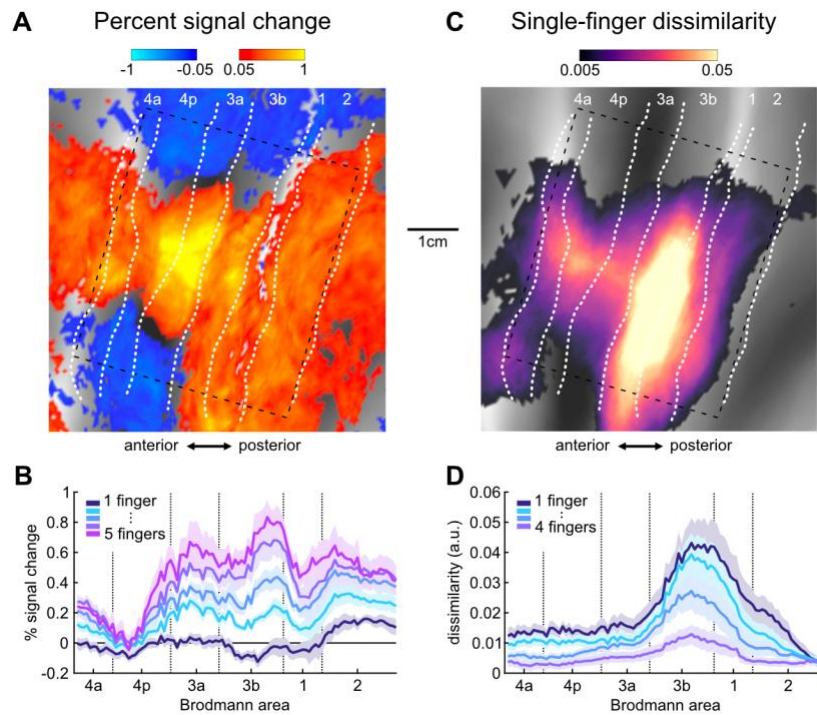


Figure 4.1: Activation and representation of fingers in the sensorimotor cortex

(A) Group-average percent signal change (relative to resting baseline) across all 31 possible finger combinations, projected to a flattened view of the left cortical sensorimotor areas around the central sulcus. Approximate boundaries of cytoarchitectonic areas (Fischl et al., 2008) are indicated by white dotted lines. The gray background indicates the average sulcal depth, with gyri in light, and sulci in dark colours. The rectangle indicates the area of averaging in the cross-sections in B and D. The scale bar approximates 1 cm on the flattened surface.

(B) Profile plot of the average percent signal change (\pm SEM across participants), grouped by the number of fingers in each combination.

(C) Cortical surface map of the average crossnobis dissimilarity between activity patterns evoked by single-finger stimulation.

(D) Profile plot of the average crossnobis dissimilarity (\pm SEM across participants) between pairs of single-finger, 2-finger, 3-finger, or 4-finger combinations.

4.3.2 Increasing overlap of single-finger patterns in sensorimotor cortex

Based on previous electrophysiological (Hyvärinen & Poranen, 1978b; Sur, 1980; Iwamura et al., 1993) and fMRI (Martuzzi et al., 2014; Besle et al., 2014) results, we would expect to find relatively focal single-finger activation in BA 3b, with more overlap between fingers in other parts of the sensorimotor cortex. This seemed to be the case as shown in the single-finger patterns for two exemplary participants (Fig. 4.2A). Each finger activated a quite distinct region of BA 3b and BA 3a. In contrast, the spatial patterns for each finger in BA 1 and BA 2, as well as in M1 (BA 4a and BA 4p) were more complex and involved multiple “hot spots” per finger, with substantial overlap between fingers.

We quantified this observation by computing a measure of finger-selectivity for each voxel. We selected voxels from each region that were significantly responsive to stimulation of any individual finger (see Methods), and scaled the responses of these voxels, such that the activity associated with the finger that evoked the largest positive response (i.e., the most-preferred finger) equaled 1, and the activity associated with the finger that evoked the smallest response (i.e., the least-preferred finger) equaled 0. If the voxel was only tuned to one finger, all non-preferred fingers would have a value of zero. The average scaled responses for the 4 non-preferred fingers therefore can be used as a measure of the selectivity of that voxel (Fig. 4.2B). To then define a selectivity index, we subtracted the averaged scaled responses for the 4 non-preferred fingers from 1, such that 1 indicates maximal selectivity, and 0 equal activation for all fingers. We averaged the selectivity indices across voxels per participant in each region.

Before comparing this selectivity index across regions, we needed to address one last problem – namely, regions with less reliable data could appear to be more broadly tuned to multiple fingers simply because higher measurement noise makes the tuning less clear. This is a concern because the strength of single-finger representations, as measured in the average pattern dissimilarities, varied across regions (Fig. 4.1D). Previous imaging work (Martuzzi et al., 2014; Besle et al., 2014) has not accounted for this potential confound. Here we addressed this issue by computing the expected selectivity indices for random

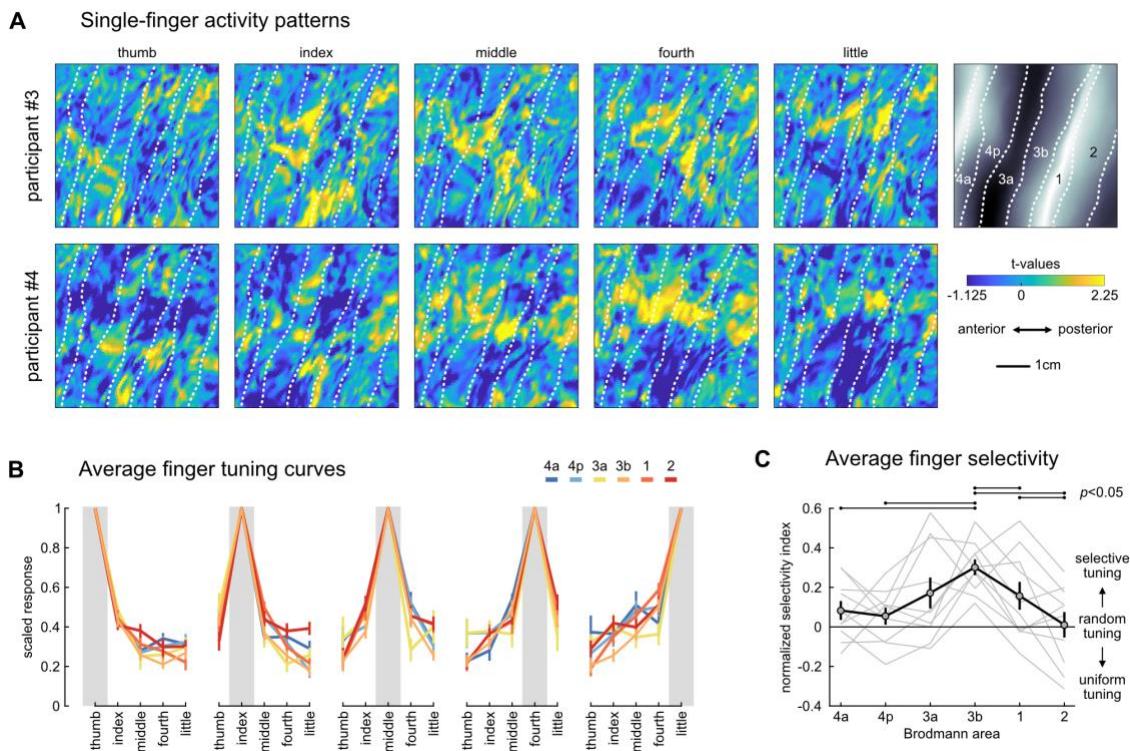


Figure 4.2: Finger tuning in the sensorimotor cortex

(A) Activity patterns for each of the five fingers from one participant, projected onto a flattened cortical surface and cut to include BA 3a to BA 2 in each panel.

(B) Average scaled voxel tuning curves arranged by most preferred finger (denoted by the gray box). Each colour corresponds to different regions.

(C) Normalized finger selectivities per region. Light gray lines reflect normalized selectivities per participant, and solid black line reflects the average across participants. A-priori paired t-tests were conducted between selectivities from different regions, and lines above the plot denote significant differences. Errorbars in B and C reflect SEM across participants in each region.

tuning and for perfectly selective tuning, given the signal reliability in each region and each participant (see Methods). We then normalized the measured selectivity for each participant and region separately, with 0 indicating random tuning and 1 indicating perfect tuning for a single finger only.

After carefully controlling for signal reliability across regions, we confirmed that voxels in BA 3b showed strong selectivity for single fingers (Fig. 4.2C), significantly more than expected from random tuning (one-sided t-test >0 : $t_9=7.557$, $p=1.739e-5$). In comparison, more posterior subregions of S1 were more broadly tuned, indicated by significantly lower selectivity indices compared to BA 3b (BA 1: $t_9=2.152$, $p=0.0299$, BA 2: $t_9=4.839$, $p=0.0005$). Indeed, in BA 2, the finger selectivity indices did not differ from what would be expected assuming random tuning curves ($t_9=1.687$, $p=0.8696$). Moving anterior relative to BA 3b, voxels appeared less selective in BA 3a but this difference failed to reach statistical significance ($t_9=1.482$, $p=0.0862$).

Selectivity indices in M1 were significantly lower than in BA 3b, for both posterior (BA 4p, $t_9=4.669$, $p=0.0006$) and anterior portions (BA 4a, $t_9=3.052$, $p=0.0069$). Rathelot and Strick (2009) proposed that “new M1” is more essential for individuated finger movements than “old M1”, from which one may predict that new M1 should show more selective single-finger representation. To test this prediction, we contrasted BA 4p and BA 4a, which may approximate old and new M1, respectively. Contrary to this prediction we found no difference in the average selectivity indices between these regions ($t_9=-0.496$, $p=0.6841$). Taken together, however, our analyses confirm the idea that sensory information from individual fingers is spatially quite segregated in BA 3b, but then continuously intermixes when moving more anterior or posterior in the sensorimotor cortex.

4.3.3 Interactions between finger activity patterns explain spatial complexity of multi-finger patterns

Having established that somatosensory inputs from different fingers heavily overlap in regions of the sensorimotor cortex, we then asked how somatosensory inputs are integrated across fingers. As a first step, we inspected the spatial activity patterns evoked

during multi-finger stimulation. Figure 4.3A shows the activity patterns from two exemplary participants during stimulation of the index finger, the little finger, or during stimulation of both fingers. The spatial patterns evoked by stimulating each finger had a relatively focal activation point in BA 3b. For the combined stimulation, we can see two areas of activation, one corresponding to the region active for the index finger, and the other corresponding to the region active during for the little finger. This suggests that the representation of inputs from multiple fingers in BA 3b may be linear, simply reflecting the superposition of activity caused by the stimulation of the individual fingers. We would expect such linearity if the inputs from different fingers do not interact with each other.

In contrast, the multi-finger spatial pattern in BA 1 and BA 2 appeared more complex, with clusters of activity emerging during simultaneous stimulation that were not present when either finger was stimulated individually. Given that the neural populations representing each finger appeared to be more overlapping in these same regions, the complexity of the spatial patterns suggests the presence of an interaction between fingers.

To test this idea formally, we fit a series of representational models to the activity patterns in each participant and region. These encoding-style models were fit to the activity patterns across all voxels in a subregion during single- and multi-finger stimulation, and then evaluated by their ability to predict multi-voxel activity patterns measured during an independent test run (see Methods). To compare model fits across regions, we normalized them to the performance of a null model and a noise-ceiling model. The null model predicted that the overall activity would increase when more fingers are stimulated, but that the activity patterns themselves would not differ between finger combinations. The noise-ceiling model was fit by estimating a unique pattern for each finger combination from the data, i.e. the model allowed for any arbitrary non-linearity. The model fits were then normalised between the null model (0) and noise-ceiling model (1), to express how much of the replicable finger-specific variation in the activity patterns each model could explain. Based on the observations in BA 3b, we first examined to what degree multi-finger patterns were simply the sum of the constituent single-finger patterns. The predictive performance of this linear model was significantly

better than that of the null model across the sensorimotor cortex (region x model ANOVA, main effect of model: $F_{(1,9)}=590.662$, $p=1.618e-9$; see Fig. 4.3B), indicating that the linear model captured some reliable aspects of the spatial activity patterns. Furthermore, the normalized linear model fit varied across regions (region x model ANOVA, interaction effect: $F_{(5,45)}=7.308$, $p=4.385e-5$). The best fit was observed in BA 3b, with significantly lower fits in all other regions (all $t_9 \geq 4.139$, all $p \leq 0.0025$, evaluated at a Bonferroni corrected α -value=0.01) except BA 3a ($t_9=2.822$, $p=0.0200$), where the difference was not significant after correction. Importantly, in all regions the linear model predicted the data significantly worse than the noise-ceiling model (all $t_9 \geq 5.318$, all $p \leq 0.0005$), suggesting that there were unexplained systematic non-linearities.

To visualize more generally how the linear model fit across the sensorimotor cortex in a region-blind manner, we applied the same model fitting to data from regularly tessellated regions (Fig. 4.3C, see Methods). This yielded similar results, with good fits in BA 3b and increasing non-linearities in regions anterior and posterior to it.

We then considered the possibility that non-linearities in how the activity patterns for single fingers combine would arise from the interaction of pairs of fingers, perhaps via local surround-inhibition or divisive normalization between two finger representations. Therefore, we created a two-finger interaction model, which explained all patterns as the sum of the component single-finger patterns, as well as their two-finger interactions (see Methods). Across all regions, this two-finger interaction model predicted left-out data significantly better than the linear model (region x model ANOVA, main effect of model: $F_{(1,9)}=209.851$, $p=1.526e-7$).

The amount of variance explained by these two-finger interactions, however, differed across regions (Fig. 4.3D). While the two-finger interactions lead to a small gain in predictive performance in BA 3b ($8.44 \pm 0.83\%$), the gain was over four times larger in BA 2 ($37.37 \pm 4.41\%$). Indeed, the region x model interaction effect was highly significant ($F_{(5,45)}=9.753$, $p=2.320e-6$). This indicates that a larger proportion of the pattern variance could be explained in regions outside of BA 3b when including interaction effects between pairs of fingers.

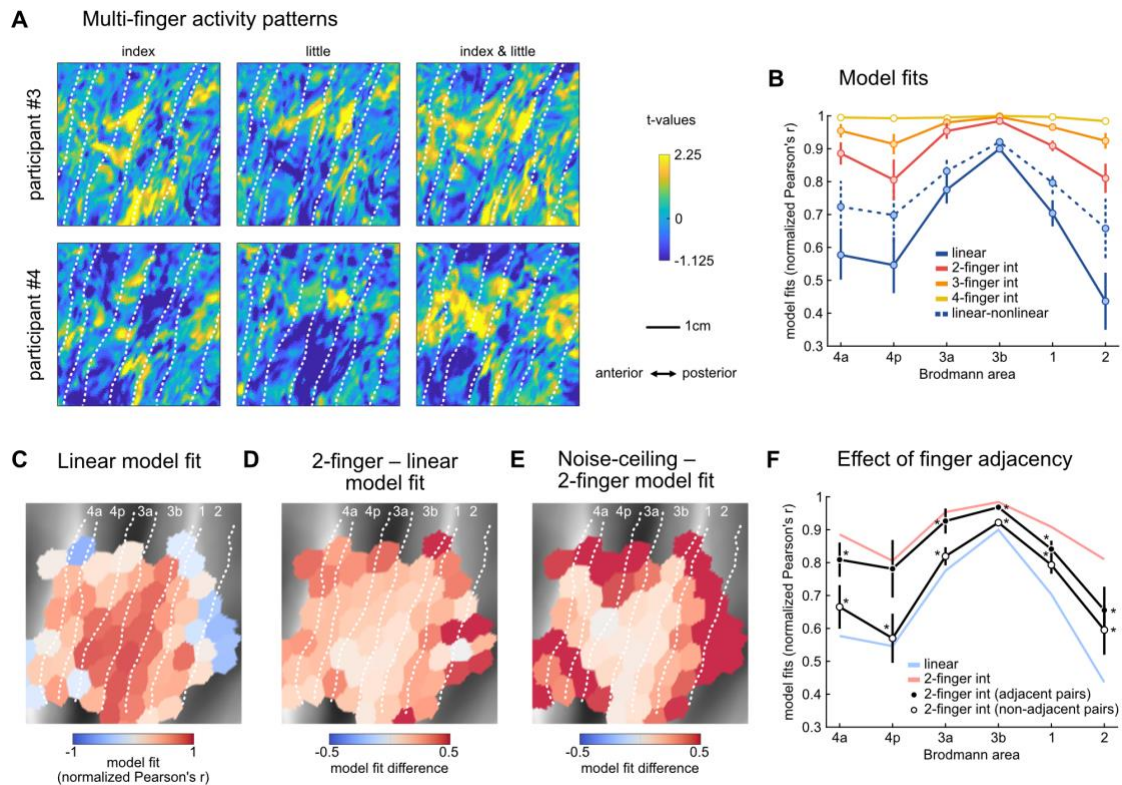


Figure 4.3: Multi-finger activity patterns in the somatosensory cortex

(A) Exemplar activity patterns from the participants displayed in Figure 2A.

(B) Representational model fits were normalized to the null model (0) and the noise-ceiling (1) in each region in each participant. Dots reflect the mean and error bars reflect SEM across participants per region.

(C) Surface map of the linear model fit (median across participants) in tessels where there were significant differences between all finger combination patterns (average paired dissimilarities between finger combination patterns ≥ 0.005). The dashed outline indicates the area shown in 3A and 2A.

(D) Difference between the fits of the 2-finger interaction model and the linear model in each tessel (median across participants).

(E) Difference between the noise-ceiling and the fit of the 2-finger interaction model in each tessel. Note that the colour scale for C is different than that for D and E.

(F) The full 2-finger interaction model (red line) was compared to a model that only contained the adjacent (black markers) or the non-adjacent (white markers) finger-pairs. Asterisks denote significantly lower model fits compared to using all interactions (two-sided paired t-test, $p < 0.05$).

4.3.4 Interactions do not only arise between adjacent fingers

Do the non-linear interactions between fingers described above arise mostly between adjacent fingers or do interactions also arise between spatially distant fingers of the hand? Previous work has shown that stimulating adjacent fingers leads to lower activity compared to non-adjacent fingers, which has been interpreted as evidence that adjacent fingers interact more than non-adjacent fingers (Biermann et al., 1998; Friedman et al., 2008; Hsieh et al., 1995; Ishibashi et al., 2000; Lipton et al., 2010). However, whether adjacent finger interactions are stronger across all regions of the sensorimotor cortex is not known. We investigated this by fitting two variants of the full two-finger interaction model, either including only the interaction terms for either adjacent or non-adjacent finger-pairs. Using only the non-adjacent pairs resulted in significantly lower model performance in all regions compared to using all finger-pairs (all $t_9 \leq -5.609$, all $p \leq 0.0003$; see Fig. 4.3F). When we used the adjacent finger pairs, the model performance was not significantly reduced in BA 4p ($t_9 = -0.605$, $p = 0.5600$), BA 4a ($t_9 = -2.793$, $p = 0.0210$), and BA 3a ($t_9 = -1.318$, $p = 0.2199$) when correcting for multiple comparisons (α -value = 0.0083). In contrast, the fits in BA 3b, BA 1, and BA 2 were significantly lower (all $t_9 \leq -4.611$, all $p \leq 0.0013$). This suggests that in posterior regions of the sensorimotor cortex, interactions between both adjacent and non-adjacent finger-pairs were important in explaining the multi-finger activity patterns. Furthermore, a significant region \times model interaction ($F_{(5,45)} = 3.199$, $p = 0.0148$) indicated that the effect of finger adjacency differed across regions. In BA 2, the predictive power of adjacent or non-adjacent interactions was comparable (two-sided paired t-test: $t_9 = -1.403$, $p = 0.1941$), whereas non-adjacent interactions were significantly less important in all other subregions (all $t_9 \leq -3.090$, all $p \leq 0.0130$). This suggests that BA 2 shows strong interactions between finger-pairs irrespective of finger adjacency.

4.3.5 Complexity of finger interactions increases along sensorimotor cortex

Thus far, we have demonstrated that population activity across sensorimotor cortex strongly represents two-finger interactions. However, in order to provide the neural substrate necessary to skillfully manipulate an object held in the entire hand, the

sensorimotor system needs to be able to detect specific patterns of stimulation across all fingers. Therefore, we should find evidence for integration of information across more than two fingers.

In BA 3b and BA 3a, the two-finger interaction model provided a good fit to the multi-finger activity patterns. In these regions, the model performance of the two-finger interaction model was very close to the noise-ceiling model, accounting for $98.42 \pm 0.38\%$ and $95.37 \pm 2.40\%$ of the reliable pattern variance, respectively. While a small significant difference remained in BA3b (two-sided paired t-test: $t_9=4.162$, $p=0.0024$), the two-finger interaction model explained the activity patterns as well as the noise-ceiling model in BA 3a ($t_9=1.916$, $p=0.0877$). Thus, neural populations in BA 3b and BA 3a do not appear to provide a unique, and hence linearly separable, representation of all possible multi-finger combinations.

In contrast, the predictive performance of the two-finger interaction model was still lower than the noise-ceiling in the other regions (all $t_9 \geq 3.142$, all $p \leq 0.0119$; see Fig. 4.3E). We therefore considered the interactions of three fingers in our models (see Methods). By including three-finger interactions, we were able to explain the activity patterns as well as the noise-ceiling model in BA 4a ($t_9=2.183$, $p=0.0569$). In BA 4p, BA 1, and BA 2, however, performance was still significantly lower than the noise-ceiling (all $t_9 \geq 2.731$, $p \leq 0.0232$). Only after including four-finger interactions were we able to fully explain the activity patterns in these remaining regions (all $t_9 \leq 2.154$, $p \geq 0.0597$). This suggests that the interactions in the most anterior and posterior regions of the sensorimotor cortex are more complex, involving non-linear interactions between three or more fingers. Therefore, our results appear to indicate that BA1, BA2, and also BA4 integrate sensory information arriving from multiple fingers to create a unique representation of specific patterns of multi-finger stimulation.

4.3.6 Finger interactions do not reflect a general suppression of activity

There is, however, an alternative and relatively simple mechanism that could give rise to the poor performance of the linear model in subregions of the sensorimotor cortex.

Specifically, it may be the case that the single-finger activity patterns combine linearly, but that the overall activity in each region is scaled in a non-linear fashion. Such non-linear scaling could arise from divisive normalization of the overall activity within the region, or from non-linearities between neural activity and the BOLD signal.

To test this, we expanded the linear model to allow for non-linear scaling of overall activity (see Methods). Indeed, this linear-nonlinear model provided a significantly better fit than the original linear model in all BA regions (two-sided paired t-test: all $t_9 \geq 6.105$, all $p \leq 0.0002$; see Fig. 3B). This alone should not be too surprising, given that the average activity did not scale linearly with the number of fingers stimulated (Fig. 4.1B).

Importantly, however, the predictive performance of the two-finger interaction model remained significantly better than that of the linear-nonlinear model in BA 3a, BA 3b, BA 1, and BA 4 (all $t_9 \geq 3.395$, all $p \leq 0.0079$). Although this difference was not significant in BA 2 after applying Bonferroni correction for multiple comparisons ($t_9 = 3.291$, $p = 0.0094$, α -value = 0.0083), the two-finger interaction model still accounted for $15.23 \pm 4.63\%$ more pattern variance in this region. Furthermore, compared to the higher-order interaction models, the linear-nonlinear model performed substantially worse in BA 2 (flexible vs. three-finger: $t_9 = -2.837$, $p = 0.0195$; four-finger: $t_9 = -3.715$, $p = 0.0048$), and more generally across the sensorimotor cortex (Fig. 4.3B). Therefore, the non-linearities captured by our multi-finger interaction models likely reflect complex interactions that arise between specific sets of finger patterns, rather than simply reflecting a general non-linear scaling of activity across the region.

4.4 Discussion

In this study, we investigated how somatosensory information coming from the fingers is integrated in different areas of the sensorimotor cortex. We hypothesized that to guide skillful object manipulation, the sensorimotor system needs to be able to detect relatively arbitrary combinations of sensory inputs across fingers, requiring non-linear integration of any pair, triplet, and quadruplet of fingers. We reported that voxels in BA 3b tend to be selectively tuned to the inputs from a single finger, whereas regions anterior and posterior show less finger-specificity, even after we controlled for differences in signal to noise. In

previous work, this broader tuning to multiple fingers has often been interpreted as evidence for finger integration (Iwamura et al., 1993; Martuzzi et al., 2014). However, spatial overlap itself only suggests that individual fingers are represented in overlapping neural populations— it does not necessarily mean that information from different fingers is integrated. By using the full set of multi-finger combinations and representational model analyses, we could show that the multi-finger patterns could not be explained by a simple linear combination of the single-finger patterns. Rather, most regions showed clear non-linearities, which not only reflected interactions between pairs of finger-pairs, but by any combination of multiple fingers.

An important strength of our experimental design was that it allowed us to test whether the observed non-linearities really reflected integration of information across the fingers. Alternatively, a relatively simple explanation for our results is that the activity patterns caused by single finger stimulations are simply summed but that the overall activity is then suppressed in a non-linear fashion. Previous studies have been unable to distinguish between these two explanations, as they used very few multi-finger combinations, making it difficult to dissociate global non-linear activity suppression from unique non-linear interactions (Gandevia et al., 1983; Hsieh et al., 1995; Biermann et al., 1998; Ishibashi et al., 2000; Hoechstetter et al., 2001; Ruben et al., 2006; Lipton et al., 2010; Brouwer et al., 2015). Having stimulated all possible multi-finger combinations, we had sufficient leverage to distinguish between these two possibilities and were able to rule out simple global suppression. That is, the interactions we report in this paper likely reflect rich, non-linear integration of sensory inputs from the fingers.

The fit of the linear combination model was greatest in BA 3b, where neurons have receptive fields that are largely restricted to single fingers (Sur, 1980; Iwamura et al., 1993) and preferentially code for tactile features that can be extracted from local spatial regions such as stimulus edge orientation (Hyvärinen & Poranen, 1978a; Bensmaia et al., 2008). However, this is not to say that multi-finger integration was entirely absent in BA 3b. Indeed, consistent with previous work (Reed et al., 2008, 2010; Lipton et al., 2010; Thakur et al., 2012), we found significant finger-pair integration in BA 3b. Interactions were stronger between adjacent fingers, indicating that the majority of integration that

occurs in BA 3b is across spatially close distances, as previously reported (Reed et al., 2008).

Moving posterior from BA 3b to BA 2, we observed progressively more complex multi-finger interactions, with evidence for non-linear interactions of all possible multi-finger combinations in BA 2. This complexity matches the changes in tactile feature preference of individual neurons, shifting from local tactile features like edge orientation (Bensmaia et al., 2008) to higher-order features that span multiple fingers like object curvature (Yau, Connor, & Hsiao, 2013). The interactions also occurred for finger pairs of increasing spatial distance. Indeed, the interactions between adjacent and non-adjacent fingers were equally strong in BA 2. Such broad spatial integration is important for extracting spatially invariant higher-order tactile features of an object (Yau et al., 2016). Together, these observations provide empirical support for the hypothesis that tactile inputs from the hand are progressively elaborated along the sensory cortical pathway (Hyvärinen & Poranen, 1978b; Phillips, Johnson, & Hsiao, 1988; Iwamura, 1998).

We also examined sensory processing in the hand area of M1, which has commonly been ignored in previous work. Although BA 4 is traditionally viewed as a motor area, it receives substantial inputs from the somatosensory thalamus (Jones, 1975; Darian-Smith & Darian-Smith, 1993) and from various areas of S1 (Ghosh, Brinkman, & Porter, 1987). Therefore, neural populations in this region may also be involved in integrating tactile inputs from the fingers, perhaps for rapid behavioural responses to object displacements (Crevecoeur et al., 2017; Hernandez-Castillo et al., 2020). Our results demonstrate that there were finger interactions in BA 4, and the strength of these interactions were comparable to those in BA 2. However, it is not clear whether these interactions arose specifically within BA 4 or reflect inputs from BA1 or BA 2.

What benefit does non-linear finger integration of information from different fingers provide? From an ethological standpoint, non-linear finger integration allows for a more flexible mapping between sensory inputs and motor responses. For example, consider the scenario where you are holding a cup in your hand and must prevent it from slipping out of your grasp. Any movement of the cup across your fingers will provide stimulation, but

the appropriate behavioural responses to these inputs differ. For example, a downward movement of the object would cause slip in the same direction across all fingers, whereas an object rotation would elicit slip signals in opposite directions on the index and little finger. Only a non-linear integration of the slip-direction signals, therefore, would allow the mapping of these different patterns to distinct motor responses.

More broadly, our results are also in agreement with recent evidence from multi-whisker stimulation studies in rodents, where multi-whisker combinations are uniquely represented by neural populations in the rodent barrel cortex (Laboy-Juárez et al., 2019; Lyall et al., 2020). These studies, together with our current results, suggest that non-linear integration between somatosensory inputs is a general feature of somatosensory processing.

In our experiment, we required participants to remain attentive to the finger stimulation. Processes of selective attention have been shown to modulate neural firing rates in response to finger stimulation (Hsiao, O'Shaughnessy, & Johnson, 1993). To what degree are our findings caused by raw sensory input, and to what degree do top-down influences modulate the sensory processing? The sequence of trials was fully randomized, such that in the moment of stimulation, participants did not know what combination to expect. In this respect we can be sure that our results are clearly dependent on the actual sensory input. Nonetheless, it is quite likely that some cognitive processes may influence how sensory information from the hand is processed. Indeed, neural populations in S1 are modulated by inputs from M1 (Goldring et al., 2014), and the neural state of S1 is strongly influenced by the planning of upcoming actions (Ariani, Pruszynski, & Diedrichsen, 2020; Gale, Flanagan, & Gallivan, 2021). Such modulation is important, as the processing requirements of somatosensory information depends on the task at hand. For example, the reaction to object slip depends not only on the direction of the slipping object (Häger-Ross, Cole, & Johansson, 1996), but also on the perceived physical properties of the object (i.e., how “object-like” the simulation is, Ohki, Edin, & Johansson, 2002), and the behavioural goal (Hernandez-Castillo et al., 2020). We may therefore expect that, in order to provide support for flexible sensory-motor mapping, the way that information is integrated across fingers changes with the behavioral context.

Thus, the next challenge is to probe how such top-down influences alter the integration of somatosensory inputs from the fingers.

4.5 Methods

4.5.1 Participants

Ten healthy participants were recruited for the study (7 males and 3 females, mean age=25.5, SD=3.24; mean Edinburgh handedness score=58.42, SD=55.43). Participants completed one training session and two experimental sessions. During the training session, participants were familiarized with the finger stimulation task. In the two experimental sessions, participants experienced finger stimulation while undergoing 7T fMRI. All participants provided informed consent before the beginning of the study, and all procedures were approved by the Office for Research and Ethics at the University of Western Ontario.

4.5.2 Stimulation apparatus

We used a custom-built five-finger keyboard to apply stimulation independently to each of the five fingers of the right hand. Each finger was comfortably restrained above an immobile key using a clamp covered with padding (Fig. 4.4A). The clamp prevented any hand or finger movement and ensured that the passive stimulation was delivered to a constant area of the fingertip. We delivered independent stimulation to each fingertip, using a pneumatic air piston mounted underneath each key. The pistons were driven by compressed air (100 psi) delivered from outside the MRI scanning room through polyvinyl tubes. The air pressure for each piston rod was regulated by adjustable valves, which were controlled on-line using a PID controller to deliver forces of ~3 Newtons to each fingertip (one participant experienced stimulation of ~2N). The piston rods (diameter=3mm) deformed the skin of the fingertip. As the padding prevented movement of the finger, the stimulation was predominantly tactile in that it involved deformation of the skin. The forces applied to the fingertips were monitored using force transducers (Honeywell-FS series, dynamic range=0-16N, resolution<0.02N, sampling rate=200Hz).

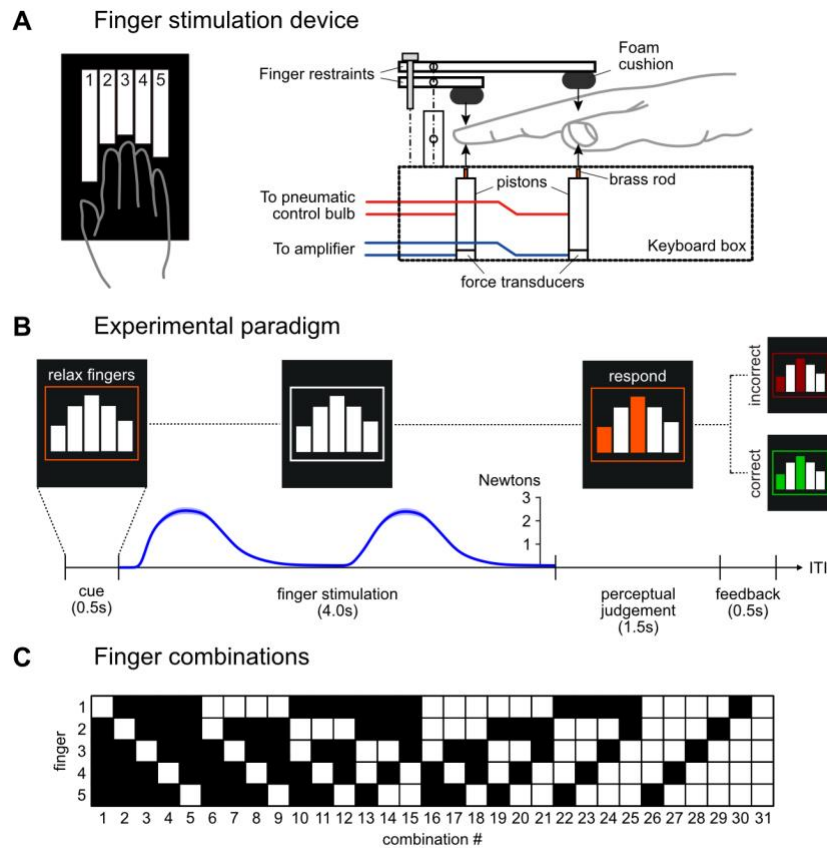


Figure 4.4: Experiment paradigm

(A) Participants experienced tactile stimulation using a custom-built finger stimulation box. Each finger was independently restrained, and pneumatic pistons were used to deliver stimulation to each fingertip.

(B) Schematic illustration of a single trial (ITI: inter-trial-interval). The blue trace shows the mean finger stimulation force (\pm SEM across participants), time aligned to the start of the stimulation phase.

(C) Participants experienced stimulation of all 31 possible single- and multi-finger combinations.

4.5.3 Finger stimulation task

While lying in the scanner, participants viewed a back-projection screen through a mirror mounted to the head coil. They saw five bars in the centre of the screen, surrounded by a box (Fig. 4.4B). Each bar corresponded to one of the five fingers of the right hand (left-to-right: thumb-to-little finger). All 31 possible finger combinations were stimulated (5 single-finger, 10 two-finger, 10 three-finger, 5 four-finger, and 1 five-finger combination; Fig. 4.4C).

Each trial lasted 6.5s and consisted of four phases (Fig. 4.4B): a cue phase (0.5s), finger stimulation (4s), perceptual judgement (≤ 1.5 s), and feedback (≥ 0.5 s). The cue phase alerted participants to the start of the trial. During the cue, the outline box on the turned orange and the words “RELAX FINGERS” were presented on screen, instructing participants to relax their hand. No information was provided about which finger combination was going to be stimulated, and therefore participants remained naïve about the stimulation until it occurred. At the start of the stimulation phase, the words disappeared from the screen and the box turned white, after which one of the 31 possible finger combinations was stimulated. The stimulated force on each finger approximated a rectified sine wave, gradually increasing and decreasing. Each “wave” of stimulation lasted approximately 1s, and two complete waves were delivered during each trial. Across all fingers and combinations, the average peak stimulated force was $2.67\text{N} \pm 0.17\text{N}$.

To ensure that participants remained attentive during the experiment, we asked them to detect the occurrence of relatively rare (5%) probe trials. In the perceptual judgement phase of each trial, we presented a visual presentation of a specific finger combination, with the boxes corresponding to the stimulated fingers turning orange (Fig. 1). On 3 out of 62 trials per run, these presented and stimulated patterns did not match (probe trials). Participants were asked to detect this mismatch and indicate it by pressing their right thumb (2N threshold). They were instructed to refrain from pressing any finger in case the presented and stimulated pattern matched. Participants had 1.5s to judge and respond. After either 1.5s elapsed (indicating a match) or immediately following a thumb press (indicating a mismatch), participants were provided feedback on their response by

changing the colour of the finger combination green (correct) or red (incorrect). The feedback was presented on-screen for ≥ 0.5 s, such that the feedback and response phases together lasted 2s regardless of response type.

To encourage good performance, participants received points based on the performance of their perceptual judgements. They were awarded 1 point for correctly identifying a matching configuration, and 10 points for correctly identifying a mis-matched configuration. False alarms were penalized by -1 point, and misses (failing to recognize a mis-match configuration) was penalized by -10 points. Points were combined across imaging runs and used to calculate a financial bonus. Behavioural performance on the perceptual judgement task was high (overall error rate = $1.77\% \pm 0.40\%$). Of the true mismatches, participants missed only $13.03\% \pm 5.09\%$, and false alarms only occurred on only $1.29\% \pm 0.21\%$ of the matched trials. Together, this resulted in participants making a response on $5.35\% \pm 0.20\%$ of all trials.

For the main analysis, any response was modelled separately with a regressor (see First-level analysis). Because the response was always the same thumb press and occurred with roughly equal probability for each finger combination, any incomplete modelling of the response-evoked activity should not influence our results pertaining to the differences in activity patterns between finger combination.

The next trial started after a variable inter-trial-interval (ITI), drawn randomly from the set of possible ITIs {1s, 2.5s, 4s, 5.5s, 7s, 8.5s, 10s} seconds, with the probability $p=[0.37, 0.24, 0.16, 0.10, 0.06, 0.04, 0.03]$ for each ITI, respectively. Thus, shorter delays occurred more often and longer delays occurred less often. The order of trials, including the position of the 3 probe trials, in each run was pseudo-random. Two trials for each of the 31 finger combinations were presented in each run, and participants completed 11 imaging runs each, yielding 682 trials total (31 combinations x 2 repeats x 11 runs).

The trial structure during the training and imaging sessions were the same. During training, participants performed runs of trials until they achieved an overall error rate of 0% in one run. Participants completed the training session 1-2 days before the first

scanning session. The 11 imaging runs were completed over two separate scanning sessions for each participant, usually within the same week.

4.5.4 fMRI acquisition and analysis

4.5.4.1 *Image acquisition*

We used high-field functional magnetic resonance imaging (fMRI, Siemens 7T Magnetom with a 32-channel head coil at Western University, London, Ontario, Canada) to measure the blood-oxygen-level dependent (BOLD) responses evoked in participants. Each participant completed 11 runs of trials across two separate scanning days, usually with 6 runs on the first day and 5 runs on the second day. Each run lasted 614s. During each run, 410 functional images were obtained using a multiband 2D-echoplanar imaging sequence (GRAPPA, in-plane acceleration factor=2, multi-band factor=3, repetition time [TR]=1500ms, echo time [TE]=20ms, in-plane resolution 148 x 148 voxels). Per image, we acquired 66 interleaved slices (without gap) with isotropic voxel size of 1.4mm. The first 2 images in the sequence were discarded to allow magnetization to reach equilibrium. To estimate magnetic field inhomogeneities, we acquired a gradient echo field map at the end of the scanning session on each day. Finally, a T1-weighted anatomical scan was obtained using a magnetization-prepared rapid gradient echo sequence (MPRAGE) with a voxel size of 0.75mm isotropic (3D gradient echo sequence, TR=6000ms, 208 volumes).

4.5.4.2 *Image preprocessing and first-level analysis*

Functional images were first realigned to correct for head motion during the scanning session (3 translations: x,y,z; 3 rotations: pitch, roll, yaw), and co-registered to each participant's anatomical T1-image. Within this process, we used B0 fieldmaps from each imaging session to correct for image distortions arising from magnetic field inhomogeneities (Hutton et al., 2002). Due to the relatively short TR (1.5s), no slice-timing correction was applied, and no spatial smoothing or normalization to a standard template was applied.

The minimally preprocessed data were then analysed using a general linear model (GLM; Friston, Jezzard, and Turner 1994) using SPM12 (fil.ion.ucl.ac.uk/spm/) using a separate regressor for each of the 31 possible finger combinations in each run. The activation during stimulation was modeled using a boxcar function that spanned the stimulation phase of each trial, convolved with a hemodynamic response function with a delayed onset of 1.5s and a post-stimulus undershoot at 12s. To capture activity evoked by the thumb presses during perceptual judgements, we included one thumb press regressor in each run which modeled the 3 thumb responses per run (duration: 1s). All trials were included in the analysis, regardless of the perceptual judgement accuracy. Finally, we included an intercept regressor for each run, yielding 363 total regressors (33 regressors x 11 runs).

To model the long-range temporal autocorrelations in the functional timeseries, we used the SPM FAST autocorrelation model. High-pass filtering was then achieved by temporally pre-whitening the functional data with this temporal autocorrelation estimate. This analysis yielded one beta-weight for each voxel for each of the 31 finger combinations per run for each participant. Collectively, these defined the estimated activity patterns. We did not further analyse the activity pattern from the thumb press regressor. From these beta-weights, we calculated the average percent signal change (PSC) evoked by each finger combination relative to the baseline for each voxel, yielding 31 PSC values per voxel.

4.5.4.3 *Surface-based analysis*

We used Freesurfer (Fischl, Sereno, and Dale 1999) to reconstruct the cortical white-matter/gray-matter surface and the pial surface from the anatomical image of each participant. The surfaces were then spherically registered to match a template atlas (FreeSurfer's Left-Right 164k node template) based on a sulcal-depth map and local curvature.

Individual activity patterns were then projected on the individual surface. All voxels touching the line between the corresponding vertices of the white matter and the pial surface were averaged. To avoid the mixing of signals between M1 and S1 across the

central sulcus, we excluded any voxel which touched the surface at two different places from all further analysis.

For multivariate analysis, we used a surface-based searchlight approach (Oosterhof et al., 2011). For each surface node on each participant's surface reconstruction, we defined a surrounding circular region of 160 voxels. The set of activity patterns from these voxels were then analysed together (see Multivariate fMRI analysis) and the results were assigned to the corresponding centre node.

To conduct more computationally intensive representational model comparison (see Representational model analysis) across the cortical surface, we employed a coarser alternative to the searchlight approach: We subdivided the left hemisphere into 1442 regular hexagonal tessels. We only analysed tessels that showed a reliable difference between the activity patterns associated with the different finger combinations (group-averaged dissimilarity between all patterns ≥ 0.005). This criterion yielded 82 tessels that spanned the surface of sensorimotor cortex.

4.5.4.4 *Regions of interest definition*

For a targeted analysis of subregions of the sensorimotor cortex, we used a probabilistic cytoarchitectonic atlas projected to the cortical surface (Fischl et al. 2008) to define Brodmann areas (BA) 4a, 4p, 3a, 3b, 1, and 2. Surface nodes were assigned to the region that had the highest probability, and this probability needed to exceed 0.25. We further restricted these regions to the hand area by excluding nodes that fell 2.5cm above and 2.5cm below the hand knob anatomical landmark (Yousry et al. 1997). To avoid smearing activity across the central sulcus, we again excluded voxels that touched the cortical surface at two separable places.

4.5.5 Estimating single-finger selectivity

4.5.5.1 *Voxel sub-selection*

To quantify the selectivity of each voxel to single fingers, we considered only the activity estimates for the single-finger conditions. We sub-selected voxels from each region that showed significant modulation (relative to baseline) during any single-finger stimulation,

by conducting an omnibus F -test per voxel, retaining only voxels that were significant on an $p=0.05$ level (uncorrected). This criterion selected $7.45\% \pm 0.74\%$ of the voxels from BA 4a, $6.84\% \pm 0.68\%$ from BA 4p, $7.49\% \pm 0.99\%$ from BA 3a, $15.52\% \pm 1.72\%$ from BA 3b, $12.74\% \pm 2.08\%$ from BA 1, and $7.12\% \pm 0.64\%$ from BA 2. We verified in simulations that this voxel sub-selection approach did not bias the subsequent selectivity analysis, but simply increased its power. This is because the omnibus F -test only tests *if* a voxel is tuned to one or more fingers, whereas the selectivity analysis characterizes the *shape* of the voxel's tuning to different fingers.

4.5.5.2 *Calculating finger selectivity*

We then normalized the tuning curves (5 activity values for each voxel), such that the maximal response equaled 1 and the lowest response equaled 0. For the plots in Figure 2B, we grouped the voxels according to the most preferred finger.

Using the normalized tuning curve for each voxel, we calculated the voxel's selectivity (λ) as

$$\lambda = 1 - \frac{1}{4} \sum_i y_i$$

, where y_i are the normalized responses to the “less-preferred” fingers. This yields the average difference between the activity evoked by the finger that the voxel is most *tuned* to (the maximal activity) and all other finger activities. Therefore, $\lambda = 1$ indicates a voxel is only active during stimulation of a specific finger. Conversely, $\lambda < 1$ indicates that a voxel also responds to stimulation of other fingers. For each participant, we averaged the resulting selectivities across the sub-selected voxels per region. This yielded one selectivity per region per participant.

4.5.5.3 *Controlling for measurement noise effects on finger selectivity*

Due to measurement noise, the estimated selectivities will always be < 1 . Furthermore, measurement noise may differ across regions, making it inappropriate to directly compare the selectivities. To address this issue, we simulated voxel tuning curves under two

different generative models. First, for random tuning, we simulated voxels with tuning that was drawn from a multivariate normal distribution, with covariance identical to the finger-by-finger correlation matrix (Ejaz, Hamada, and Diedrichsen 2015). Second, for perfect tuning, we simulated voxels that were selective for stimulation of a single finger and remained unresponsive to all other fingers. Both simulations were scaled, so that the average diagonal of the covariance matrix matched the signal strength for that region and participant (σ_s^2). We then added the measurement noise, drawn from a normal distribution with variance set to σ_ϵ^2 .

To estimate σ_s^2 and σ_ϵ^2 from the real data, we first vectorized the matrix of mean-centred tuning curves for each run, and then calculated the average covariance between these vectors across runs. An estimate of σ_ϵ^2 could then be obtained via $\sigma_\epsilon^2 = \frac{\sigma_s^2}{r} - \sigma_s^2$, where r is the average Pearson's correlation between the vectorized tuning curves across runs. This expression arises because we assume the noise in the real data is independent (i.e., uncorrelated) across different runs, and therefore, the expected value of the Pearson's correlation between vectorized tuning curves from different runs is $r = \sigma_s^2 / (\sigma_s^2 + \sigma_\epsilon^2)$.

Using these estimates, we simulated 1000 datasets with random tuning and 1000 datasets with perfectly selective tuning for each region in each participant, each with the same number of voxels as the real data. All data sets were simulated with 11 imaging runs. As for the real data, we then applied the voxel sub-selection to the simulated data. We calculated the average selectivity across voxels in each simulated dataset and averaged the selectivities across simulations. The selectivity of the real data was then normalized such that a selectivity of 0 reflected the expected value under random tuning and 1 reflected the expected value for perfectly selective tuning.

4.5.6 Multivariate fMRI analysis

To test for reliable differences between fMRI activity patterns for each condition (i.e., the first-level GLM beta-weights), we used the cross-validated squared Mahalanobis dissimilarity (i.e., crossnobis dissimilarity: Walther et al., 2016). Cross-validation ensures the dissimilarity estimates are unbiased, such that if two patterns differ only by measurement noise, the mean of the estimated dissimilarities would be zero. This also

means that estimates can sometimes become negative (Diedrichsen, Provost, and Zareamoghaddam 2016; Diedrichsen et al. 2020). Therefore, dissimilarities significantly larger than zero indicate that two patterns are reliably distinct, and we take this as evidence that features about the finger combinations are represented in the activity patterns.

The crossnobis dissimilarity d between the fMRI activity patterns (\mathbf{x}) for conditions i and j was calculated as

$$d_{i,j} = \frac{1}{M} \sum_m^M (\mathbf{x}_i - \mathbf{x}_j)_m^T \Sigma^{-1} (\mathbf{x}_i - \mathbf{x}_j)_{\sim m}$$

, where the activity patterns from run m are multiplied with the activity patterns averaged over all runs except m ($\sim m$). Σ is the voxel-wise noise covariance matrix, estimated from the residuals of the first-level GLM, and slightly regularized to ensure invertibility. Multivariate noise-normalization removes spatially correlated noise and yields generally more reliable dissimilarity estimates (Walther et al. 2016). Analyses were conducted using functions from the RSA (Nili et al. 2014) and PCM (Diedrichsen, Yokoi, & Arbuckle, 2018) MATLAB toolboxes. For the searchlight results (Fig. 4.1C, D), we averaged the resulting dissimilarities based on whether they were between single-finger patterns, 2-finger patterns, 3-finger patterns, and 4-finger patterns.

4.5.7 Representational model analysis

A representational model characterizes the tuning curves of a group of voxels or neurons. In the sense we are using it here, it specifies a probability distribution over all possible tuning curves (Diedrichsen and Kriegeskorte 2017). Here, we used an encoding-style approach (Naselaris et al. 2011) to specify and evaluate representational models that predicted activity patterns for all finger combinations using various feature sets. Models were fit and evaluated within each region and participant using cross-validation across imaging runs.

4.5.7.1 *Linear model*

The linear model predicted that activity patterns evoked during multi-finger stimulation were the sum of the constituent single-finger patterns:

$$\hat{Y}_{lin} = M_{lin}U_{sf}$$

, where \hat{Y}_{lin} are the [31 x P voxels] predicted activity patterns, U_{sf} is a [5 features x P voxels] matrix of single-finger feature patterns, and M_{lin} is a [31 combinations x 5 features] indicator matrix denoting which finger(s) are in each of the combinations. To complete the representational model, we also specified that the single-finger features had a second-moment matrix (co-variance matrix without subtraction of the mean across voxels) of G_{lin} . The second-moment matrix of finger-related patterns is highly invariant across individuals, reflecting the high correlations of patterns from neighboring fingers, and the low correlation of the pattern of the thumb with the other fingers (Ejaz, Hamada, and Diedrichsen 2015; Arbuckle et al. 2020). We determined the exact form of the matrix from the group-averaged second moment matrix \bar{G} for the area under question. From this, we determined the second moment matrix for the single-finger patterns that would best approximate the overall second moment matrix $G_{lin} = M_{lin}^+ \bar{G} M_{lin}^{+T}$, where M_{lin}^+ is the Moore-Penrose pseudoinverse.

4.5.7.2 *Multi-finger interaction models*

We also constructed 3 multi-finger interaction models. Like the linear model, these models assumed that the multi-finger patterns were the sum of the constituent single finger patterns, but also included specific interaction effects between specific fingers. These models took the same general form as the linear model above. For the 2-finger interaction model, we included 10 terms indicating the presence of a specific pair of fingers (i.e., when the pair of fingers was pressed, the regressor was 1 and 0 otherwise), in addition to the 5 model features for the individual fingers. In the 3-finger interaction model, we additionally added 10 regressors indicating the presence of each unique 3-finger combination. Finally, the 4-finger model included, in addition to the 3-, 2-, and 1-finger terms, the five possible 4-finger interactions, resulting in 30 model features

overall. For each of the models, the second-moment matrix for the feature patterns U was estimated from the group-averaged second-moment matrix as for the linear model.

4.5.7.3 *Adjacent and Non-adjacent 2-finger interaction models*

To test the strength of finger interactions between adjacent and non-adjacent finger pairs, we created two modified versions of the 2-finger interaction model. In the first version, we only included the 4 adjacent finger-pairs as interaction terms. In the second version we included only the 6 non-adjacent finger pairs.

4.5.7.4 *Linear-nonlinear model*

The linear-nonlinear model predicted that activity patterns for single-fingers combined linearly when multiple fingers were stimulated, but that the overall activity was compressed by a unknown, non-linear function f , $\hat{Y}_{lnl} = f(M_{lin}U_{sf})$. Such a non-linearity could arise from a global divisive normalization of neural activity in the region, or from non-linearities in the relationship between neural activity and the BOLD signal. To approximate any form of such compressive non-linearity, we created a model, based on the linear model, that allowed for flexible scaling of the predicted multi-finger patterns. All predicted patterns that included the same number of stimulated fingers were scaled by a common factor. These scaling factors as well as the single-finger feature patterns U_{sf} were estimated from the training data.

4.5.7.5 *Null model*

As a baseline for model comparison, we defined a null-model that predicted overall activity scaled the number of fingers stimulated, but that the patterns lacked finger-specificity. Under this model, the predicted patterns were derived from the average activity patterns for the single-finger, 2-finger, 3-finger, 4-finger, and 5-finger combinations, respectively. For example, the predicted single finger patterns was the average pattern across the five single-finger conditions.

4.5.7.6 *Noise-ceiling model*

To provide an estimate of how much systematic variation could be explained in the data given measurement noise, we included a “noise-ceiling” model. The predictions under the noise-ceiling model were simply the 31 activity patterns from the training data. Note that this fully saturated model differs from the 4-finger interaction model only by the addition of a single model term that models the specific non-linearities arising during the stimulation of all 5 fingers. The second-moment matrix for this model was set to the observed group-averaged estimate \bar{G} for the area under question.

4.5.7.7 *Model fitting*

We fit and evaluated the different models within each participant, using a leave-one-run-out cross-validation procedure. For each cross-validation fold, the training data were the activity patterns from all imaging runs except one, and the test data were the activity patterns from the left-out run.

For a representational model with the assumption that both noise and signal have multivariate Gaussian distribution (Diedrichsen and Kriegeskorte 2017), the feature patterns for each model can be estimated from the training data Y_{train} as:

$$U = (X^T X + G^{-1} s^{-1} \sigma_\epsilon^2)^{-1} X^T Y_{train}$$

, where X is a model-specific design matrix that denoted which feature(s) were present in each of the rows (activity patterns) in Y_{train} , G is the model-dependent second-moment matrix as specified above, s indicates the strength of the signal in Y_{train} , and σ_ϵ^2 is the variance of the random run-by-run noise. Note that this estimation takes the form of linear regression with Tikonov regularization. The strength of the regularization to the model prior was determined by $s^{-1} \sigma_\epsilon^2$. For each cross-validation fold, we derived the maximum-likelihood estimate of s and σ_ϵ^2 using the PCM toolbox. For the linear-nonlinear model, we additionally fitted the scaling parameters by minimizing the residual sums-of-squares of the model predicted patterns to the training data.

4.5.7.8 *Model evaluation*

The estimated feature patterns (U) were then used to predict activity patterns under the corresponding model. We compared the predicted 31 condition patterns with the left-out test data. The model fits were evaluated using Pearson's correlation. For this, the predicted and test patterns were first mean-centred (per voxel), then correlated across all voxels and conditions within each cross-validation fold. We averaged the correlations across cross-validation folds to yield a single estimate of model performance per participant per region. We preferred Pearson's correlation as our evaluation metric over the coefficient of determination, as it is less dependent on the exact choice of regularization coefficient (Diedrichsen and Kriegeskorte 2017), and therefore provides a more robust evaluation.

Finally, the model fits were normalized between 0 and 1 using the fits of the null and noise-ceiling models. Normalized fits >0 indicated that the model captured more information than the simple scaling of overall activity (null model), and fits <1 indicated that there was structured variance in the activity patterns that remained unaccounted for in the model(s).

4.5.8 *Statistical analyses*

All statistical tests were performed in MATLAB R2019a (Mathworks, Inc.). We set the significance level in our analyses to $p=0.05$. When a test involved multiple comparisons without any specified *a priori* hypotheses, we adjusted the significance level by dividing by the number of comparisons (i.e., Bonferroni correction). For clarity, we report uncorrected p -values in the text. The Bonferroni-corrected statistical threshold is reported as an α -value when appropriate. In cases where we had *a priori* hypotheses, we did not correct for multiple comparisons (i.e., replicating single-finger pattern overlap; Fig. 4.2C). To compare evoked activity, dissimilarities, or model fits across regions, we used within-participant repeated measures ANOVAs. We used two-sided paired t-tests to compare the model fits to the fit of the noise-ceiling in each region. If the model fit did not differ significantly from the fit of the noise-ceiling model, we considered the model to be as good as the noise-ceiling. Therefore, to remain conservative, we evaluated

uncorrected p -values and did not correct for multiple comparisons, as this correction would lower the bar for what would be considered a “good-fitting” model.

4.6 References

- Arbuckle, S. A., Weiler, J., Kirk, E. A., Rice, C. L., Schieber, M., Pruszynski, J. A., ... Diedrichsen, J. (2020). Structure of Population Activity in Primary Motor Cortex for Single Finger Flexion and Extension. *The Journal of Neuroscience: The Official Journal of the Society for Neuroscience*, 40(48), 9210–9223.
- Ariani, G., Andrew Pruszynski, J., & Diedrichsen, J. (2020). Motor planning brings human primary somatosensory cortex into movement-specific preparatory states. *bioRxiv*.
- Bensmaia, S. J., Denchev, P. V., Dammann, J. F., 3rd, Craig, J. C., & Hsiao, S. S. (2008). The representation of stimulus orientation in the early stages of somatosensory processing. *The Journal of Neuroscience: The Official Journal of the Society for Neuroscience*, 28(3), 776–786.
- Besle, J., Sánchez-Panchuelo, R.-M., Bowtell, R., Francis, S., & Schluppeck, D. (2014). Event-related fMRI at 7T reveals overlapping cortical representations for adjacent fingertips in S1 of individual subjects: Finger Representation Overlap in S1 at 7T. *Human Brain Mapping*, 35(5), 2027–2043.
- Biermann, K., Schmitz, F., Witte, O. W., Konczak, J., Freund, H.-J., & Schnitzler, A. (1998). Interaction of finger representation in the human first somatosensory cortex: a neuromagnetic study. *Neuroscience Letters*, Vol. 251, pp. 13–16.
- Brochier, T., Boudreau, M. J., Paré, M., & Smith, A. M. (1999). The effects of muscimol inactivation of small regions of motor and somatosensory cortex on independent finger movements and force control in the precision grip. *Experimental Brain Research. Experimentelle Hirnforschung. Experimentation Cerebrale*, 128(1–2), 31–40.
- Brodmann, K. (1909). *Vergleichende Lokalisationslehre der Grosshirnrinde in ihren Prinzipien dargestellt auf Grund des Zellenbaues*. Barth.
- Brouwer, G. J., Arnedo, V., Offen, S., Heeger, D. J., & Grant, A. C. (2015). Normalization in human somatosensory cortex. *Journal of Neurophysiology*, 114(5), 2588–2599.
- Carandini, M., & Heeger, D. J. (2011). Normalization as a canonical neural computation. *Nature Reviews. Neuroscience*, 13(1), 51–62.
- Carlson, M. (1981). Characteristics of sensory deficits following lesions of Brodmann's areas 1 and 2 in the postcentral gyrus of *Macaca mulatta*. *Brain Research*, 204(2), 424–430.
- Chemnitz, A., Dahlin, L. B., & Carlsson, I. K. (2013). Consequences and adaptation in daily life – patients' experiences three decades after a nerve injury sustained in adolescence. *BMC Musculoskeletal Disorders*, 14(1), 1–9.
- Crevecoeur, F., Barrea, A., Libouton, X., Thonnard, J.-L., & Lefèvre, P. (2017). Multisensory components of rapid motor responses to fingertip loading. *Journal of Neurophysiology*, 118(1), 331–343.

- Darian-Smith, C., & Darian-Smith, I. (1993). Thalamic projections to areas 3a, 3b, and 4 in the sensorimotor cortex of the mature and infant macaque monkey. *The Journal of Comparative Neurology*, 335(2), 173–199.
- Diedrichsen, J., Berlot, E., Mur, M., Schütt, H. H., & Kriegeskorte, N. (2020). Comparing representational geometries using the unbiased distance correlation. *arXiv*.
- Diedrichsen, J., & Kriegeskorte, N. (2017). Representational models: A common framework for understanding encoding, pattern-component, and representational-similarity analysis. *PLoS Computational Biology*, 13(4), e1005508.
- Diedrichsen, J., Provost, S., & Zareamoghaddam, H. (2016). On the distribution of cross-validated Mahalanobis distances. *arXiv*.
- Ejaz, N., Hamada, M., & Diedrichsen, J. (2015). Hand use predicts the structure of representations in sensorimotor cortex. *Nature Neuroscience*, 18(7), 1034–1040.
- Fischl, B., Sereno, M. I., & Dale, A. M. (1999). Cortical surface-based analysis. II: Inflation, flattening, and a surface-based coordinate system. *NeuroImage*, 9(2), 195–207.
- Fischl, Bruce, Rajendran, N., Busa, E., Augustinack, J., Hinds, O., Yeo, B. T. T., ... Zilles, K. (2008). Cortical folding patterns and predicting cytoarchitecture. *Cerebral Cortex*, 18(8), 1973–1980.
- Florence, S. L., Wall, J. T., & Kaas, J. H. (1988). The somatotopic pattern of afferent projections from the digits to the spinal cord and cuneate nucleus in macaque monkeys. *Brain Research*, 452(1–2), 388–392.
- Florence, S. L., Wall, J. T., & Kaas, J. H. (1989). Somatotopic organization of inputs from the hand to the spinal gray and cuneate nucleus of monkeys with observations on the cuneate nucleus of humans. *The Journal of Comparative Neurology*, 286(1), 48–70.
- Friedman, R. M., Chen, L. M., & Roe, A. W. (2008). Responses of areas 3b and 1 in anesthetized squirrel monkeys to single- and dual-site stimulation of the digits. *Journal of Neurophysiology*, 100(6), 3185–3196.
- Friston, K. J., Jezzard, P., & Turner, R. (1994). Analysis of functional MRI time-series. *Human Brain Mapping*, Vol. 1, pp. 153–171.
- Gale, D. J., Randall Flanagan, J., & Gallivan, J. P. (2021). Human somatosensory cortex is modulated during motor planning. *The Journal of Neuroscience: The Official Journal of the Society for Neuroscience*.
- Gandevia, S. C., Burke, D., & McKeon, B. B. (1983). Convergence in the somatosensory pathway between cutaneous afferents from the index and middle fingers in man. *Experimental Brain Research. Experimentelle Hirnforschung. Experimentation Cerebrale*, 50(2–3), 415–425.
- Geyer, S., A. Ledberg, A. Schleicher, S. Kinomura, T. Schormann, U. Bürgel, T. Klingberg, J. Larsson, K. Zilles, and P. E. Roland. (1996). Two Different Areas within the Primary Motor Cortex of Man. *Nature*, 382(6594), 805–7

- Ghosh, S., Brinkman, C., & Porter, R. (1987). A quantitative study of the distribution of neurons projecting to the precentral motor cortex in the monkey (*M. fascicularis*). *The Journal of Comparative Neurology*, 259(3), 424–444.
- Goldring, A. B., Cooke, D. F., Baldwin, M. K. L., Recanzone, G. H., Gordon, A. G., Pan, T., ... Krubitzer, L. (2014). Reversible deactivation of higher-order posterior parietal areas. II. Alterations in response properties of neurons in areas 1 and 2. *Journal of Neurophysiology*, 112(10), 2545–2560.
- Häger-Ross, C., Cole, K. J., & Johansson, R. S. (1996). Grip-force responses to unanticipated object loading: load direction reveals body- and gravity-referenced intrinsic task variables. *Experimental Brain Research. Experimentelle Hirnforschung. Experimentation Cerebrale*, 110(1), 142–150.
- Hernandez-Castillo, C. R., Maeda, R. S., Pruszynski, J. A., & Diedrichsen, J. (2020). Sensory information from a slipping object elicits a rapid and automatic shoulder response. *Journal of Neurophysiology*, 123(3), 1103–1112.
- Hikosaka, O., Tanaka, M., Sakamoto, M., & Iwamura, Y. (1985). Deficits in manipulative behaviors induced by local injections of muscimol in the first somatosensory cortex of the conscious monkey. *Brain Research*, 325(1–2), 375–380.
- Hochstetter, K., Rupp, A., Stančák, A., Meinck, H.-M., Stippich, C., Berg, P., & Scherg, M. (2001). Interaction of Tactile Input in the Human Primary and Secondary Somatosensory Cortex—A Magnetoencephalographic Study. *NeuroImage*, 14(3), 759–767.
- Hsiao, S. S., O’Shaughnessy, D. M., & Johnson, K. O. (1993). Effects of selective attention on spatial form processing in monkey primary and secondary somatosensory cortex. *Journal of Neurophysiology*, 70(1), 444–447.
- Hsieh, C.-L., Shima, F., Tobimatsu, S., Sun, S.-J., & Kato, M. (1995). The interaction of the somatosensory evoked potentials to simultaneous finger stimuli in the human central nervous system. A study using direct recordings. *Electroencephalography and Clinical Neurophysiology/Evoked Potentials Section*, Vol. 96, pp. 135–142.
- Hutton, C., Bork, A., Josephs, O., Deichmann, R., Ashburner, J., & Turner, R. (2002). Image distortion correction in fMRI: A quantitative evaluation. *NeuroImage*, 16(1), 217–240.
- Hyvärinen, J., & Poranen, A. (1978a). Movement-sensitive and direction and orientation-selective cutaneous receptive fields in the hand area of the post-central gyrus in monkeys. *The Journal of Physiology*, 283(1), 523–537.
- Hyvärinen, J., & Poranen, A. (1978b). Receptive field integration and submodality convergence in the hand area of the post-central gyrus of the alert monkey. *The Journal of Physiology*, Vol. 283, pp. 539–556.
- Ishibashi, H., Tobimatsu, S., Shigeto, H., Morioka, T., Yamamoto, T., & Fukui, M. (2000). Differential interaction of somatosensory inputs in the human primary sensory cortex: a magnetoencephalographic study. *Clinical Neurophysiology*:

Official Journal of the International Federation of Clinical Neurophysiology, 111(6), 1095–1102.

- Iwamura, Y. (1998). Hierarchical somatosensory processing. *Current Opinion in Neurobiology*, 8(4), 522–528.
- Iwamura, Y., Tanaka, M., Sakamoto, M., & Hikosaka, O. (1993). Rostrocaudal gradients in the neuronal receptive field complexity in the finger region of the alert monkey's postcentral gyrus. *Experimental Brain Research. Experimentelle Hirnforschung. Experimentation Cerebrale*, 92(3), 360–368.
- Jones, E. G. (1975). Lamination and differential distribution of thalamic afferents within the sensory-motor cortex of the squirrel monkey. *The Journal of Comparative Neurology*, 160(2), 167–203.
- Jones, E. G., & Powell, T. P. (1970). Connexions of the somatic sensory cortex of the rhesus monkey. 3. Thalamic connexions. *Brain: A Journal of Neurology*, 93(1), 37–56.
- Krause, T., Kurth, R., Ruben, J., Schwiemann, J., Villringer, K., Deuchert, M., ... Villringer, A. (2001). Representational overlap of adjacent fingers in multiple areas of human primary somatosensory cortex depends on electrical stimulus intensity: an fMRI study. *Brain Research*, 899(1–2), 36–46.
- Laboy-Juárez, K. J., Langberg, T., Ahn, S., & Feldman, D. E. (2019). Elementary motion sequence detectors in whisker somatosensory cortex. *Nature Neuroscience*, 22(9), 1438–1449.
- Lipton, M. L., Liszewski, M. C., Noelle O'Connell, M., Mills, A., Smiley, J. F., Branch, C. A., ... Schroeder, C. E. (2010). Interactions within the Hand Representation in Primary Somatosensory Cortex of Primates. *The Journal of Neuroscience: The Official Journal of the Society for Neuroscience*, 30(47), 15895–15903.
- Lyall, E. H., Mossing, D. P., Pluta, S. R., Dudai, A., & Adesnik, H. (2020). Synthesis of higher order feature codes through stimulus-specific supra-linear summation. *bioRxiv*.
- Martuzzi, R., van der Zwaag, W., Farthouat, J., Gruetter, R., & Blanke, O. (2014). Human finger somatotopy in areas 3b, 1, and 2: a 7T fMRI study using a natural stimulus: Human Finger Somatotopy in Areas 3b, 1, and 2. *Human Brain Mapping*, 35(1), 213–226.
- Moberg, E. (1958). Objective methods for determining the functional value of sensibility in the hand. *The Journal of Bone and Joint Surgery. British Volume*. doi:10.1302/0301-620X.40B3.454
- Monzée, J., Lamarre, Y., & Smith, A. M. (2003). The effects of digital anesthesia on force control using a precision grip. *Journal of Neurophysiology*, 89(2), 672–683.
- Naselaris, T., Kay, K. N., Nishimoto, S., & Gallant, J. L. (2011). Encoding and decoding in fMRI. *NeuroImage*, 56(2), 400–410.

- Nili, H., Wingfield, C., Walther, A., Su, L., Marslen-Wilson, W., & Kriegeskorte, N. (2014). A toolbox for representational similarity analysis. *PLoS Computational Biology*, 10(4), e1003553.
- Ohki, Y., Edin, B. B., & Johansson, R. S. (2002). Predictions specify reactive control of individual digits in manipulation. *The Journal of Neuroscience: The Official Journal of the Society for Neuroscience*, 22(2), 600–610.
- Oosterhof, N. N., Wiestler, T., Downing, P. E., & Diedrichsen, J. (2011). A comparison of volume-based and surface-based multi-voxel pattern analysis. *NeuroImage*, 56(2), 593–600.
- Phillips, J. R., Johnson, K. O., & Hsiao, S. S. (1988). Spatial pattern representation and transformation in monkey somatosensory cortex. *Proceedings of the National Academy of Sciences of the United States of America*, 85(4), 1317–1321.
- Powell, T. P., & Mountcastle, V. B. (1959). The cytoarchitecture of the postcentral gyrus of the monkey *Macaca mulatta*. *Bulletin of the Johns Hopkins Hospital*, 105, 108–131.
- Rathelot, J.-A., & Strick, P. L. (2009). Subdivisions of primary motor cortex based on cortico-motoneuronal cells. *Proceedings of the National Academy of Sciences of the United States of America*, 106(3), 918–923.
- Reed, J. L., Pouget, P., Qi, H.-X., Zhou, Z., Bernard, M. R., Burish, M. J., ... Kaas, J. H. (2008). Widespread spatial integration in primary somatosensory cortex. *Proceedings of the National Academy of Sciences of the United States of America*, 105(29), 10233–10237.
- Reed, J. L., Qi, H.-X., Zhou, Z., Bernard, M. R., Burish, M. J., Bonds, A. B., & Kaas, J. H. (2010). Response properties of neurons in primary somatosensory cortex of owl monkeys reflect widespread spatiotemporal integration. *Journal of Neurophysiology*, 103(4), 2139–2157.
- Ruben, J., Krause, T., Taskin, B., Blankenburg, F., Moosmann, M., & Villringer, A. (2006). Sub-area-specific Suppressive Interaction in the BOLD responses to simultaneous finger stimulation in human primary somatosensory cortex: evidence for increasing rostral-to-caudal convergence. *Cerebral Cortex*, 16(6), 819–826.
- Shanks, M. F., & Powell, T. P. (1981). An electron microscopic study of the termination of thalamocortical fibres in areas 3b, 1 and 2 of the somatic sensory cortex in the monkey. *Brain Research*, 218(1–2), 35–47.
- Sur, M. (1980). Receptive fields of neurons in areas 3b and 1 of somatosensory cortex in monkeys. *Brain Research*, 198(2), 465–471.
- Thakur, P. H., Fitzgerald, P. J., & Hsiao, S. S. (2012). Second-order receptive fields reveal multidigit interactions in area 3b of the macaque monkey. *Journal of Neurophysiology*, 108(1), 243–262.

- Walther, A., Nili, H., Ejaz, N., Alink, A., Kriegeskorte, N., & Diedrichsen, J. (2016). Reliability of dissimilarity measures for multi-voxel pattern analysis. *NeuroImage*, 137, 188–200.
- Yau, J. M., Connor, C. E., & Hsiao, S. S. (2013). Representation of tactile curvature in macaque somatosensory area 2. *Journal of Neurophysiology*, 109(12), 2999–3012.
- Yau, J. M., Kim, S. S., Thakur, P. H., & Bensmaia, S. J. (2016). Feeling form: the neural basis of haptic shape perception. *Journal of Neurophysiology*, 115(2), 631–642.
- Yousry, T. A., Schmid, U. D., Alkadhi, H., Schmidt, D., Peraud, A., Buettner, A., & Winkler, P. (1997). Localization of the motor hand area to a knob on the precentral gyrus. A new landmark. *Brain: A Journal of Neurology*, 120 (Pt 1), 141–157.

Chapter 5

5 General discussion

In this thesis, I performed a series of experiments that were designed to examine how M1 and S1 represent finger movements and integrate somatosensory inputs from multiple fingers. Previous studies have usually approached these questions either by measuring single neurons (e.g., for single finger movements Schieber and Hibbard, 1993; e.g., for sensory processing Thakur, Fitzgerald, and Hsiao, 2012), which is limited to a sparse sampling of the entire neural population, or by using fMRI to map where regions are activated (e.g., for movement: Huber et al. 2020; e.g., for sensory processing Bodegård et al. 2001), which does not reveal how conditions are represented within the active region(s). In my experiments, I took a different approach whereby I quantified *how* representations of finger movements and sensory inputs are organized in M1 and S1 using multivariate fMRI analyses.

In the first study (**Chapter 2**), I validated that representational geometries measured with fMRI are relatively stable across a broad range of overall activities (Arbuckle et al., 2019). This result is good news for all flavours of multivariate fMRI analyses (e.g., encoding, PCM, RSA) because it demonstrates that one of the key assumptions we make in such analyses is valid (at least for M1, S1, and V1/V2).

Having validated the multivariate analysis framework with fMRI data, I used this analysis to study how M1 represents single finger flexion and extension movements in M1 (**Chapter 3**). By comparing the fMRI results to neural spiking data recorded in monkeys trained to perform an identical task, I proposed a new organization of finger movements in M1, where neural populations that control opposing muscular patterns share common inputs and may spatially co-locate (Arbuckle et al. 2020).

In my third study (**Chapter 4**), I examined how somatosensory inputs from multiple fingers are represented in S1. Using representational models, I quantified to what degree the activity patterns in each subregion of S1 could be explained by a linear integration of single fingers, and to what degree higher-order interactions between multiple fingers also

occurred. My results showed that significantly strong multi-finger interactions occur throughout S1, and that each multi-finger combination is uniquely represented. This suggests that sensory inputs from all fingers are completely integrated within S1. More broadly, this suggests that S1 contains the neural substrate necessary for pattern recognition of any arbitrary stimulation across the fingers during dexterous object manipulation.

Each of the previous chapters has devoted space to discuss the findings of each study. Therefore, in the following sections, I build on these discussions and highlight five key questions that cut across the work I have presented in my thesis.

5.1 Can fMRI be used to make inferences about the neural population code?

Functional MRI is an incredibly popular tool to study brain activity in humans. The main advantages of fMRI are that it is non-invasive, has excellent spatial coverage, and is higher resolution compared to other non-invasive techniques. However, as with any measurement approach, fMRI comes with a set of caveats that will limit one's ability to draw conclusions about the underlying neural code. This is problematic since this is exactly the goal of multivariate fMRI. There are four main caveats. First, fMRI measures a proxy of neural activity that largely reflects excitatory postsynaptic activity. Second, fMRI is biased to representations that exist at broad spatial scales and is virtually blind to information that is encoded in a neuron-to-neuron variation. Third, interpretation of fMRI data depends on the assumption that the neural-to-fMRI coupling is linear and stable. Fourth, the fMRI signal has poor temporal resolution. Given all these constraints, to what degree can we draw valid inferences about the underlying neural code from fMRI data? In the following sections, I discuss each caveat in more detail, highlighting how they influence the conclusions we can make using fMRI and offer ways that they can be mitigated (if possible).

5.1.1 fMRI does not measure spiking

First, BOLD fMRI predominantly reflects synaptic activity rather than spiking outputs (Logothetis 2003). Although this may initially appear to be a limiting factor when making

inferences about the underlying neural organization, it can actually be a strength. Clearly, spiking output from neural populations produce downstream behaviour. But the spiking outputs produced depend on the inputs to, and local recurrent activity within, these neural populations. Unfortunately, single-cell recordings provide limited insight into these features (however, multi-electrode arrays and high-density recording probes can capture these features). This is further compounded by the fact that single-neuron recordings are biased towards large principal output cells, as they are often easier to locate and record from (Firmin et al. 2014; but this bias is weaker with arrays and high-density probes). Thus, measuring only spiking outputs will restrict the view that one has on the underlying neural population. A strong example of this is the work of Picard and colleagues (2013). They trained monkeys to produce sequences of reaching movements, some of which were visually guided whereas others were internally generated, meaning that the monkeys needed to learn the sequences. After 1-6 years of practice, the spiking outputs from neurons in M1 were comparable when producing either sequence type, even though the internally generated sequences were highly trained skills. However, measurements of metabolic activity in M1 (using [¹⁴C]2-deoxyglucose uptake) showed that less energy was required to produce the spiking activity during internally generated sequences, demonstrating that neural populations in M1 became more metabolically efficient after long-term training. Clearly, if the authors only measured spiking, they would have been blind to the learning-related changes in efficiency that had occurred for trained sequences.

The work of Picard and colleagues is a good example of how two different measurement modalities provide complementary views about the underlying neural processes. In the third chapter of my thesis, I combined the complementary viewpoints offered by BOLD fMRI and spiking to provide a testable hypothesis about how neural populations in M1 are organized to control dexterous hand movements. The hypothesized organization suggests that neural populations which control opposing muscular patterns in M1 receive shared sensory input and closely communicate, effectively forming a “functional unit”. With only the spiking data, I would have been unable to make this inference (the monkey dataset lacked local field potential data). Therefore, although BOLD fMRI does not

directly measure spiking, we can still use it to help make inferences about the organization of the underlying neural population.

5.1.2 fMRI is spatially biased

The second caveat is that fMRI is biased towards detecting representations that exist at a broad spatial scale (Kriegeskorte and Diedrichsen 2016). This bias arises because fMRI effectively averages the synaptic activity across all neural tissue within each voxel. This averaging removes any neuron-to-neuron variation that exists within each voxel, which can strongly distort representations measured with fMRI. But, like for the first caveat, an acknowledgement of this bias can also help to make inferences about the spatial organization of representations in the brain. For example, in Chapter 3, I found that the activity patterns evoked by presses of different fingers were more dissimilar than the activity patterns evoked by presses of the same finger in different directions. Thus, fingers appeared more strongly represented than directions in the population activity of M1. One possibility for this is that neurons that control movements of the same finger in opposing directions spatially co-localize in M1. Therefore, when measuring the population activities with fMRI, these local neuron-to-neuron variations in direction preference are averaged out. I leveraged this idea when interpreting the results from the fMRI and spiking datasets to make a testable prediction about the spatial structure of finger and direction representations in M1. As another example, in Chapter 4, the observation that individual voxels in BA 3 were selective to sensory inputs from a specific finger indicate that neurons in this region spatially cluster (to some degree) according to finger preference. Furthermore, that multi-finger interactions were evident at the spatial scale of fMRI suggests that these interactions were not limited to a few select neurons, but rather occurred across a sizable number of neurons within each voxel.

However, the spatial bias of fMRI can also be problematic. For example, when comparing the strength of representations across different regions, differences in the spatial organization of neurons in each region may obscure the measured representations and lead to erroneous inferences about representational content. Since the spatial bias is the result of the fMRI measurement process, it can be modelled, and its influence accounted for in more complex representational analyses (Kriegeskorte and Diedrichsen

2016). But, the effectiveness of this approach ultimately depends on how the measurement process is parameterized, and this can require prior knowledge of the spatial organization in the first place. So, what can be done when we lack a priori knowledge about the underlying spatial organization?

I suggest two possible approaches. First, one can attempt to estimate the spatial tuning to each class of representations. This is the approach I took in Chapter 3, where I evaluated the spatial tuning for fingers and directions in M1. For this, I calculated the correlations between voxel tuning profiles (see Fig. 1.3B and Fig. 3.6E) for fingers and for directions, separately, at various spatial distances. Features that are encoded at finer spatial distances would have correlations that decay (i.e., approach zero) faster. However, this approach itself is limited by the spatial resolution of the voxel, meaning that there is a limit to the spatial resolution that can be estimated with this analysis. Therefore, a second approach (to alleviate the spatial bias of fMRI) is to collect functional images with higher spatial resolution. However, there is a trade-off between voxel size and signal strength. Larger voxels have greater signal strength, and thus many studies commonly use larger voxel sizes (the influence of participant movement in the scanner is also attenuated with larger voxel sizes). Fortunately, the signal is stronger at higher magnetic field strengths (Gati et al. 1997; Yacoub et al. 2001), and so one can use this gain in signal strength to acquire higher resolution images. Linking back to Chapter 3, if direction representations exist at a smaller spatial scale than finger representations, then using higher resolution voxels will result in more distinct activity patterns for presses of the same finger in different directions.

However, using the BOLD contrast to image at higher resolutions than the $\sim 1.5\text{mm}^3$ resolution used in my thesis may not provide better insight into the spatial organization of representations in M1. Although the intrinsic resolution of the hemodynamic response of penetrating vessels is $\sim 1/2\text{mm}$ (in cats: O'Herron et al. 2016), one cannot achieve this resolution with gradient-echo BOLD. This because a substantial portion of the BOLD signal also arises from large draining veins on the cortical surface (Lai et al. 1993; Menon et al. 1993; Turner 2002). The pooling of blood into these macrovascular structures on the cortical surface “spreads” the BOLD signal. The spreading of BOLD signal that

occurs in response to a focal point of neural activity is called the point-spread function (PSF) of BOLD⁶. For 7T BOLD fMRI, the PSF is estimated to be ~1-2mm (in human V1, Shmuel et al. 2007; Chaimow et al., 2018)⁷. Thus, because the voxel size I used in Chapter 3 approximates the effective resolution of BOLD (due to the point spread effect), gradient-echo BOLD imaging at higher spatial resolution would not be a practical way to test my prediction that movement direction is represented at a smaller spatial scale than fingers in M1.

Therefore, to achieve higher resolution with fMRI, one needs to remove the macrovascular contributions (draining veins) from the measured signal. One approach is to mask-out the signal that arises from voxels that contain these large veins (Menon 2002). A second approach, which retains the data from all voxels, is to use a different fMRI contrast that measures cerebral blood volume (CBV) of the gray-matter microvasculature, which itself is also a proxy of changes in synaptic activity (O'Herron et al. 2016). The vascular space occupancy (VASO) contrast (Lu et al. 2003) is one contrast that measures cerebral blood volume, and recent efforts have made it more practical to use at high field strengths like 7T (Huber et al. 2014, 2015). The VASO signal acquisition implemented by Huber and colleagues includes a nulling of the CBV signal that arises from the macrovasculature on the cortical surface. Thus, this VASO signal more so reflects CBV changes in the microvasculature of the gray matter. In turn, this yields better spatial resolution than gradient-echo BOLD. Therefore, to study direction

⁶ In effect, there are 3 effective limits to the spatial resolution of BOLD fMRI: 1) resolution of neurovascular coupling (this is in respect to a single blood vessel); 2) the point spread function of BOLD (this is the combined effect across several blood vessels and includes the dilution effects of large draining veins); 3) the spatial resolution of the voxels (determined by the time available to read out gradient echos). Limits 2 and 3 are the biggest culprits in BOLD fMRI.

⁷ Although the BOLD PSFs for human M1 and S1 have not been evaluated, I can make an estimated guess as to whether they are larger or smaller than that in V1. Cortical vascular densities are thought to influence the BOLD PSF (Uludağ and Blinder 2018), and it is hypothesized that higher vascular densities result in smaller PSFs (Harrison et al. 2002). Furthermore, there is a moderately strong correlation between vascular and neural densities in rodents (Tsai et al. 2009) and primates (Weber et al. 2008), and so neural densities can provide a crude approximation of the PSF (e.g., smaller neural density \approx smaller vascular density \approx larger PSF). Given that M1 and S1 have lower neural densities than V1 in primates ($\sim 1/2$ in S1, $\sim 1/3$ in M1, see Collins et al., 2010), I predict that the BOLD PSF in M1 and S1 are larger than that in V1.

representations in M1 at a finer spatial scale, I would benefit from using a different contrast, such as VASO. However, given that any fMRI contrast is limited to the intrinsic resolution of the neurovascular response, there are spatial limits to the neural representations that can be resolved with fMRI – it is simply not possible to study neuron-to-neuron variation with fMRI.

5.1.3 Stability of representational analyses of fMRI data

The third caveat is that interpretations of fMRI data are predicated on the assumption that neural-to-BOLD fMRI coupling is linear and stable (Boynton et al. 1996). This assumption is critical in multivariate fMRI analyses. Violations of this assumption could come about from a variable spatial spreading of the BOLD signal at different levels of overall activity. This would mean that the fMRI activity patterns measured for certain conditions would distort as a function of the overall activity of the neural population (like the over-exposed photograph example from the introduction). Because this is such an important caveat, I dedicated an entire chapter to testing this assumption.

In Chapter 2, I quantified the stability of representational geometries measured across a broad range of overall activity in sensorimotor and visual cortices (Arbuckle et al. 2019). The good news was that, for the regions I studied (M1, S1, and V1/V2), the representational geometries appeared quite stable and therefore so too would inferences made using these representational geometries. This finding, however, should not be interpreted to mean that all representational geometries estimated from fMRI data are stable and independent of the underlying neural state. This is because neurovascular coupling might differ in different brain regions (Devonshire et al. 2012) and can be altered by neurological diseases (Girouard and Iadecola 2006). While these concerns cannot be entirely dismissed, these kinds of issues can be mitigated by careful estimation of the haemodynamic response in regions of interest and by conducting careful control analyses like those in Chapter 2⁸.

⁸ For example, in Chapter 3, I instructed participants to make individuated finger movements at different force levels, with the assumption that overall activity in M1 would change with pressing force. I then

5.1.4 Temporal resolution of fMRI

The fourth caveat is that BOLD fMRI has poor temporal resolution. This is because it is a blood-based signal. Thus, it is common practice to effectively average the signal over time. However, movement is a time-varying behaviour, and studying this behaviour with a temporally independent measure can be challenging. Using fMRI will not allow careful examination of any neural population dynamics that evolve over the course of the movement (Churchland et al. 2012; Shenoy, Sahani, and Churchland 2013). Fortunately, for the work presented in Chapter 3, I had the ability to characterize time-varying neural dynamics (in the monkey spiking data) that arise during individuated finger presses. In this dataset, I did not find substantial evidence to support the idea that neural activity in M1 evolved in a stereotyped fashion during individuated finger movements (i.e., variance of spiking patterns explained over time using two principal components ~15%, compared to ~30% for variance explained during reaching in Churchland et al. 2012). This agrees with recent work demonstrating that neural dynamics during grasping movements in monkey M1 are much less stereotyped than those recorded during reaching movements, suggesting that neural circuits underlying hand control are fundamentally different from that for arm control (Suresh et al. 2020).

Whether there are true stereotyped neural dynamics or not, fMRI cannot measure these temporal processes. However, this does not mean that fMRI cannot provide insight into the underlying neural substrates that facilitate behaviour. For example, using a novel multivariate analysis technique (PCM), we were recently able to dissect M1 activity patterns evoked during multi-finger sequences to address the question of whether neural populations in M1 form unique representations for trained movement sequences (Yokoi, Arbuckle, and Diedrichsen 2018; data not included in this thesis). We found that M1 did not generate sequence-specific representations (i.e., an encoding of the *order* of finger presses), but rather represented a linear combination of the consistent single-finger patterns. This suggests that activity in M1 is related to the execution of each individual

ensured my results were consistent across the different force levels (i.e. at different levels of overall activity), and only then reported the results averaged across the different forces.

movement element in a sequence. This finding is supported by recent electrophysiological recordings in monkeys trained on a sequential arm reaching task. The neural population dynamics estimated from M1 spiking data indicated that each component reach of the entire sequence was represented individually (Zimnik and Churchland 2021). Thus, even though BOLD has poor temporal resolution, advanced statistical analyses can allow one to overcome the temporal smearing of activity and make inferences about the functional organization of the underlying neural code. More broadly, the example above demonstrates how both representational and dynamical systems approaches to studying brain function can offer complementary insights.

5.2 Can single-finger movements tell us anything about how M1 is organized to control dexterous hand movements?

In this thesis, I have often commented on the great skill and precision humans show with hand movements. But in my experiments, participants were required to make presses with a single, isolated finger. There is clearly a visual distinction between the complexity of a single finger press and, for example, the finger coordination required to carefully stabilize and fold paper when making origami. However, although individuated finger movements may look simple, they are anything but. Neurons in M1 project to several motor neuron muscle pools in the spinal cord (McKiernan et al. 1998; Shinoda, Yokota, and Futami 1981), and thus, the muscle recruitment is broader than would be needed to move a single finger. Indeed, instead of recruiting only the muscles necessary to move a single finger, individuated finger movements require complex patterns of muscle activity in order to limit movements across other fingers (Schieber 1991; Yu, van Duinen, and Gandevia 2010). This fractionated control is attributed to neural populations in M1 (Muir and Lemon 1983; Takei et al. 2017) and their descending projections (Takei et al. 2017). The neural pathways that facilitate this individuated control are more developed in humans, and this is considered why humans are the most capable at producing individuated finger movements (Lemon 2008). Hence, instead of being relatively simple movements, I argue that individuated finger movements are complex. Such movements underlie the dexterous

abilities that make human hand control so special, and thus the activity patterns evoked during single-finger presses reflect the control processes I am interested in understanding.

However, it is important to clarify that although I have studied movements of single fingers, I do not suggest that M1 explicitly represent movements of single fingers. Indeed, the findings reported in this thesis and elsewhere (Nudo et al. 1992; Schieber and Hibbard 1993; Sanes et al. 1995; Ejaz, Hamada, and Diedrichsen 2015) support the notion that the underlying organization of hand movements in M1 is not that of single fingers. My results in Chapter 4 provide further empirical support for this idea. In the multi-finger stimulation experiment, I found that the multi-finger activity patterns in M1 could not be explained by a linear combination of single-finger patterns (see Fig. 4.3B). However, in this experiment participants did not make simultaneous finger movements, but instead received passive multi-finger stimulation. Therefore, to better test if the representations of multi-finger movements are comprised of single-fingers, I applied the representational model analyses from Chapter 4 to a different imaging dataset collected while participants produced all possible 31 finger chords ($n=8$; data from Ejaz et al., 2015; analyses not shown). I found that for representations of multi-finger movements in M1, combinations of the single-finger patterns provided significantly worse fits than simply the mean overall activity (normalized linear model fit = -1.03 ± 0.22 , $t_7=-4.78$, $p=0.002$; normalized nonlinear-linear model fit = -0.68 ± 0.21 , $t_7=-3.32$, $p=0.013$). Together, these results demonstrate that the underlying organization of M1 is not that of single fingers. Instead, my findings support the notion that M1 represents complex patterns of muscle activities that evoke movements of multiple finger that commonly occur in everyday activities (Nudo et al. 1992; Graziano 2006; Ejaz, Hamada, and Diedrichsen 2015). Under this organization, the fMRI activity patterns evoked during individuated finger presses reflect the unique combination of underlying neural patterns that are recruited to produce the movement of a single finger (Schieber 1990, 1995).

As an aside, this may seem at odds with the findings I discussed in the previous section, namely that activity patterns evoked in M1 during sequential finger presses appear to be linear combinations of the consistent single-finger patterns (Yokoi, Arbuckle, and Diedrichsen 2018). If M1 does not explicitly represent single fingers, why can linear

combinations of single-finger activity patterns predict the activity patterns evoked during sequential movements of different fingers? This is because each finger press in each sequence is temporally segregated, and so the cortical activity patterns necessary to produce muscle patterns evoking each press in the sequence are the same as those needed to evoke a single press in isolation. It follows that, if the sequences were comprised of multiple multi-finger chords, linear combinations of single-finger patterns would be unable to fully predict the sequence patterns. This is because a linear single-finger model does not account for the non-linearities that arise in M1 activity during simultaneous multi-finger movements.

5.3 The feature fallacy: Does the brain encode movements or muscles?

Neural populations in M1 are critical for producing dexterous hand movements that have ethological utility in our world. Therefore, the distributed activity patterns in M1 contain information that is used by downstream neurons to guide behaviour. In this section, I argue that even if we know that some features are represented in the distributed population activity, it may not provide significant insight into the computational functioning of a region. Indeed, if the research goal is to understand *how* the neural population in M1 controls dexterous hand movements, we should focus on *how* the neural population is functionally organized (i.e., the representational geometry of distributed patterns), not necessarily *what* features are represented. This is because different features can make similar (or even identical) predictions about brain representations, and so over-interpreting exactly *what* features are represented can be problematic.

Indeed, neurons in M1 show broad, heterogenous tuning to several movement features such as force (Evarts 1968), muscle EMG (Morrow and Miller 2003), movement/target direction (Georgopoulos, Schwartz, and Kettner 1986; Ashe and Georgopoulos 1994), and limb geometry (Scott and Kalaska 1997). These features are difficult to disambiguate because they often covary together – they are all related in some way to the movement that is produced. This is not to say that studies have not successfully separated these features, such as by altering arm postures and target locations in a reaching task (e.g., Scott and Kalaska 1997; Kakei, Hoffman, and Strick 1999), but across the literature, each

of these feature sets appear to be comparably good (and bad) descriptors of neural activity in M1. More problematic is that, because these features are tightly related, they often make similar predictions about representational organizations in M1.

For example, the seminal finding that hand movement direction is represented as a population code in M1 was interpreted as evidence that the spatial coordinate frames of movement were more strongly represented in M1 than muscle parameters (Georgopoulos, Schwartz, and Kettner 1986). The implication of this was that downstream neural populations were then responsible for transforming this higher-order direction code into the exact muscle commands needed to produce the corresponding movement. But it was quickly demonstrated that similar results also come about if, instead of movement direction, neurons in M1 are tuned to muscle parameters (Mussa-Ivaldi 1988). To further this argument, Lillicrap and Scott (2013) demonstrated that units in a neural network trained to control a simulated arm (which performed reaches and maintained posture under static loads) exhibited strong directional preferences (i.e., they represented directions). This occurred even though units in the network produced “muscle-like” commands, suggesting that directional tuning emerged incidentally. This serves as an excellent example of how two different features can make highly similar, if not identical, predictions about the structure of representations in the brain.

Therefore, the analyses in my thesis do not focus on *what* features are represented, but rather on the distribution of voxel tuning profiles. This distribution defines *how* representations are organized across population activity (independent of their spatial distribution⁹). The distribution of tuning profiles can be summarized by the collection of

⁹ The spatial arrangement of activity patterns is discarded in this analysis framework. This can be both a strength and a limitation. Without considering the spatial arrangement, I cannot make claims about whether features are encoded in localized regions, or broadly distributed across the entire population in an area without specialized analyses (such as the feature tuning analysis of chapter three, or the finger selectivity analysis from chapter four). Furthermore, the exact arrangement of these feature representations will likely influence the neural computations that occur for two reasons. First, spatially localized neurons may interact to a greater degree than more distant neurons, and this would therefore influence the degree to which certain features interact based on whether they are represented locally or more broadly. Second, neurons probably do not receive inputs from the entire population, but instead from specific subpopulations were not all features may be represented. One way to consider these spatial properties in representational analysis is to compare the representational geometries across smaller, more localized regions, such as the

dissimilarities (or covariances) between the activity patterns (see Fig. 1.2B). Importantly, two representational models are identical if they both predict the same representational geometry. This can occur even if the two models are built from different features (like the example discussed above). This is critical point because it means that inductive reasoning is not appropriate; that a representational model well-characterizes the data does not mean that the features used to construct the model are explicitly represented in the neural code. However, confusing the semantic labels of the tools/features that we use to describe brain activity data with the functional organization of the process that we are studying is rather common. This confusion between tools and processes is referred to as the *feature fallacy* (Diedrichsen 2019).

The idea behind the feature fallacy is not new. Fetz (1992) had a similarly powerful conviction about this same issue, stating that the approach of searching for features that are encoded in neurons is “like reading tea leaves, [because] this approach can be used to create an impression by projecting conceptual schemes onto suggestive patterns”. Indeed, it can be problematic to interpret the semantic labels of features too literally. However, I disagree with the implied idea that features are not useful neuroscientific tools. Defining features can be useful. They do ultimately provide semantically interpretable descriptors of the data. Some neurons may explicitly represent specific features (e.g., first-order sensory neurons). They are also practical because they help construct representational models. But one needs to be careful to separate the tools from the interpretations. The tools used in my thesis provide the ability to gain insight into how representations are organized (e.g., according to movement co-occurrence) but cannot elucidate the true underlying features (movements or muscles).

For example, in Chapter 3 I made model predicted geometries under the hypotheses that representations in M1 are organized according to the statistics of everyday hand movements, or according to the individual muscles that are recruited during the same movements. At face value, this would appear to be yet another test of whether M1

tessellated regions from chapter four. Another possible approach would be to spatially decompose the activity patterns and analyse the representational content within each spatial frequency.

encodes movements or muscles. However, although the movement co-occurrence model provided a better description of finger representations (irrespective of movement directions), this does not mean that M1 represents movements and not muscles (Phillips 1975; Kakei, Hoffman, and Strick 1999). Instead, it suggests that, if neural populations in M1 do represent muscles, it is in a manner that is highly structured by the patterns of muscle recruitment that occur during everyday hand use (Ejaz, Hamada, and Diedrichsen 2015; Tresch and Jarc 2009). I made no claim that finger movements (rather than muscle activities) have a special status or meaning to the representation. In fact, this argument detracts from the main insight from that study, which is that opposing movement directions elicit similar states of activity in M1. As another example, in Chapter 4, although I constructed representational models using adjacent or non-adjacent finger-pair interactions, the actual insight this analysis provided was about whether interactions occurred between spatially close or spatially distant areas of the hand. This analysis did not imply any special status about *neighbouring fingers per se*.

Ultimately, the importance assigned to specific features depends on the research question (Kriegeskorte and Diedrichsen, 2019), and my thesis work is not motivated by studying what is represented. More targeted analyses can be done to estimate the contribution of different features to the structure of brain representations (e.g., using pattern component modelling: Diedrichsen, Yokoi, and Arbuckle, 2018). Even in these approaches, however, features are only useful to the extent that they can make unique predictions about how representations are organized in the brain.

5.4 How is M1 organized to control dexterous hand movements?

I have thus far discussed that: 1) we can make inferences about the neural organization using representational fMRI analyses, 2) single-finger movements can be used to study functional organizations that support dexterous movements, and 3) my results cannot comment on whether the underlying neural code in M1 represents movements or muscles. Having established these points, I now discuss one of the motivating questions in my thesis, namely how is M1 organized to control dexterous movements? In the introduction, I presented evidence against a strict somatotopic or single-muscle

organization. Therefore, I focus my discussion here on the organization predicted by the results of Chapter 3.

Previous fMRI results (Ejaz, Hamada, and Diedrichsen 2015; Diedrichsen, Yokoi, and Arbuckle 2018), support the hypothesis that neural representations in M1 are organized according to the natural statistics of movement. Put another way, movements that commonly co-occur will be represented more similarly than movements that do not temporally co-occur. If this hypothesis can fully explain the functional organization in M1, then movements that cannot co-occur in daily life (i.e., like movements of the same limb in different directions) should be represented in non-overlapping (i.e., unique) neural substrates. Recent work has provided evidence for such an organization (Huber et al. 2020). However, the authors in this study used separate tasks (finger presses and whole-hand grasping/extension) to map fingers and directions. This is problematic as different neural populations in M1 are engaged during whole-hand grasping vs. precise finger movements (Muir and Lemon 1983). Therefore, I designed my task to explicitly tease apart individuated finger flexion and extension in a more careful manner.

In contrast to the prediction and the findings of Huber et al., I found that M1 activity patterns for presses of the same finger in opposing directions were highly similar, whereas movements of different fingers were quite distinct. This similarity could not be explained by muscle co-contraction during the experiment. Analysis of a complementary dataset of single neuron recordings from two monkeys trained on an identical task provided a unique opportunity to characterize the neural patterns in M1 at two spatial scales and with two different measurement modalities. This juxtaposition provided the means to propose a new hypothetical organization for the control of finger movements in M1.

I predict that neural populations that are involved in coordinating opposing muscular patterns form a functional unit that receives common sensory input and extensively communicate. This organization would have clear benefits for the control of dexterous hand movements. For example, during object manipulation with the hand, the force applied by a finger needs to be closely controlled. Thus, from an ethological perspective,

it makes sense to have a functional organization that facilitates tight coordination between neurons involved in producing the opposing movements of finger flexion and extension. Recent evidence from Griffin and Strick (2020) supports this idea that neurons in M1 tightly coordinate opposing muscular patterns. Using a small sample of output neurons in M1, they reported that two descending commands are present – one that facilitates agonist muscles to generate movement, and another to suppress the antagonist muscles and prevent movement opposition (via spinal interneurons). The spiking outputs of these neurons would thus be specific for each finger in each direction, but presumably the sensory inputs to these neurons would come from both the agonist and antagonist muscles. This common sensory input would lead to similar activity patterns measured with fMRI, but distinct spiking output patterns when recording from single neurons. Furthermore, neurons tuned to opposing muscular patterns (i.e., from the same functional unit) may also spatially intermix in order to support fast and efficient communication.

Two testable predictions emerge from this “functional unit” hypothesis. First, the synaptic inputs to, and recurrent activity within, populations involved in finger flexion and extension should be more similar than the spiking output. This prediction can be evaluated by contrasting the representations for single finger movements using LFP and spiking data measured in primates. Unfortunately, the monkey dataset that I analysed in Chapter 3 did not record LFP data, and so this prediction remains to be tested. The second, non-mutually exclusive prediction is that neural populations involved in finger flexion and extension are spatially arranged at a fine spatial scale. One way to test this spatial prediction is to image M1 at higher voxel resolution using VASO (see section 5.1.2). If direction representations do exist at a finer spatial scale, then the direction representations will be better resolved using higher resolution imaging. In contrast, finger representations, which exist at a spatial scale (~3-5mm, see Fig. 3.6E and Wiestler et al., 2011) that is larger than the voxel resolution in Chapter 3 (1.5mm^3), will be unaffected by higher resolution imaging. Therefore, under this spatial hypothesis, I predict that direction-specific dissimilarities (i.e., differences between the same finger pressing in different directions) would increase relative to the finger-specific dissimilarities (i.e., between different fingers pressing in the same direction) at higher voxel resolutions. Finally, an interesting avenue for future study is to consider whether these non-mutually

exclusive organizations (opposing muscular patterns eliciting similar states of activity in M1, and spatial scale of organization) are restricted to neural populations involved in hand control or are universal principles of organization in M1.

5.5 Why integrate somatosensory information across fingers?

In this final section, I consider why it is beneficial to integrate sensory information across fingers and discuss potential avenues for future work. What benefit does non-linear sensory integration provide? Consider the example where you are holding a cup in your hand and wish to prevent it from slipping. Any movement of the cup across your fingers will provide stimulation, but the behavioural response necessary to prevent slips will differ based on the pattern of stimulation. A downward movement of the object will cause slip in the same direction across fingers, but a rotation of the object in the hand will cause different slips to arise on the fingers. We would only be able to respond appropriately to each slipping pattern by non-linearly integrating the slip-direction signals across fingers. Therefore, non-linear sensory integration allows for a flexible mapping between arbitrary patterns of sensory inputs and motor responses.

Therefore, in order facilitate this flexible sensory-motor mapping, a neural population should uniquely represent each pattern of stimulation across fingers. Previous electrophysiological studies of finger integration have shown that, during simultaneous stimulation of fingers, the activity of neurons is sub-linear, and this has been taken as evidence that sensory integration across the fingers is non-linear. However, this non-linearity could reflect a general suppression of overall activity, akin to divisive normalization, not a non-linearity arising during integration of sensory information. Specifically, in this case, the underlying representations of sensory inputs from each finger are linearly summated, and the non-linearity arises only to suppress overall activity. This form of integration would not provide the neural substrate necessary for a fast detection of specific patterns of slipping across the fingers.

This is an important point, but it has been largely ignored in the finger integration literature. Perhaps this is because no other study has yet examined the representation of

all possible multi-finger stimulations. Without a broad stimulation battery, it is difficult to dissociate between a global non-linearity and local pattern interactions. This has also been the case for many studies examining multi-whisker integration in rodent barrel cortex, and only recently has it been demonstrated that distributed neurons in the barrel cortex are uniquely tuned to specific patterns of multi-whisker combinations. Laboy-Juarez and colleagues (2019) demonstrated that neurons in barrel cortex show highly selective tuning for two-whisker combinations. This tuning was not explainable by global non-linear scaling alone, as the combination selectivity occurred through a selective non-linear enhancement of the firing rate to the preferred combination. Following this, Lyall and colleagues (2020) examined a larger set of multi-whisker combinations. They stimulated all possible 31 combinations of five neighbouring whiskers. They too reported that specific sets of neurons in the barrel cortex were selectively tuned to each of the multi-whisker combinations, demonstrating a selective non-linear enhancement. Taken together, these studies suggest that S1 provides the neural substrate for unique representation of arbitrary patterns of sensory stimulation.

In Chapter 4, I extended this finding by showing evidence that human S1 also provides the neural substrate necessary for a complete and unique sensory representation of all possible multi-finger combinations. In that study, I applied passive tactile stimulation to all 31 possible single- and multi-finger combinations. Using representational model analyses, I demonstrated that much of the population activity across S1 (and M1) was explained by unique non-linear interactions between sensory inputs from specific sets of fingers, and not by a global non-linear suppression of activity. My results, in combination with those from the multi-whisker studies, support the idea that unique encoding of arbitrary patterns of somatosensory inputs is a general principle of somatosensory processing.

It is also worth acknowledging that the behavioural task in Chapter 4 did not require participants to integrate sensory information across fingers. Recall that the task in my study was a perceptual judgement task, where each participant needed to indicate whether a finger combination presented on a screen matched the stimulation felt on the fingers. In this task, each finger was identified separately, and so participants could have

successfully performed the task by simply noting which finger(s) were stimulated. This does not require multi-finger integration. Moreover, the stimulations themselves were not designed to feel “object-like”. That my analyses showed clear evidence of non-linear sensory integration further supports the notion that a general principle of somatosensory processing is that each multi-finger combination is uniquely represented in S1.

Furthermore, object manipulation (like folding origami) requires different hand postures. Neurons in primate S1 have receptive fields that span several joints of the hand, and this enables a unique representation of hand postures that arise during natural grasping actions (comparable to the unique representation of stimulation patterns in my experiment; Goodman et al. 2019). However, little is known about how the neural population in S1 integrate proprioceptive information of hand posture with tactile inputs from the hand. My experiment in Chapter 4 cannot speak to this because participants’ fingers were restrained (to limit movement during stimulation). But this is an important question because the hand is a flexible sensory organ, and so changes in hand posture (which occur during object manipulation) will influence how sensory signals from the fingers are integrated. Indeed, it would be necessary to take into account postural information when extracting information about the shape of an object (Yau et al. 2016). A study examining responses of single neurons in S1 (specifically BA 3b) showed that postural representations often exist in the same neurons that represent tactile inputs from the fingers (Kim et al. 2015). This intermixing of proprioceptive and cutaneous signals would therefore provide the neural substrate necessary to alter the integration of tactile inputs across fingers according to changes in hand posture. Indeed, in the same study, some neurons showed variable responses to the same pattern of tactile inputs when the relative location of each finger (i.e., hand posture) was altered. Whether these non-linearities lead to a highly unique representation of each pattern of tactile input for different hand postures remains to be studied. A highly unique non-linear integration of this sensory information would be ethologically beneficial. It would facilitate a flexible sensory-motor mapping that would enable fast, dexterous control of the hand – an ability that is important for object manipulation.

In future experiments, I plan to study these non-linear sensory interactions in S1 by varying the “object-like” patterns of stimulation. Specifically, we have developed an apparatus that can provide patterns of slipping stimulation to each of the five fingers independently (see Fig. 5.1). Using this device, I plan to apply patterns of slipping stimulations that mimic an object slipping or rotating the in hand and contrast the representations of these sensory signals in S1 to those evoked by patterns of random slipping across the fingers. Applying the same analyses as in Chapter 4, I predict that the object-like slipping conditions will elicit stronger, and distinct, non-linear interactions between sensory inputs compared to interactions arising during random slipping patterns that do not feel “object-like”. Stronger and distinct interactions would yield highly specific sensory representations that could trigger behavioural responses appropriate for the different slipping patterns produced by an object in the hand. A second avenue to pursue in future work is to study how changes in behavioural context (top-down) influence how sensory information from the hand is integrated. Indeed, the neural state of S1 is influenced by the planning of upcoming hand actions (Ariani, Andrew Pruszynski, and Diedrichsen 2020; Gale, Randall Flanagan, and Gallivan 2021), but it is unknown if this change in state primes the neural substrate in S1 for context-specific somatosensory integration.

5.6 Conclusion

Humans possess an unmatched ability for dexterous control of the hand. The results of this thesis have further elucidated how two cortical regions, M1 and S1, support this dexterity. First, neural populations in M1 are predicted to be organized in functional units that control opposing muscular patterns, allowing for fast coordinate of fine finger movements. Second, neural populations in S1 provide the neural substrate for rich, non-linear integration of somatosensory information across fingers. The work in this thesis additionally demonstrates how fMRI can be used to make inferences about how brain regions are functionally organized to compute information and enable behaviour in the world. More broadly, future work can build on the research efforts here to probe how M1 and S1 operate in synchrony to promote flexible hand control during object manipulation.

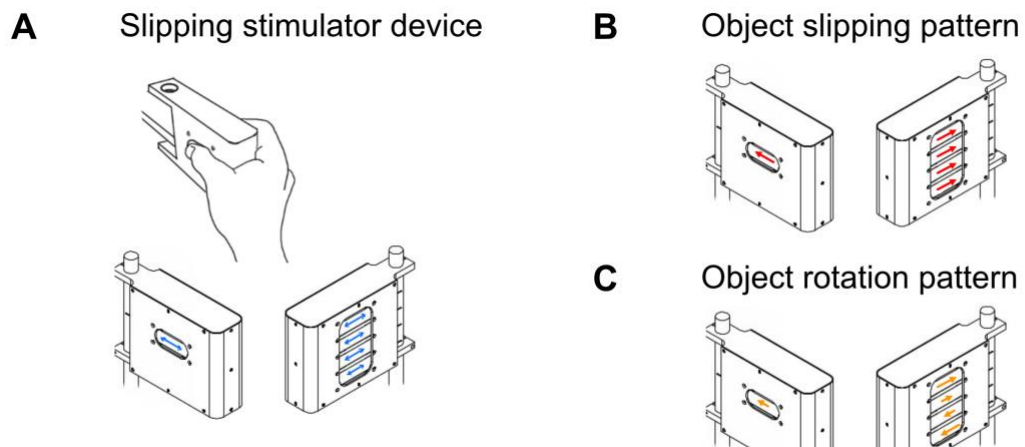


Figure 5.1: Slipping stimulator device

(A) Stimulator device that is designed to provide independent slipping stimulation to each of the five fingers of the right hand. Top panel shows a hand grasping the device. Bottom panels show the left and right views of the device, respectively. Each finger rests on a different “key”. The blue arrows indicate the possible movement directions of each key. By applying different patterns of key movements, it is possible to mimic sensations of object slip and rotation in the hand.

(B) Pattern of stimulation that mimics an object slipping out and away from the hand.

(C) Pattern of stimulation that mimics an object rotating in the hand. The length of each arrow reflects how far each key travels.

5.7 References

- Arbuckle, S. A., Weiler, J., Kirk, E. A., Rice, C. L., Schieber, M., Pruszynski, J. A., ... Diedrichsen, J. (2020). Structure of Population Activity in Primary Motor Cortex for Single Finger Flexion and Extension. *The Journal of Neuroscience: The Official Journal of the Society for Neuroscience*, 40(48), 9210–9223.
- Arbuckle, S. A., Yokoi, A., Pruszynski, J. A., & Diedrichsen, J. (2019). Stability of representational geometry across a wide range of fMRI activity levels. *NeuroImage*, 186, 155–163.
- Ariani, G., Andrew Pruszynski, J., & Diedrichsen, J. (2020). Motor planning brings human primary somatosensory cortex into movement-specific preparatory states. *bioRxiv*.
- Ashe, J., & Georgopoulos, A. P. (1994). Movement parameters and neural activity in motor cortex and area 5. *Cerebral Cortex*, 4(6), 590–600.
- Bodegård, A., Geyer, S., Grefkes, C., Zilles, K., & Roland, P. E. (2001). Hierarchical processing of tactile shape in the human brain. *Neuron*, 31(2), 317–328.
- Boynton, G. M., Engel, S. A., Glover, G. H., & Heeger, D. J. (1996). Linear Systems Analysis of Functional Magnetic Resonance Imaging in Human V1. *The Journal of Neuroscience: The Official Journal of the Society for Neuroscience*, 16(13), 4207–4221.
- Buzsáki, G., Anastassiou, C. A., & Koch, C. (2012). The origin of extracellular fields and currents--EEG, ECoG, LFP and spikes. *Nature Reviews. Neuroscience*, 13(6), 407–420.
- Chaimow, D., Yacoub, E., Uğurbil, K., & Shmuel, A. (2018). Spatial specificity of the functional MRI blood oxygenation response relative to neuronal activity. *NeuroImage*, 164, 32–47.
- Churchland, M. M., Cunningham, J. P., Kaufman, M. T., Foster, J. D., Nuyujukian, P., Ryu, S. I., & Shenoy, K. V. (2012). Neural population dynamics during reaching. *Nature*, 487(7405), 51–56.
- Collins, C. E., Airey, D. C., Young, N. A., Leitch, D. B., & Kaas, J. H. (2010). Neuron densities vary across and within cortical areas in primates. *Proceedings of the National Academy of Sciences of the United States of America*, 107(36), 15927–15932.
- Davis, Z. W., Muller, L., Martinez-Trujillo, J., Sejnowski, T., & Reynolds, J. H. (2020). Spontaneous travelling cortical waves gate perception in behaving primates. *Nature*, 587(7834), 432–436.
- Devonshire, I. M., Papadakis, N. G., Port, M., Berwick, J., Kennerley, A. J., Mayhew, J. E. W., & Overton, P. G. (2012). Neurovascular coupling is brain region-dependent. *NeuroImage*, 59(3), 1997–2006.

- Diedrichsen, J. (2019). Representational models and the feature fallacy. In M. S. Gazzaniga, G. R. Mangun, & D. Poeppel (Eds.), *The Cognitive Neurosciences* (sixth). MIT Press.
- Diedrichsen, J., Yokoi, A., & Arbuttle, S. A. (2018). Pattern component modeling: A flexible approach for understanding the representational structure of brain activity patterns. *NeuroImage*, Vol. 180, pp. 119–133.
- Ejaz, N., Hamada, M., & Diedrichsen, J. (2015). Hand use predicts the structure of representations in sensorimotor cortex. *Nature Neuroscience*, 18(7), 1034–1040.
- Evarts, E. V. (1968). Relation of pyramidal tract activity to force exerted during voluntary movement. *Journal of Neurophysiology*, 31(1), 14–27.
- Fetz, E. E. (1992). Are movement parameters recognizably coded in the activity of single neurons? *The Behavioral and Brain Sciences*, 15(4), 679–690.
- Firmin, L., Field, P., Maier, M. A., Kraskov, A., Kirkwood, P. A., Nakajima, K., ... Glickstein, M. (2014). Axon diameters and conduction velocities in the macaque pyramidal tract. *Journal of Neurophysiology*, 112(6), 1229–1240.
- Fromm, G. H., & Bond, H. W. (1964). Slow Changes In The Electrocoricogram And The Activity Of Cortical Neurons. *Electroencephalography and Clinical Neurophysiology*, 17, 520–523.
- Gale, D. J., Randall Flanagan, J., & Gallivan, J. P. (2021). Human somatosensory cortex is modulated during motor planning. *The Journal of Neuroscience: The Official Journal of the Society for Neuroscience*.
- Gati, J. S., Menon, R. S., Ugurbil, K., & Rutt, B. K. (1997). Experimental determination of the BOLD field strength dependence in vessels and tissue. *Magnetic Resonance in Medicine: Official Journal of the Society of Magnetic Resonance in Medicine / Society of Magnetic Resonance in Medicine*, 38(2), 296–302.
- Georgopoulos, A. P., Schwartz, A. B., & Kettner, R. E. (1986). Neuronal population coding of movement direction. *Science*, 233(4771), 1416–1419.
- Girouard, H., & Iadecola, C. (2006). Neurovascular coupling in the normal brain and in hypertension, stroke, and Alzheimer disease. *Journal of Applied Physiology*, 100(1), 328–335.
- Goodman, J. M., Tabot, G. A., Lee, A. S., Suresh, A. K., Rajan, A. T., Hatsopoulos, N. G., & Bensmaia, S. (2019). Postural Representations of the Hand in the Primate Sensorimotor Cortex. *Neuron*, 104(5), 1000-1009.e7.
- Graziano, M. (2006). The organization of behavioral repertoire in motor cortex. *Annual Review of Neuroscience*, 29, 105–134.
- Griffin, D. M., & Strick, P. L. (2020). The motor cortex uses active suppression to sculpt movement. *Science Advances*, 6(34).
- Harrison, R. V., Harel, N., Panesar, J., & Mount, R. J. (2002). Blood capillary distribution correlates with hemodynamic-based functional imaging in cerebral cortex. *Cerebral Cortex*, 12(3), 225–233.

- Huber, L., Finn, E. S., Handwerker, D. A., Bönstrup, M., Glen, D. R., Kashyap, S., ... Bandettini, P. A. (2020). Sub-millimeter fMRI reveals multiple topographical digit representations that form action maps in human motor cortex. *NeuroImage*, 208, 116463.
- Huber, L., Goense, J., Kennerley, A. J., Trampel, R., Guidi, M., Reimer, E., ... Möller, H. E. (2015). Cortical lamina-dependent blood volume changes in human brain at 7 T. *NeuroImage*, 107, 23–33.
- Huber, L., Ivanov, D., Krieger, S. N., Streicher, M. N., Mildner, T., Poser, B. A., ... Turner, R. (2014). Slab-selective, BOLD-corrected VASO at 7 Tesla provides measures of cerebral blood volume reactivity with high signal-to-noise ratio. *Magnetic Resonance in Medicine: Official Journal of the Society of Magnetic Resonance in Medicine / Society of Magnetic Resonance in Medicine*, 72(1), 137–148.
- Kakei, S., Hoffman, D. S., & Strick, P. L. (1999). Muscle and movement representations in the primary motor cortex. *Science*, 285(5436), 2136–2139.
- Kim, S. S., Gomez-Ramirez, M., Thakur, P. H., & Hsiao, S. S. (2015). Multimodal Interactions between Proprioceptive and Cutaneous Signals in Primary Somatosensory Cortex. *Neuron*, 86(2), 555–566.
- Kriegeskorte, N., & Diedrichsen, J. (2016). Inferring brain-computational mechanisms with models of activity measurements. *Philosophical Transactions of the Royal Society of London. Series B, Biological Sciences*, 371(1705). doi:10.1098/rstb.2016.0278
- Kriegeskorte, N., & Diedrichsen, J. (2019). Peeling the Onion of Brain Representations. *Annual Review of Neuroscience*, 42(1), 407–432.
- Laboy-Juárez, K. J., Langberg, T., Ahn, S., & Feldman, D. E. (2019). Elementary motion sequence detectors in whisker somatosensory cortex. *Nature Neuroscience*, 22(9), 1438–1449.
- Lai, S., Hopkins, A. L., Haacke, E. M., Li, D., Wasserman, B. A., Buckley, P., ... Friedland, R. (1993). Identification of vascular structures as a major source of signal contrast in high resolution 2D and 3D functional activation imaging of the motor cortex at 1.5T: preliminary results. *Magnetic Resonance in Medicine: Official Journal of the Society of Magnetic Resonance in Medicine / Society of Magnetic Resonance in Medicine*, 30(3), 387–392.
- Lemon, R. N. (2008). Descending pathways in motor control. *Annual Review of Neuroscience*, 31, 195–218.
- Logothetis, N. K. (2003). The Underpinnings of the BOLD Functional Magnetic Resonance Imaging Signal. *The Journal of Neuroscience: The Official Journal of the Society for Neuroscience*, 23(10), 3963–3971.
- Lu, H., Golay, X., Pekar, J. J., & Van Zijl, P. C. M. (2003). Functional magnetic resonance imaging based on changes in vascular space occupancy. *Magnetic Resonance in Medicine: Official Journal of the Society of Magnetic Resonance in Medicine / Society of Magnetic Resonance in Medicine*, 50(2), 263–274.

- Lyall, E. H., Mossing, D. P., Pluta, S. R., Dudai, A., & Adesnik, H. (2020). Synthesis of higher order feature codes through stimulus-specific supra-linear summation. *bioRxiv*.
- McKiernan, B. J., Marcario, J. K., Karrer, J. H., & Cheney, P. D. (1998). Corticomotoneuronal postspike effects in shoulder, elbow, wrist, digit, and intrinsic hand muscles during a reach and prehension task. *Journal of Neurophysiology*, 80(4), 1961–1980.
- Menon, R. S., Ogawa, S., Tank, D. W., & Uğurbil, K. (1993). Tesla gradient recalled echo characteristics of photic stimulation-induced signal changes in the human primary visual cortex. *Magnetic Resonance in Medicine: Official Journal of the Society of Magnetic Resonance in Medicine / Society of Magnetic Resonance in Medicine*, 30(3), 380–386.
- Menon, R. S. (2002). Postacquisition suppression of large-vessel BOLD signals in high-resolution fMRI. *Magnetic Resonance in Medicine: Official Journal of the Society of Magnetic Resonance in Medicine / Society of Magnetic Resonance in Medicine*, 47(1), 1–9.
- Morrow, M. M., & Miller, L. E. (2003). Prediction of muscle activity by populations of sequentially recorded primary motor cortex neurons. *Journal of Neurophysiology*, 89(4), 2279–2288.
- Muir, R. B., & Lemon, R. N. (1983). Corticospinal neurons with a special role in precision grip. *Brain Research*, 261(2), 312–316.
- Mussa-Ivaldi, F. A. (1988). Do neurons in the motor cortex encode movement direction? An alternative hypothesis. *Neuroscience Letters*, 91(1), 106–111.
- Nudo, R. J., Jenkins, W. M., Merzenich, M. M., Prejean, T., & Grenda, R. (1992). Neurophysiological correlates of hand preference in primary motor cortex of adult squirrel monkeys. *The Journal of Neuroscience: The Official Journal of the Society for Neuroscience*, 12(8), 2918–2947.
- O'Herron, P., Chhatbar, P. Y., Levy, M., Shen, Z., Schramm, A. E., Lu, Z., & Kara, P. (2016). Neural correlates of single-vessel haemodynamic responses in vivo. *Nature*, 534(7607), 378–382.
- Phillips, C. G. (1975). Laying the Ghost of 'Muscles Versus Movements.' *The Canadian Journal of Neurological Sciences. Le Journal Canadien Des Sciences Neurologiques*, 2(3), 209–218.
- Picard, N., Matsuzaka, Y., & Strick, P. L. (2013). Extended practice of a motor skill is associated with reduced metabolic activity in M1. *Nature Neuroscience*, 16(9), 1340–1347.
- Rathelot, J. A., & Strick, P. L. (2006). Muscle representation in the macaque motor cortex: an anatomical perspective. *Proceedings of the National Academy of Sciences of the United States of America*, 103(21), 8257–8262.

- Sanes, J. N., Donoghue, J. P., Thangaraj, V., Edelman, R. R., & Warach, S. (1995). Shared neural substrates controlling hand movements in human motor cortex. *Science*, 268(5218), 1775–1777.
- Schieber, M. H. (1990). How might the motor cortex individuate movements? *Trends in Neurosciences*, 13(11), 440–445.
- Schieber, M. H. (1991). Individuated finger movements of rhesus monkeys: a means of quantifying the independence of the digits. *Journal of Neurophysiology*, 65(6), 1381–1391.
- Schieber, M. H. (1995). Muscular production of individuated finger movements: the roles of extrinsic finger muscles. *The Journal of Neuroscience: The Official Journal of the Society for Neuroscience*, 15(1 Pt 1), 284–297.
- Schieber, M. H., & Hibbard, L. S. (1993). How somatotopic is the motor cortex hand area? *Science*, 261(5120), 489–492.
- Scott, S. H., & Kalaska, J. F. (1997). Reaching movements with similar hand paths but different arm orientations. I. Activity of individual cells in motor cortex. *Journal of Neurophysiology*, 77(2), 826–852.
- Shenoy, K. V., Sahani, M., & Churchland, M. M. (2013). Cortical Control of Arm Movements: A Dynamical Systems Perspective. *Annual Reviews Neuroscience*.
- Shinoda, Y., Yokota, J., & Futami, T. (1981). Divergent projection of individual corticospinal axons to motoneurons of multiple muscles in the monkey. *Neuroscience Letters*, 23(1), 7–12.
- Shmuel, A., Yacoub, E., Chaimow, D., Logothetis, N. K., & Ugurbil, K. (2007). Spatio-temporal point-spread function of fMRI signal in human gray matter at 7 Tesla. *NeuroImage*, 35(2), 539–552.
- Suresh, A. K., Goodman, J. M., Okorokova, E. V., Kaufman, M., Hatsopoulos, N. G., & Bensaïa, S. J. (2020). Neural population dynamics in motor cortex are different for reach and grasp. *ELife*, 9, e58848.
- Takei, T., Confais, J., Tomatsu, S., Oya, T., & Seki, K. (2017). Neural basis for hand muscle synergies in the primate spinal cord. *Proceedings of the National Academy of Sciences of the United States of America*, 114(32), 8643–8648.
- Thakur, P. H., Fitzgerald, P. J., & Hsiao, S. S. (2012). Second-order receptive fields reveal multidigit interactions in area 3b of the macaque monkey. *Journal of Neurophysiology*, 108(1), 243–262.
- Tresch, M. C., & Jarc, A. (2009). The case for and against muscle synergies. *Current Opinion in Neurobiology*, 19(6), 601–607.
- Tsai, P. S., Kaufhold, J. P., Blinder, P., Friedman, B., Drew, P. J., Karten, H. J., ... Kleinfeld, D. (2009). Correlations of Neuronal and Microvascular Densities in Murine Cortex Revealed by Direct Counting and Colocalization of Nuclei and Vessels. *The Journal of Neuroscience: The Official Journal of the Society for Neuroscience*, 29(46), 14553–14570.

- Turner, R. (2002). How Much Cortex Can a Vein Drain? Downstream Dilution of Activation-Related Cerebral Blood Oxygenation Changes. *NeuroImage*, 16(4), 1062–1067.
- Uludağ, K., & Blinder, P. (2018). Linking brain vascular physiology to hemodynamic response in ultra-high field MRI. *NeuroImage*, 168, 279–295.
- Weber, B., Keller, A. L., Reichold, J., & Logothetis, N. K. (2008). The microvascular system of the striate and extrastriate visual cortex of the macaque. *Cerebral Cortex*, 18(10), 2318–2330.
- Wiestler, T., McGonigle, D. J., & Diedrichsen, J. (2011). Integration of sensory and motor representations of single fingers in the human cerebellum. *Journal of Neurophysiology*, 105(6), 3042–3053.
- Yacoub, E., Shmuel, A., Pfeuffer, J., Van De Moortele, P. F., Adriany, G., Andersen, P., ... Hu, X. (2001). Imaging brain function in humans at 7 Tesla. *Magnetic Resonance in Medicine: Official Journal of the Society of Magnetic Resonance in Medicine / Society of Magnetic Resonance in Medicine*, 45(4), 588–594.
- Yau, J. M., Kim, S. S., Thakur, P. H., & Bensmaia, S. J. (2016). Feeling form: the neural basis of haptic shape perception. *Journal of Neurophysiology*, 115(2), 631–642.
- Yokoi, A., Arbuckle, S. A., & Diedrichsen, J. (2018). The Role of Human Primary Motor Cortex in the Production of Skilled Finger Sequences. *The Journal of Neuroscience: The Official Journal of the Society for Neuroscience*, 38(6), 1430–1442.
- Yu, W. S., van Duinen, H., & Gandevia, S. C. (2010). Limits to the control of the human thumb and fingers in flexion and extension. *Journal of Neurophysiology*, 103(1), 278–289.
- Zimnik, A. J., & Churchland, M. M. (2021). Independent generation of sequence elements by motor cortex. *Nature Neuroscience*, 24(3), 412–424.

Appendices



**Western
Research**

Research Ethics

**Western University Health Science Research Ethics Board
HSREB Delegated Initial Approval Notice**

Principal Investigator: Prof. Joern Diedrichsen
Department & Institution: Science/Computer Science, Western University

Review Type: Delegated
HSREB File Number: 107061
Study Title: Neural correlates of skillfull finger movements

HSREB Initial Approval Date: September 28, 2015
HSREB Expiry Date: September 28, 2016

Documents Approved and/or Received for Information:

Document Name	Comments	Version Date
Recruitment Items	Revised advertisement text	2015/09/11
Western University Protocol	Received 24Sep15	
Letter of Information & Consent		2015/09/11

The Western University Health Science Research Ethics Board (HSREB) has reviewed and approved the above named study, as of the HSREB Initial Approval Date noted above.

HSREB approval for this study remains valid until the HSREB Expiry Date noted above, conditional to timely submission and acceptance of HSREB Continuing Ethics Review.

The Western University HSREB operates in compliance with the Tri-Council Policy Statement Ethical Conduct for Research Involving Humans (TCPS2), the International Conference on Harmonization of Technical Requirements for Registration of Pharmaceuticals for Human Use Guideline for Good Clinical Practice Practices (ICH E6 R1), the Ontario Personal Health Information Protection Act (PHIPA, 2004), Part 4 of the Natural Health Product Regulations, Health Canada Medical Device Regulations and Part C, Division 5, of the Food and Drug Regulations of Health Canada.

Members of the HSREB who are named as Investigators in research studies do not participate in discussions related to, nor vote on such studies when they are presented to the REB.

The HSREB is registered with the U.S. Department of Health & Human Services under the IRB registration number IRB 0000940.

[Redacted Signature]
Ethics Officer, on behalf of Dr. Joseph Gilbert, HSREB Chair

Ethics Officer to Contact for Further Information

Erika Basile ebasile@uwo.ca	Grace Kelly grace.kelly@uwo.ca	Mira Mekhail mmekhail@uwo.ca	Vikki Tran vikki.tran@uwo.ca
--------------------------------	-----------------------------------	---------------------------------	---------------------------------

This is an official document. Please retain the original in your files.

Western University, Research, Support Services Bldg., Rm. 5150
London, ON, Canada N6G 1G9 t. 519.661.3036 f. 519.850.2466 www.uwo.ca/research/ethics

Appendix A: fMRI behavioural ethics approval



Research Ethics

Western University Non-Medical Research Ethics Board
NMREB Delegated Initial Approval Notice

Principal Investigator: Prof. Joern Diedrichsen
Department & Institution: Science/Computer Science, Western University

NMREB File Number: 108479
Study Title: Studies of the acquisition and control of skilled finger movements.

NMREB Initial Approval Date: May 15, 2017
NMREB Expiry Date: May 15, 2018

Documents Approved and/or Received for Information:

Document Name	Comments	Version Date
Revised Western University Protocol		2017/04/03
Revised Letter of Information & Consent		2017/04/03
Advertisement		2017/05/12

The Western University Non-Medical Research Ethics Board (NMREB) has reviewed and approved the above named study, as of the NMREB Initial Approval Date noted above.

NMREB approval for this study remains valid until the NMREB Expiry Date noted above, conditional to timely submission and acceptance of NMREB Continuing Ethics Review.

The Western University NMREB operates in compliance with the Tri-Council Policy Statement Ethical Conduct for Research Involving Humans (TCPS2), the Ontario Personal Health Information Protection Act (PHIPA, 2004), and the applicable laws and regulations of Ontario.

Members of the NMREB who are named as Investigators in research studies do not participate in discussions related to, nor vote on such studies when they are presented to the REB.

The NMREB is registered with the U.S. Department of Health & Human Services under the IRB registration number IRB 00000941.


 Ethics Officer, on behalf of Dr. Riley Hinson, NMREB Chair or delegated board member

EO: Erika Basile ___ Grace Kelly ___ Kathryn Harris ___ Nicole Morphet ___ Karen Gospatl

Appendix B: Behavioural ethics approval (for EMG experiment)



ELSEVIER

About Elsevier Products & Solutions Services Shop & Discover

Permission guidelines ScienceDirect content ClinicalKey content Tutorial videos Help and support

Can I include/use my article in my thesis/dissertation? –

Yes. Authors can include their articles in full or in part in a thesis or dissertation for non-commercial purposes.

Appendix C: Article reuse permissions for NeuroImage (Chapter 2)

Author Rights

Authors do not need to obtain permission to reuse their material, including to:

- Reuse figures and tables in future works
- Include articles in theses or dissertations
- Reprint articles in books or compilations of their work
- Deposit the accepted manuscript version of their manuscript in an institutional repository or on their personal website. The *JNeurosci*-formatted PDF may be used 6 months after issue publication, or immediately if published Open Choice.

The original article in *JNeurosci* must be cited and linked to, where appropriate.

Appendix D: Article reuse permissions for Journal of Neuroscience (Chapter 3)

Curriculum Vitae – Spencer A. Arbuckle

Education

2016–2021	Ph.D. Neuroscience	Western University	advisors: Jörn Diedrichsen & Andrew Pruszynski
2010–14	B.Sc. (Hon.) Psychology	Queen’s University	advisor: Ingrid Johnsrude

Publications

- [7] **Arbuckle SA**, Pruszynski JA, Diedrichsen J. (2021) Mapping the integration of sensory information across fingers in human sensorimotor cortex. *bioRxiv (preprint)*
- [6] Fox AS, Holley D, Klink PC, **Arbuckle SA**, Barnes CA, Diedrichsen J, Kwok SC, Kyle C, Pruszynski JA, Seidlitz J, Zhou X, Poldrack RA, Gorgolewski KJ. (2021) Sharing voxelwise neuroimaging results from rhesus monkeys and other species with Neurovault. *NeuroImage* 225: 117518.
- [5] **Arbuckle SA**, Weiler J, Kirk EA, Rice CL, Schieber MH, Pruszynski JA, Ejaz N, Diedrichsen J. (2020) Structure of population activity in primary motor cortex for single finger flexion and extension. *Journal of Neuroscience* 40: 9210-9223.
- [4] **Arbuckle SA**, Yokoi A, Pruszynski JA, Diedrichsen J. (2019) Stability of representational geometry across a wide range of fMRI activity levels. *NeuroImage* 186: 155-163.
- [3] Yokoi A, **Arbuckle SA**, Diedrichsen J. (2018) The role of human primary motor cortex in the production of skilled finger sequences. *Journal of Neuroscience* 38: 1430-1442.
- [2] Diedrichsen J, Yokoi A, **Arbuckle SA**. (2018) Pattern Component Modeling: A flexible approach for understanding the representational structure of brain activity patterns. *NeuroImage* 180: 119-133.
- [1] Lambert C, **Arbuckle SA**, Holden R. (2016) The Marlow-Crowne Social Desirability Scale outperforms the BIDR Impression Management Scale for identifying fakers. *Journal of Research in Personality* 61: 80-86.

Awards & Scholarships

2020	Western University Neuroscience Research Day poster award
2019	DPZ Primate Systems Neuroscience Summer School Travel Award
2018–21	NSERC PGS-D Postgraduate Scholarship
2018	Ontario Graduate Scholarship – <i>declined</i>
2017	Nominated to attend Canadian Student Health Research Forum conference
2017	Western University Neuroscience Conference Travel Award
2017	Computational Sensorimotor Neuroscience (<i>CoSMo</i>) Summer School – Best project
2017	Brain Canada Travel Scholarship to attend <i>CoSMo</i> Summer School
2017	BMI Collaborative Research Grant: Ejaz, Weiler, & Arbuckle
2013,14	Queen’s University Dean’s Honour List

- 2010 Queen's University Academic Excellence Entrance Scholarship
 2010 University of Winnipeg Special Entrance Scholarship – *declined*

Invited Talks

- 11/2020 Cortical contributions to human hand control. Be.Neuro Lab, Dept. of Bioengineering, Imperial College London, London, UK.
 03/2018 Can fMRI be used to make inferences on neural representations? Dept. of Cognitive, Linguistic, & Psychological Sciences, Brown University, Providence, USA.
 04/2017 An introduction to pattern component modeling. BLAM Lab, Dept. of Neurology, Johns Hopkins University School of Medicine, Baltimore, USA.

Workshop Participation

- 2019 Representational Similarity Analysis 3.0 Workshop. Collingwood, Canada.
 2019 DPZ Primate Systems Neuroscience Summer School. Bad Bevensen, Germany.
travel grant awarded
 2017 Computational Sensorimotor Neuroscience (*CoSMo*). University of Minnesota, USA.
travel grant awarded

Conference Talks

- [5] **Arbuckle SA***, Pruszynski JA, Diedrichsen J. (2020) Integration of tactile information from multiple fingers in human primary somatosensory cortex measured using high-resolution fMRI. Robarts Research Retreat, London, Canada.
 [4] **Arbuckle SA**, Weiler J, Kirk EA, Saikaley M, Rice C, Schieber M, Diedrichsen J, Ejaz N*. (2018) Representation of fingers and finger movement direction in the primary motor cortex. Society for the Neural Control of Movement, Santa Fe, USA.
 [3] Liu M*, **Arbuckle SA**, Okorokova L, Herrera* A, Kaiser A. (2017) Does S1 spiking activity encode sensory feedback for goal-directed movements in a grasping task? Advances in Motor Learning & Motor Control, Washington D.C., USA.
 [2] **Arbuckle SA***, Weiler J, Kirk EA, Saikaley M, Rice C, Schieber M, Diedrichsen J, Ejaz N. (2017) Extension and flexion representations in M1 spatially cluster around the moving finger. Advances in Motor Learning & Motor Control, Washington D.C., USA.
 [1] Ritz H, **Arbuckle SA**, Wild C, Johnsrude I.* (2015) Enhanced recognition memory for acoustically degraded sentences. 39th MidWinter Meeting of the Association for Research in Otolaryngology, Baltimore, USA.

**indicates primary speaker*

Conference Posters

- [7] **Arbuckle SA***, Pruszynski JA, Diedrichsen J. (2020) Integration of tactile information from multiple fingers in human primary somatosensory cortex measured using high-resolution fMRI. Neuroscience Research Day, London, Canada. *top poster award*

- [6] **Arbuckle SA***, Pruszynski JA, Diedrichsen J. (2019) Integration of tactile information from multiple fingers in human primary somatosensory cortex measured using high-resolution fMRI. Society for Neuroscience, Chicago, USA.
- [5] **Arbuckle SA***, Weiler J, Kirk EA, Saikaley M., Rice C, Schieber M, Diedrichsen J, Ejaz N. (2018) Representation of fingers and finger movement direction in the primary motor cortex. Canadian Student Health Research Forum, Winnipeg, Canada. *nominated to attend by the Western Neuroscience graduate program*
- [4] **Arbuckle SA***, Weiler J, Kirk EA, Saikaley M., Rice C, Schieber M, Diedrichsen J, Ejaz N. (2018) Representation of fingers and finger movement direction in the primary motor cortex. Mechanisms of Dexterous Behaviour, HHMI Janelia, USA.
- [3] **Arbuckle SA***, Yokoi A, Diedrichsen J. (2017) Is representational similarity analysis stable across a broad range of overall fMRI activity levels? Organization for Human Brain Mapping, Vancouver, Canada. *travel grant awarded*
- [2] **Arbuckle SA***, Yokoi A, Diedrichsen J. (2016) Stability of representational similarity analysis across a large range of overall activation levels. Society for Neuroscience, San Diego, USA.
- [1] Diedrichsen J*, **Arbuckle SA**, Yokoi, A. (2016) Studying the representational structure of simple and complex hand movements in the human motor cortex. Neural Control of Movement, Montego Bay, Jamaica.

Selected Teaching Experience (lecturing, workshops, TAships)

2020–21	Intro to Data Science I (compsci 4414)	Western University
2020	Intro to Neural Networks (psyc 9221B / app math 9624B)	Western University
2018–	Regular speaker, Computational Core Methods Lunches	Western University
2017	Information Systems (compsci 1032)	Western University
2016	Statistics for Science (stats 2244)	Western University
2016	Intro to Statistics (stats 1024)	Western University
2012–14	Principles of Psychology (psyc 100)	Queen's University

Other

Community outreach: local school science fair judge (2017, 2019, 2020), member of UWO Society of Neuroscience Graduate Students presentation workshop committee

Invited Reviewer: Journal of Neurophysiology, NeuroImage

Personal webpage: spencerarbuckle.com